Dielectric laser acceleration of non-relativistic electrons at a photonic structure

John Breuer

München 2013

Dielectric laser acceleration of non-relativistic electrons at a photonic structure

John Breuer

Dissertation
an der Fakultät für Physik
der Ludwig–Maximilians–Universität
München

vorgelegt von
John Breuer
aus Chemnitz

München, den 1. Juli 2013

Erstgutachter: Prof. Dr. Peter Hommelhoff
Zweitgutachter: Prof. Dr. Jörg Schreiber
Tag der mündlichen Prüfung: 29. August 2013

To Julia, Trey and Lukas

Zusammenfassung

In dieser Arbeit berichten wir über die Beobachtung der dielektrischen Laserbeschleunigung nichtrelativistischer Elektronen mithilfe des inversen Smith-Purcell Effekts bei optischen Wellenlängen. Wenn die Phasengeschwindigkeit von evaneszenten Wellen nahe periodischer Gitterstrukturen mit der Elektronengeschwindigkeit übereinstimmt, kann eine vorwärtsgerichtete elektrische Feldkomponente das Elektron kontinuierlich beschleunigen. Dieser Effekt tritt jedoch nur im Nahfeld passender photonischer Strukturen auf, d.h., dass der Elektronenstrahl die Struktur in Abständen, die kleiner als die Wellenlänge sind, passieren muss.

Für die Beschleunigung nichtrelativistischer 28 keV Elektronen verwenden wir die dritte Raumharmonische eines Quarzgitters, die mittels Lichtpulsen eines Titan-Saphir-Oszillators angeregt wird. Wir messen einen maximalen Energiegewinn von 280 eV, was einem Beschleunigungsgradienten von 25 MeV/m entspricht. Dieser Wert ist vergleichbar mit dem Gradienten heutiger Radiofrequenz-Linearbeschleuniger. Um diese Beschleunigung zu erfahren, passieren die Elektronen die Gitteroberfläche in einem Abstand von weniger als 100 nm.

Im Rahmen dieser Arbeit beschreiben wir die Theorie der Elektronenbeschleunigung im Nahfeld von Gitterstrukturen und diskutieren Simulationsergebnisse zu dieser dielektrischen Laserbeschleunigung. Unsere Messergebnisse stimmen sehr gut mit den Simulationen überein und bestätigen deshalb die direkte Beschleunigung im Lichtfeld. Zusätzlich diskutieren wir die Elektronenbeschleunigung in Doppelgitterstrukturen, das Dephasieren nichtrelativistischer Elektronen, sowie den Raumladungseffekt, der den Spitzenstrahlstrom in diesen neuartigen, auf Mikrostrukturen basierenden Beschleunigern begrenzt.

Die hier verwendeten photonischen Gitterstrukturen können direkt aneinandergereiht werden und erfüllen damit die Voraussetzung für skalierbare Linearbeschleuniger. Außerdem sind unsere Strukturen kompatibel mit den Mikrostrukturen, an denen die dielektrische Laserbeschleunigung *relativistischer* Elektronen zeitgleich durch unsere Kollegen in Stanford demonstriert wurde. Das Potenzial dielektrischer Laserbeschleuniger liegt in dem bis zu zwei Größenordnungen höheren Beschleunigungsgradienten verglichen mit konventionellen Beschleunigereinrichtungen, was sich letztendlich auf die größere Zerstörschwelle dielektrischer Materialien bei optischen Wellenlängen im Vergleich zu Metallen im Radio- und Mikrowellenbereich zurückführen lässt, die eine erhöhte Oberflächenspannungsfestigkeit zur Folge hat. Dieser erhöhte Beschleunigungsgradient könnte den Bau von deutlich kompakteren und kostengünstigeren Beschleunigern erlauben. Wir geben einen Ausblick

auf den möglichen Aufbau solcher zukünftiger optischen Beschleuniger und auf deren potentiellen Anwendungen in kompakten Freie-Elektronen-Lasern.

Abstract

This thesis reports on the observation of dielectric laser acceleration of non-relativistic electrons via the inverse Smith-Purcell effect in the optical regime. Evanescent modes in the vicinity of a periodic grating structure can travel at the same velocity as the electrons along the grating surface. A longitudinal electric field component is used to continuously impart momentum onto the electrons. This is only possible in the near-field of a suitable photonic structure, which means that the electron beam has to pass the structure within about one wavelength.

In our experiment we exploit the third spatial harmonic of a single fused silica grating excited by laser pulses derived from a Titanium:sapphire oscillator and accelerate non-relativistic 28 keV electrons. We measure a maximum energy gain of 280 eV, corresponding to an acceleration gradient of 25 MeV/m, already comparable with state-of-the-art radio-frequency linear accelerators. To experience this acceleration gradient the electrons approach the grating closer than 100 nm.

We present the theory behind grating-based particle acceleration and discuss simulation results of dielectric laser acceleration in the near-field of photonic grating structures, which is excited by near-infrared laser light. Our measurements show excellent agreement with our simulation results and therefore confirm the direct acceleration with the light field. We further discuss the acceleration inside double grating structures, dephasing effects of non-relativistic electrons as well as the space charge effect, which can limit the attainable peak currents of these novel accelerator structures.

The photonic structures described in this work can be readily concatenated and therefore represent a scalable realization of dielectric laser acceleration. Furthermore, our structures are directly compatible with the microstructures used for the acceleration of relativistic electrons demonstrated in parallel to this work by our collaborators in Stanford. The potential of dielectric laser accelerators lies in the larger attainable acceleration gradients resulting in a more compact design as well as a lower cost of these devices compared with conventional accelerator facilities. This size reduction by potentially a factor of 100 is owed to the two orders of magnitude larger damage threshold of dielectric materials as compared to metals. We present an outlook towards the design of an envisioned large-scale dielectric laser accelerator and its possible application in future compact free electron lasers.

Table of contents

Introduction

Particle accelerators represent a key tool for the discovery of subatomic physics. In particle accelerators charged particles, such as electrons, protons or ions, are accelerated to high energies. Collisions of those high energy beams in particle colliders allow insight into the smallest structures and fundamental forces of the universe. The most recent groundbreaking result is the discovery of a new particle, most likely the Higgs boson, at the Large Hadron Collider (LHC) at CERN in Geneva, Switzerland [1, 2].

A second important application is the use of particle accelerators as sources of soft or hard X-ray radiation. These X-rays, which can be either incoherent (synchrotron radiation) or coherent (free electron laser radiation), are used for various experiments in biology, medicine and materials science to explore the structure of our surrounding matter [3].

A third field of application of high energy particle beams is particle therapy, where beams of protons, neutrons or ions are used for cancer treatment [4]. The advantage of using particle beams in comparison with conventional radiation therapy (i.e., with X-rays or γ-rays) is that particles can penetrate deep into human tissue and deposit their energy in a very localized area without damaging the overlying tissue. On the contrary, electromagnetic radiation therapy is characterized by an exponentially decaying energy deposit as a function of penetrated depth. Therefore tumors that are located deep inside the body cannot be treated without damaging the surrounding tissue with photon beams, whereas in particle therapy tumors can be selectively destroyed.

There is a limited number of particle accelerators around the world, because of their large size and high cost. Facility users compete for beam time creating a major bottleneck for scientific discoveries and medical treatments. This explains the increasing interest in advanced accelerator technology that may lead to more compact and to more affordable machines that open up the opportunities of particle accelerators to a wide community [5]. It has been envisaged that the next generation of particle accelerators is based on laser technology providing electromagnetic fields with very large amplitude [6–11]. These fields can be used to accelerate charged particles to high energies on comparably short distances. Advanced accelerator technologies include, e.g., plasma-based particle acceleration and dielectric laser acceleration. While plasma-based particle acceleration has progressed rapidly over the last two decades and represents the most mature scheme of advanced particle acceleration, dielectric laser acceleration is still in an early stage of development.

In this work we present the first experimental demonstration of laser-based acceleration of non-relativistic electrons in the vicinity of a dielectric grating structure. It has

been suggested that dielectric laser accelerators, which represent the optical counterpart of conventional radio frequency accelerators, can lead to a size reduction in linear accelerators up to two orders of magnitude [12]. Grating structures used in this work can be concatenated in a straightforward manner and are directly compatible with structures used to accelerate relativistic electrons [13]. This inter-compatibility is important for the realization of scalable and modular linear accelerators, in which the non-relativistic structures, presented here, represent an integral part of the electron injector to bridge the gap between the electron source and the relativistic structures. In this proof-of-concept experiment we have accelerated 28 keV electrons and measured a maximum acceleration gradient of 25 MeV/m, already comparable with state-of-the-art radio frequency accelerator facilities and three orders of magnitude larger than reported in previous experiments that were based on a similar effect. Besides their application in future linear accelerators the structures described here may find use in ultrafast electron microscopy and electron diffraction experiments.

This thesis is organized as follows:

In Chapter 1 we briefly review the physics of charged particle acceleration. We discuss the Lawson-Woodward theorem, introduce the important particle beam quantities, emittance and brightness, and present a brief overview of radio frequency acceleration structures, which are the core of conventional particle accelerators. We further present a survey of the physics and recent progress in advanced accelerator technology like dielectric laser acceleration, plasma-based acceleration and other laser-based particle acceleration schemes.

In Chapter 2 we present the theory behind grating-based particle acceleration, based on the inverse Smith-Purcell effect. We further estimate the dephasing length of non-relativistic particles.

In Chapter 3 we show general simulation results of particle acceleration at single and double grating structures. We also present the simulations for the single fused silica grating that was used in the experiment.

In Chapter 4 we describe the experimental setup including the geometry of the fused silica grating as well as the detection scheme, which we have used to measure the accelerated electrons. We further present and discuss the measurement results.

In Chapter 5 we discuss the design of large-scale dielectric laser accelerators providing energies up to 1 TeV. We estimate bunch charge limitations due to the space charge effect, as well as the length and power consumption of such devices. We further give an outlook on possible applications in future radiation sources such as free electron lasers.

In Chapter 6 we conclude and define goals for following experiments.

Chapter 1

Physics of charged particle acceleration

Charged particles can be accelerated either with electrostatic or oscillating electromagnetic fields. The interaction of a particle with the fields takes place via the Lorentz force

$$\mathbf{F} = q\left(\mathbf{E} + \mathbf{v} \times \mathbf{B}\right), \tag{1.1}$$

with the particle's charge q, the particle's velocity $\mathbf{v}$, the electric field $\mathbf{E}$ and the magnetic field $\mathbf{B}$.

In electrostatic accelerators charged particles are accelerated by a static electric field. The maximum attainable voltage in such devices is limited by high-voltage breakdown to $\sim$30 MV [14]. Electrostatic accelerators comprise, amongst others, cathode ray tubes, X-ray tubes and tandem accelerators, in which after crossing the acceleration distance negatively charged ions pass a thin foil to strip off electrons, so that the positive ions can be further accelerated [15]. Due to the simple design and comparably small cost electrostatic accelerators are a widespread research tool at universities around the world.

Particle accelerators operating with oscillating fields exploit an electromagnetic wave with a phase speed equal to the particle's velocity and an electric field component parallel to the particle's trajectory. This acceleration scheme, which therefore exploits the synchronicity between the fields and the particle motion, has the advantage that the maximum achievable particle energy is not limited by high-voltage breakdown, in contrary to electrostatic accelerators.

The oscillating field particle accelerators can be classified into circular and linear accelerators. Circular accelerators include cyclotrons, betatrons and synchrotrons. Particles, which are forced on circular orbits, emit synchrotron radiation resulting in an energy loss. The total radiated power can be calculated with Larmor's formula [16]

$$P = \frac{q^2 c}{6\pi\epsilon_0}\frac{\beta^4}{\rho^2}\left(\frac{E_{\mathrm{kin}}}{m_0 c^2} + 1\right)^4, \tag{1.2}$$

with the speed of light c, the vacuum permittivity ϵ_0, the orbit radius ρ, the particle's velocity $\beta = v/c$, the kinetic energy E_{kin} and the particle's rest mass m_0. The associated

energy loss limits the maximum achievable practical energy in circular devices. As the synchrotron radiation power is proportional to $1/\rho^2$ it is evident that the diameter of the facility has to increase in order to reach higher energies. For example, the diameter of the Large Hadron Collider is 8.4 km and therefore protons lose 2.2 keV per cycle, assuming an energy of $E_{\text{kin}} = 7\,\text{TeV}$. Electrons have a much smaller mass than protons, which results in a much smaller attainable final energy for synchrotrons of identical size, because the radiation loss scales with $1/m_0^4$. Although representing the high energy frontier in circular accelerators, synchrotron radiation is also a source of high brilliance, high brightness, high energy, collimated and incoherent X-ray radiation with numerous applications in materials science, e.g., in X-ray crystallography [3].

This work will focus on linear particle acceleration. In a linear accelerator (linac) charged particles are accelerated along a straight line with synchronously oscillating electromagnetic fields. It can be shown that radiation losses in a linac can be neglected unless the acceleration gradient is impractically large, e.g., on the order of $10^{14}\,\text{MeV/m}$ for electrons [16]. The largest operating linac at the SLAC National Accelerator Laboratory is about 3.2 km long and accelerates electrons or positrons to 50 GeV [17]. This is small compared to the historical Large Electron-Positron Collider at CERN, which measured a circumference of 27 km and achieved maximum energies around 100 GeV [18].

In this chapter we discuss basic principles of charged particle acceleration with oscillating electromagnetic fields. We state the general acceleration theorem and introduce the two important quantities of beam emittance and brightness, which characterize the quality of particle beams. We then review conventional radio frequency acceleration structures and their limitations, present the concept of dielectric laser acceleration and discuss plasma-based acceleration schemes as well as other laser-driven acceleration mechanisms.

1.1 Lawson-Woodward theorem

The Lawson-Woodward theorem [19–22], also known as the general acceleration theorem, explores the conditions under which charged particle acceleration with oscillating fields can occur. It states that the net energy gain of a particle interacting with electromagnetic fields is zero under the following circumstances:

1. the interaction takes place in vacuum (unity refractive index),
2. no boundaries or surfaces are present, i.e., the distance from any source of field is large compared to the wavelength (far-field),
3. the particle is moving in a region without other free charges,
4. the particle is highly relativistic ($\beta \sim 1$) (this condition can be relaxed [21]),
5. no static electric or magnetic fields are present,
6. the interaction region is infinitely large, **and**

7. non-linear forces (e.g., the ponderomotive force [23]) are neglected.

The simple explanation for this theorem is that electromagnetic waves in vacuum traveling at the speed of light are transversely polarized. Hence, a wave propagating along the particle's trajectory cannot cause acceleration. If the wave is traveling under an angle to the particle's trajectory, the particle experiences an oscillating field whose effect averages to zero over time. A rigorous proof is presented in [22].

Despite efforts to contradict the Lawson-Woodward theorem, for example, by using unipolar pulses [24–29], it could not be disproved: In order to accelerate relativistic particles in vacuum with oscillating electromagnetic fields one or more of the above-mentioned conditions must be violated.

1.2 Beam emittance and brightness

The emittance of a charged particle beam is a measure of the beam quality. It describes the size and energy spread of an ensemble of charged particles, and is related to the phase-space volume occupied by the particles in the beam. In one dimension the root-mean-square (rms) emittance is defined as [30]

$$\tilde{\epsilon}_x = \sqrt{\overline{x^2}\,\overline{x'^2} - \overline{xx'}^2}, \tag{1.3}$$

in terms of the moments of the particle distribution in the x-x' trace space, with the particle position x and the divergence x'. The $\overline{xx'}$ term describes a correlation between x and x'. It vanishes at the waist of an ideal, focused particle beam, where the emittance is simply given by the product of the rms beam size $(\overline{x^2})^{1/2}$ and divergence $(\overline{x'^2})^{1/2}$. The emittance is usually measured in units of mm mrad. Sometimes the dimensionless angle is omitted, i.e., $1\,\text{mm mrad} = 1\,\mu\text{m}$, which we will apply throughout this work. The transverse emittances $\tilde{\epsilon}_x$ and $\tilde{\epsilon}_y$ of a particle beam propagating into the z-direction are usually of main interest, but in the case of longitudinally bunched beams the emittance $\tilde{\epsilon}_z$, related to a longitudinal energy spread, has to be included to describe the overall quality of the beam.

The emittance can be made arbitrarily small, e.g., by collimating the beam with an aperture, which consequently also reduces the beam current. Therefore a better measure for the beam quality is the brightness $\hat{B}$, which is defined as beam current I_b over transverse emittance $\tilde{\epsilon}_x\tilde{\epsilon}_y$, i.e.,

$$\hat{B} = \frac{I_\text{b}}{8\pi^2\tilde{\epsilon}_x\tilde{\epsilon}_y}. \tag{1.4}$$

Emittance and brightness depend on the particles' energy in the beam, because increasing the longitudinal momentum reduces the divergence of the beam. Therefore, in order to compare particle beams of different energy, the normalized rms emittance $\tilde{\epsilon}_\text{n} = \beta\gamma\tilde{\epsilon}$ and normalized brightness $\hat{B}_\text{n} = \hat{B}/(\beta\gamma)^2$ should be used, with the Lorentz factor $\gamma = (1-\beta^2)^{-1/2}$. It can be explained by Liouville's theorem that these normalized

quantities are conserved in an ideal system with linear forces as long as dissipation and interactions between the particles are neglected [30]. Although the total emittance, i.e., the product of transverse and longitudinal emittance $\tilde{\epsilon}_x\tilde{\epsilon}_y\tilde{\epsilon}_z$ is conserved, emittance can be exchanged from one coordinate to another. For example, transverse to longitudinal emittance exchange schemes have been proposed in [31–33].

Because the normalized emittance and brightness are conserved quantities, we note that the beam quality ultimately depends on the electron source. It can be shown that the intrinisic or thermal emittance of an electron emitter (e.g., a photocathode) scales linearly with the intrinsic energy spread of the electrons at the emission site and with the source size, i.e., the dimension of the area from which the electron's are emitted [34]. Therefore recently there has been a lot of interest in ultrasharp needle emitters with an intrinsic emittance $<1\,\mathrm{nm}$ [33, 35–40].

We also note that there is an ultimate limit on the brightness of an electron beam, because the maximum phase-space density of fermions is given by the Pauli exclusion principle. This quantum limit for the maximum normalized brightness of an electron beam can be written as [41]

$$\hat{B}_\mathrm{Q} = \frac{2m_\mathrm{e}^2c^2e\Delta E}{h^3}, \tag{1.5}$$

with the electron mass m_e, the electron charge e, the Planck constant h and the energy spread of the beam ΔE. For example, a beam with an energy spread of $\Delta E = 1\,\mathrm{eV}$ can exhibit a maximum brightness of $1.3 \cdot 10^{19}\,\mathrm{A/(m^2sr)}$.

1.3 Radio frequency linear accelerators

The dielectric acceleration structures exploited in this work and described in Chapters 3 and 4 are conceptually similar to conventional radio frequency (RF) acceleration structures, which we briefly describe here. This section is based on [42], which represents an excellent textbook on the physics of RF linacs.

The concept of RF linacs has been introduced by Ising in 1924 [43]. The first experimental realization by Wideröe [44] was the precursor of all modern RF linacs. The Wideröe linac, schematically illustrated in Figure 1.1 (a), is based on alternating RF voltages (frequency f, wavelength $\lambda = c/f$) applied to a sequence of drift tubes, whose length of $\beta\lambda/2$ is matched to the velocity of an accelerating particle, so that the particle always experiences an accelerating field when passing the gaps between the drift tubes. The first linac operated with an RF voltage of 25 kV at a frequency of 1 MHz and was used to accelerate singly charged potassium ions to an energy of 50 keV. In contrast to previous electrostatic accelerators the entrance and exit of the linac were on ground potential and the energy gain of the particles was not limited by the applied voltage. In principle an infinite number of such structures can be connected in series leading to an unlimited final energy.

In practice, however, the Wideröe linac is not suitable for the acceleration of particles traveling close to the speed of light because the length of the drift tubes would equal half

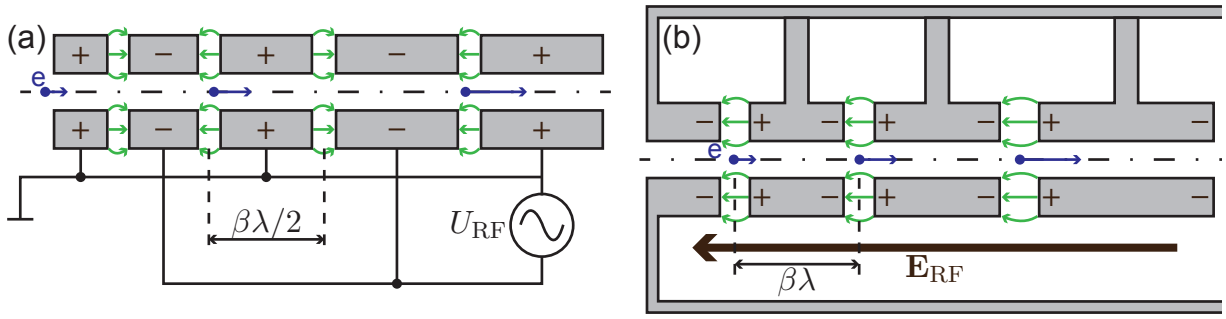

Figure 1.1: (a), Schematic of the Wideröe linac based on drift tubes with length $\beta\lambda/2$, to which an alternating RF voltage U_{RF} is applied. (b), Conceptual picture of the Alvarez drift-tube linac which consists of a series of drift tubes placed inside an RF cavity. The drift tubes shield the passing electrons from experiencing the decelerating phase of the cavity field $\mathbf{E}_{\mathrm{RF}}$. The direction of the accelerating field between the drift tubes is indicated by the green arrows.

the wavelength of the driving RF field, which creates resonant antennas with high power losses. Moreover, for practical sizes of the linac the frequency should be increased into the gigahertz range, where microwave technology has to be employed. The availability of high power microwave sources, such as klystrons, developed for radar applications during World War II, laid the foundation for more efficient RF acceleration structures. The concept of the drift-tube linac (DTL) was proposed by Alvarez [45] and realized as a proton linac in 1955 [46, 47]. It consists of a cylindrical microwave cavity, which enhances the applied RF field and contains a series of drift tubes that shield the protons from the decelerating field. A schematic is depicted in Figure 1.1 (b). The main difference between the Wideröe linac and the Alvarez DTL is that in the Wideröe linac an RF *voltage* is applied to the drift tubes with a cell length of $\beta\lambda/2$ leading to high power losses as $\beta \to 1$, whereas in the Alvarez DTL an RF *field* is applied to the drift tubes with a cell length of $\beta\lambda$ leading to more efficient acceleration of relativistic particles. Because the electric field along each conducting drift tube is uniform and oscillating at the frequency f, the DTL is considered a standing-wave structure.

Around the same time, at which the DTL has been demonstrated, a different, efficient acceleration structure has been proposed, which was called the disk-loaded or iris-loaded waveguide [48], shown in Figure 1.2. It was later implemented in the 3-km-long Stanford Linear Accelerator Center (SLAC) linac. In the iris-loaded traveling-wave acceleration structure the RF power is fed into an input port and an electromagnetic traveling-wave propagates synchronously with the particles along the waveguide. The periodically-spaced conducting disks inside the waveguide assure that the phase velocity of the accelerating mode matches the particles' velocity.

The main difference between standing-wave and traveling-wave structures is the duration which is needed to fill the cavities with RF power, also known as the filling time. Typical filling times for traveling-wave structures are in the sub-microsecond range, whereas

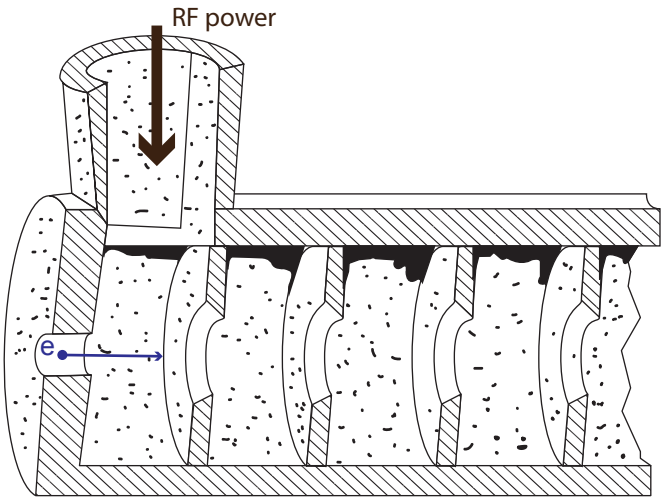

Figure 1.2: Disk-loaded traveling-wave structure with RF input port at the top. Electrons traveling along the axis are accelerated by the electromagnetic field of the traveling wave. Taken from [42].

standing-wave structures have filling times on the order of tens of microseconds [49]. Hence, traveling-wave structures are more efficient for short-pulsed operation ($<1\,\mu$s), which enables larger acceleration gradients, because the maximum attainable RF field increases with decreasing pulse duration.

Besides the standing-wave (DTL) and traveling-wave (iris-loaded waveguide) structures there are also independent-cavity linacs, in which a series of quarter-wave or half-wave resonators is independently driven by their individual RF generators. This enables the possibility to apply specific cavity field amplitudes and phases, which offers flexibility and is therefore often employed in heavy ion linacs where particles with different charge-to-mass ratios are accelerated [50].

RF linacs operate either with room-temperature (copper) or superconducting (niobium) acceleration structures. Superconducting structures have the advantage of five orders of magnitude smaller surface resistance compared to room-temperature copper structures. Together with the power needed for the cooling to cryogenic temperatures, this leads to an overall power savings factor on the order of 100 [51]. Due to the much smaller dissipated power, superconducting cavities achieve much larger quality factors on the order of 10^9–10^{10} in comparison with $\sim 10^4$ for copper cavities [49]. This also implies much longer filling times in superconducting structures up to the millisecond range making them more suitable for longer pulsed or continuous-wave (cw) operation.

The maximum attainable acceleration gradients in RF linacs are limited by RF breakdown phenomena [52]. Room-temperature structures have been demonstrated with acceleration gradients exceeding 100 MeV/m [53–55]. The physics of RF breakdown in those structures is still not fully understood, but important factors include field emission and local pulsed heating [56]. Superconducting structures can reach acceleration gradients

up to 50 MeV/m [57, 58] ultimately limited, amongst others, by electron multipacting, normal-conducting defects and electron field emission [51, 52].

Both room-temperature and superconducting technologies continue to coexist as they have their specific advantages and disadvantages. Proposals for the next generation of particle colliders are based on normal conducting structures with acceleration gradients around 100 MeV/m, as planned for the Compact Linear Collider (CLIC) [59], as well as on superconducting cavities with gradients around 30 MeV/m, as planned for the International Linear Collider (ILC) [60].

1.4 Dielectric laser acceleration

The development of short pulse lasers with high peak electric fields kindled the vision of a new generation of linear accelerators (linacs) already half a century ago [6], just two years after the first successful demonstration of laser operation in 1960 [61]. Shimoda proposed to use a cylindrical tube made of a gain medium and to excite an accelerating mode inside the tube by optical pumping from the outside [6]. However, excitation of such a synchronous mode turns out to be challenging, as has been noted in [7, 62].

Takeda *et al.* proposed to use the near-field of a periodic grating structure for particle acceleration in 1968 [7]. This mechanism is also known as the inverse Smith-Purcell effect [63], which has been observed at a metal grating of 250 μm period using a terahertz radiation source ($\lambda = 496\,\mu$m) [64,65]. However, the measured acceleration gradients were too small ($\sim$10 keV/m) to compete with RF linacs. Eventually, the maximum attainable acceleration gradients for metal gratings are limited by the damage threshold of the metals to $\sim$100 MeV/m, similar to RF structures.

Dielectric materials at optical frequencies withstand one to two orders of magnitude larger fields [69–71] suggesting dielectric laser accelerators (DLAs) with acceleration gradients exceeding 1 GeV/m [11, 66–68, 72–77]. We define dielectric laser acceleration as all particle acceleration schemes in vacuum that exploit the near-field of a dielectric boundary excited by laser light. Examples of proposed DLA structures are shown in Figure 1.3. Dielectric acceleration structures represent the optical counterpart of RF structures and include standing-wave [11, 66, 75] and traveling-wave [67, 72, 73, 77] waveguides, which are exploited to create electromagnetic modes that travel synchronously with the accelerating particles. Due to the roughly four orders of magnitude smaller wavelength of the driving field, optical accelerators also have four orders of magnitude smaller dimensions than conventional RF structures. DLA structures can be side-pumped by a laser and their resonating nature allows very efficient excitation of the accelerating mode. However, these structures usually have quality factors of around 10^3, resulting in filling times on the order of tens of picoseconds, which prevents the compatibility with ultrashort laser pulses.

Plettner *et al.* have proposed a non-resonating dielectric double grating structure which enables ultrashort-pulsed (<100 fs) operation [68]. This structure consists of two opposing dielectric gratings whose accelerating mode is excited by two counterpropagating laser beams, as shown in Figure 1.3 (c). The advantage of ultrashort-pulsed operation is the

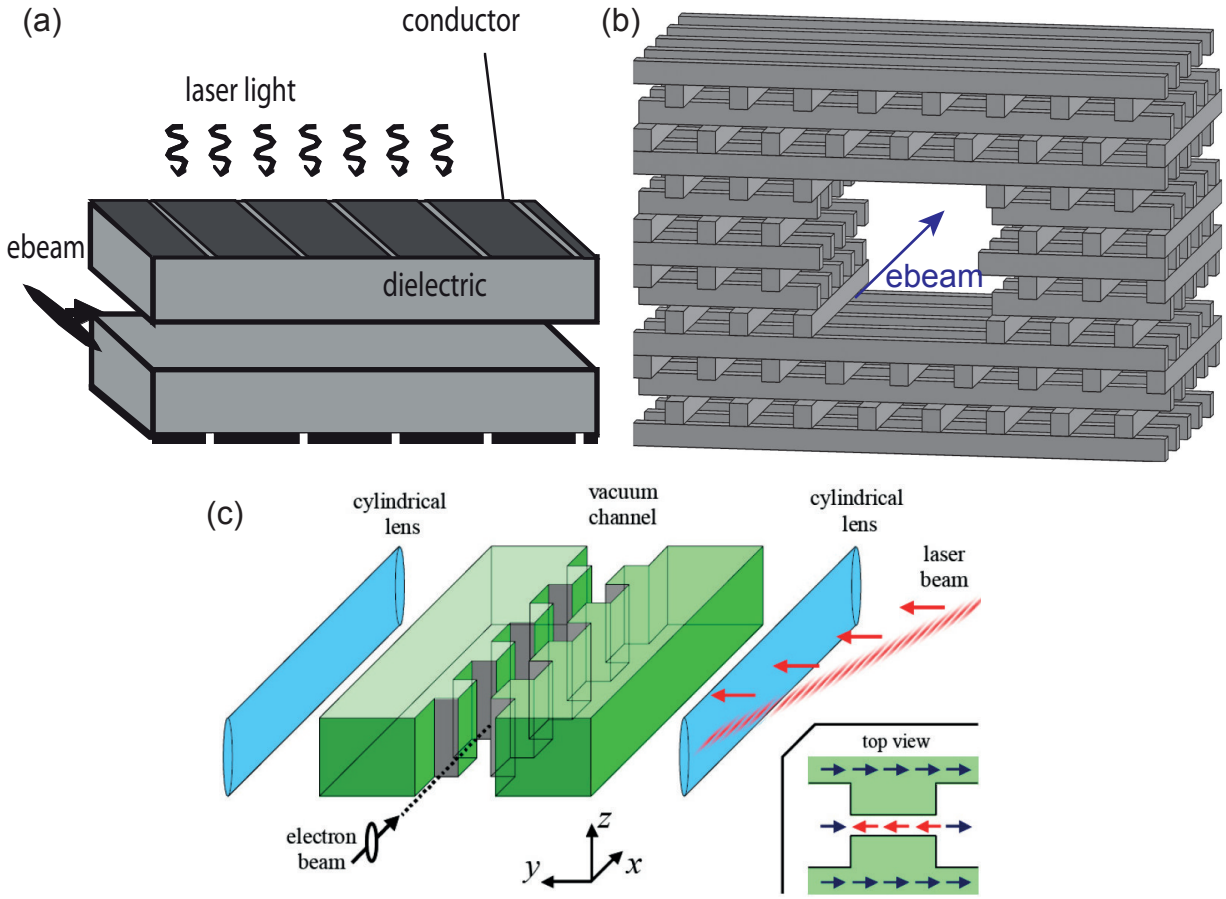

Figure 1.3: Proposed dielectric laser accelerator (DLA) structures. (a), Side-coupled slab-symmetric dielectric structure designed to be driven at terahertz frequencies. Taken from [66]. (b), Photonic crystal waveguide (so-called woodpile structure) which supports a traveling wave that can be used for particle acceleration. Taken from [67]. (c), DLA scheme based on transparent double grating structures. Contrary to other approaches this structure is non-resonating (i.e., the laser can pass the structure and reform a plane wave at the opposite grating) and therefore allows ultrashort-pulsed operation. Taken from [68].

possibility to drive these structures at very large repetition rates in the gigahertz range, which broadens the spectrum of possible applications. Based on this concept, accelerating, deflecting and focusing structures have been proposed as components for an envisioned all-optical dielectric-based table-top linac [78–80].

Compared with plasma-based accelerators, discussed in the next section, DLAs have the advantage of supporting ultralow emittance (<1 nm) bunched particle beams at the cost of a much lower (sub-pC) bunch charge. However, DLA structures in combination with moderate power laser systems facilitate gigahertz repetition rates, compensating for the lower bunch charge. For comparison, plasma-based accelerators require petawatt lasers that currently have repetition rates on the order of 1-10 Hz.

1.5 Plasma-based acceleration schemes

The maximum acceleration gradient of the particle acceleration schemes, discussed so far, is ultimately limited by the damage threshold of the materials, which are used to confine the electromagnetic fields. However, there is an acceleration mechanism which circumvents this limitation, namely plasma-based acceleration. Here a plasma wave with a very large electric field strength is excited by, e.g., an intense laser pulse or an electron beam. Particles injected into this plasma wave experience acceleration gradients up to 100 GeV/m. A conceptual picture of the beam-driven plasma wakefield accelerator is shown in Figure 1.4. Good reviews on laser-driven plasma-based acceleration are given in [81, 82].

A plasma consists of a fluid of electrons and positively charged ions. Applying an external field to the plasma leads to local charge separation and the restoring Coulomb force generates a plasma wave. Hence, the third condition of the Lawson-Woodward theorem is violated due to the presence of free charges (Section 1.1). The maximum electric field of the plasma wave is determined by the wave breaking limit above which wave propagation cannot occur. The cold non-relativistic wave breaking field is $E_0 = cm_e\omega_{pl}/e$ [84], with the plasma frequency $\omega_{pl} = \sqrt{4\pi n_0 e^2/m_e}$ and the plasma density n_0. It can be written as

$$E_0(\mathrm{V/m}) \simeq 96\sqrt{n_0(\mathrm{cm^{-3}})}. \tag{1.6}$$

Hence, for a density of $n_0 = 10^{18}\,\mathrm{cm^{-3}}$ a field of 96 GV/m can be reached. Taking relativistic effects and nonlinearities into account suggests that plasmas can sustain even slightly larger fields [82]. Another important parameter is the plasma wavelength $\lambda_{pl} = 2\pi c/\omega_{pl}$. For example, $\lambda_{pl} = 33\,\mu$m for $n_0 = 10^{18}\,\mathrm{cm^{-3}}$. This implies that very short bunches of particles with bunch durations below 100 fs ($< \lambda_{pl}/c$) can be generated.

The laser-driven plasma-based accelerator (LPA) has been proposed in the late 1970s [9]. A short laser pulse with high intensity ($>10^{18}\,\mathrm{W/cm^2}$) is used to excite the plasma wave, i.e., the ponderomotive force drives the electrons away from the laser pulse. In essence, the plasma acts as an efficient transformer of the transverse laser electric field into the longitudinal field of the plasma wave, which can be used for particle acceleration.

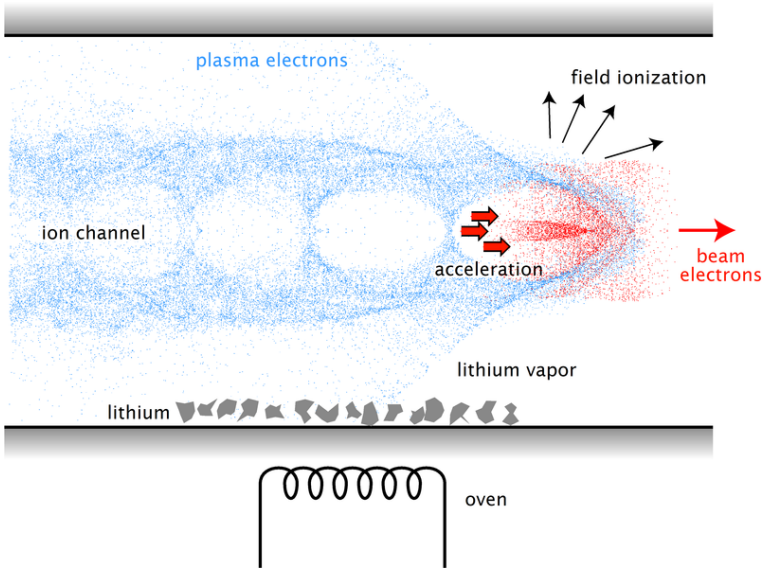

Figure 1.4: Schematic illustration of the plasma wakefield accelerator. A lithium vapor is generated inside a heat-pipe oven. An electron beam, which passes through, field ionizes the lithium vapor (i.e., creates a plasma) and drives out the plasma electrons, which are pulled back towards the beam axis by the Coulomb force of the lithium ions. The resulting longitudinal electric field of the plasma wave accelerates electrons that at the rear of the so-called bubble. Taken from [83].

The success of LPAs over the last two decades is closely connected to the rapid progress in ultrafast and high power laser technology, especially the invention of chirped-pulse amplification [85].

There is a variety of different approaches on how the plasma wave can be excited. For example, in laser wakefield acceleration a single laser pulse is used whereas in laser beat-wave acceleration the difference frequency between two laser pulses is used to resonantly excite the plasma wave. There are also different schemes on how electrons can be injected into the plasma wave, e.g., by self-injection or external injection. For more details we refer the reader to [82].

In the early years of LPAs electrons have been accelerated up to energies of a few tens of MeV with bunch charges on the order of a few nC and an emittance of below $10\,\mu$m [86], comparable with RF accelerators. However, the energy of the accelerated bunch spread from zero to the MeV-range with only a small fraction of the bunch charge being accelerated up to the highest energies. A major advance was the production of monoenergetic electron beams with energies up to $\sim$100 MeV and energy spreads of a few percent in 2004 [87–89]. The key improvement was to increase the acceleration length, thereby allowing the electrons to interact with the plasma wave over a longer distance. This can be achieved either by weaker focusing of the laser leading to an increase of the Rayleigh length [87, 89], or by using a preformed plasma channel [88].

The plasma wave has a phase velocity smaller than the speed of light and hence electrons that are accelerated to relativistic energies eventually outrun the plasma wave. When the resulting phase slip exceeds half the plasma wavelength, the electron experiences a decelerating force. The corresponding dephasing length can be approximated with $L_\mathrm{d} = \lambda_\mathrm{pl}^3/\lambda^2 \propto (n_0)^{-3/2}$, with the driving laser wavelength λ. L_d is the maximum distance for acceleration. Multiplying with the electric field of the plasma wave (Equation 1.6) yields a maximum energy gain on the order of $\Delta W(\mathrm{GeV}) \simeq I_0(\mathrm{W/cm^2})/n_0(\mathrm{cm^{-3}})$, with the laser peak intensity I_0 [81]. For example, using a laser with a peak intensity of $10^{18}\,\mathrm{W/cm^2}$ and a plasma density of $10^{17}\,\mathrm{cm^{-3}}$ results in a maximum energy gain of 10 GeV in a single-stage LPA. Using plasmas with a lower density increases the maximum energy gain and the dephasing length, and therefore allows to accelerate electrons over longer distances, which consequently reduces the energy spread. This was the key to another milestone in LPAs in 2006 with the production of a high quality electron beam with an energy of $\sim$1 GeV, a few percent energy spread, a bunch charge of 30 pC and an emittance in the μm range using a 3 cm-long plasma capillary [90]. Recently, monoenergetic 2 GeV electron bunches have been produced using petawatt laser technology [91].

Furthermore, electron bunches with bunch durations around 1 fs and peak currents of a few kA have been demonstrated [92] and progress has been made towards stable and reproducible beam generation [93, 94]. However, shot-to-shot fluctuations, which can be attributed to laser and plasma instabilities, are limiting the applicability and have prevented serious competition with conventional RF accelerator technology in current and planned linac facilities so far. Advances in technology will be required to control the laser and plasma parameters on the percent-level. Another big question is the scalability of

LPAs, i.e., the issue of building multistage LPAs in order to reach larger final energies. Despite first efforts to build a two-stage LPA [95, 96], there is no clear concept yet on how to concatenate multiple stages. Nevertheless, laser-driven plasma acceleration is definitely the most mature advanced concept of linear particle acceleration and will most likely soon be able to replace conventional RF linacs for certain applications, e.g., for a next generation light source, which we will discuss in Section 5.3.

A different plasma-based acceleration scheme is the so-called plasma wakefield acceleration (PWFA), schematically depicted in Figure 1.4 [97, 98]. Here the space-charge force of an electron beam (drive beam) is used to excite the plasma wave. The maximum energy gain of a PWFA is limited by the transformer ratio, which is the ratio of the energy gain to the initial drive beam energy. The transformer ratio can be on the order of two [81, 99]. Hence, twice the drive beam energy can be transferred to the accelerated electrons. The largest energy gains that have been observed in plasma-based accelerators are on the order of 50 GeV in a meter-scale plasma channel excited by a 42 GeV electron beam at SLAC [100]. A new PWFA scheme has been proposed, which may be able to produce electron beams with emittance as low as 50 nm [101]. On-going research in this area points towards a promising future.

1.6 Other laser-based acceleration schemes

Limiting the interaction region between an electromagnetic wave and a particle can lead to particle acceleration, in agreement with the Lawson-Woodward theorem, by violating the sixth condition in Section 1.1. When a laser is focused, there is always a longitudinal electric field component, which can be used for particle acceleration [102, 103]. However, the phase velocity of this accelerating field is larger than the speed of light and it has been shown that the acceleration distance is limited to $\sim\pi Z_\mathrm{R}$ [22], with the Rayleigh range $Z_\mathrm{R} = \pi w_\mathrm{l}^2/\lambda$ for a laser beam with waist w_l and wavelength λ. Accelerators based on a series of focusing lenses in combination with drift tubes, which shield the particle from experiencing the laser field outside the Rayleigh range, have been proposed [102]. Other schemes, in which the particle-light interaction is confined, employ focused higher order Gaussian modes [104] or a configuration of two crossed laser beams [12, 105]. Using radially polarized laser beams produces a strong longitudinal field component [106, 107]. First electron acceleration exploiting a radially polarized laser beam has recently produced a 25 keV electron beam with an acceleration gradient around 10 GeV/m [108, 109].

A different concept comprises the termination of the laser field with a boundary, illustrated in Figure 1.5 [110]. Based on this idea an experiment at SLAC demonstrated electron acceleration with a maximum acceleration gradient of 40 MeV/m using a dielectric boundary to limit the interaction distance between the laser and the electron beam [111, 112].

All particle acceleration mechanisms in vacuum support acceleration gradients which are eventually limited by the damage threshold of the materials that are used to confine the laser fields, e.g., lenses or mirrors, similarly to dielectric laser accelerators. Scalability

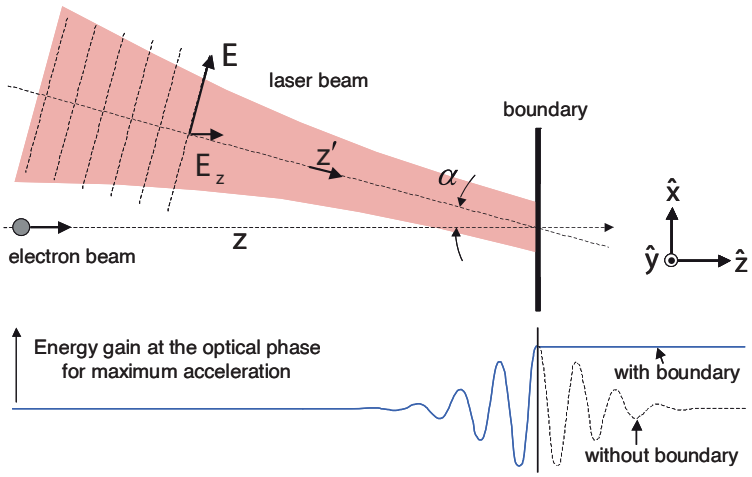

Figure 1.5: Schematic illustration of the laser acceleration at a dielectric boundary. The linearly polarized laser propagates under an angle to the electron beam to create a longitudinal electric field component. The electrons periodically gain and lose energy in the presence of this field. The effect would average to zero, if the interaction proceeded to infinity, according to the Lawson-Woodward theorem (Section 1.1). However, a dielectric boundary terminates the field at the focus of the laser and therefore allows a non-zero energy gain. Taken from [111].

of these schemes is questionable due to the rather large optical components needed to focus the ultra-high-intensity laser beams.

Another method for particle acceleration is the inverse Čerenkov effect [10, 113–115], which exploits that the phase velocity of light inside a medium is smaller than the vacuum speed of light. Therefore a particle traveling under an angle to a laser beam inside the medium can experience a synchronous accelerating force. The theoretically achievable maximum acceleration gradient in inverse Čerenkov accelerators is limited by ionization processes to a few hundred MeV/m [116].

The inverse free electron laser [8, 117–119] uses the interaction of an electron beam inside an undulator, i.e., a periodic magnetic field which forces the electrons on an oscillatory trajectory, with a laser beam propagating through the undulator. Besides the observed large acceleration gradients on the order of 100 MeV/m [119], inverse free electron lasers can also be used to produce microbunched electron beams [120].

Finally, a plasmon linac has been proposed which uses surface plasmon polaritons close to a metal surface to synchronously accelerate particles [121]. This idea is conceptually similar to DLAs with the exception that a metal and not a dielectric material is used. Open questions related to the plasmon linac include the maximum attainable acceleration gradient limited by the damage threshold of the metal surface as well as an efficient excitation scheme of the surface plasmons.

The development of laser-based particle acceleration schemes is closely connected to

the advances in laser technology over the past decades. Plasma-based accelerators require ultrahigh power (petawatt) laser systems, which are based on the principle of chirped pulse amplification [85], in order to generate GeV electron bunches with bunch charges on the order of a few nC. The emittance of these bunches is currently in the micrometer-range, comparable with RF accelerators. LPAs operate at repetition rates that do not exceed a few tens of hertz, limited by the high peak power laser systems. Revolutionizing ideas in laser technology are needed to push the repetition rate of LPAs into the kilohertz-regime [122].

On the other hand, dielectric laser accelerators operate in a different parameter range. DLAs require laser peak powers of up to 1 GW, enabling operation at very large repetition rates in the gigahertz-regime. The advantage of DLAs compared to plasma-based accelerators is the scalability, that is, the possibility to concatenate many DLA structures which can be driven by individual, but synchronized, lasers. Therefore the total power needed to produce highly relativistic particles can be distributed over many high-repetition-rate laser systems. However, an important prerequisite for successful DLA operation is the synchronization and phase-stabilization of the multiple laser systems, which has been demonstrated about 10 years ago [123,124], and is now routinely possible. A disadvantage of the DLA is the comparably low supported bunch charge (<pC). However, the large repetition rate in combination with the ultralow emittance of the electron beams ($\sim$nm) can compensate this drawback.

Yet another ground-breaking idea of laser-driven particle acceleration was proposed about one week prior to the submission of this thesis. The combination of plasma technology, high power lasers and the concept of periodic field reversal at grating structures lead to the proposal of electron acceleration at plasma gratings with acceleration gradients in the TeV/m-regime [125].

The recent progress and ongoing research in advanced accelerator technology points towards a promising future. It is not yet clear, which scheme will be best suited for applications like future light sources or linear colliders. Both LPAs and DLAs will be certainly useful schemes and most likely enable new applications, which we cannot foresee at this point.

This thesis focuses on dielectric laser acceleration, in particular non-relativistic DLA structures, which represent an integral part of large-scale optical accelerators. In the next chapter we elucidate the theory behind grating-based particle acceleration.

Chapter 2

Theory of grating-based particle acceleration

In this chapter we derive the properties of the evanescent fields close to a single grating and the forces exerted onto a particle that synchronously interacts with those fields. We further discuss the drawbacks of particle acceleration close to a single grating that led to the proposal of symmetric double grating structures. In the second part of this chapter we calculate the dephasing length, i.e., the maximum distance over which acceleration of non-relativistic particles takes place until the mismatch between the particle velocity and the phase velocity of the accelerating mode leads to deceleration of the particle. The discussion presented in this chapter follows [126].

2.1 Particle acceleration in evanescent electromagnetic fields

R. Palmer explored the electromagnetic fields above a single grating excited by a plane wave and derived conditions for particle acceleration within such fields for the first time in 1980 [62]. Following his discussion we analyze the fields close to an infinitely large plane, which is assumed to be a grating with grating period λ_p and grating vector $k_\mathrm{p} = 2\pi/\lambda_\mathrm{p}$, as shown in Figure 2.1. The diffraction of the incident wave at the grating excites spatial harmonics with wave vectors $\mathbf{k}_\parallel^\mathbf{n} = \mathbf{K} + n\mathbf{k}_\mathrm{p}$, with the in-plane projection of the incident wave vector $\mathbf{K}$ and the order number $n = 0, 1, 2, \ldots$ The electromagnetic field of the n-th mode $\mathcal{A}(\mathbf{r}, t) = (\mathbf{E}(\mathbf{r}, t), \mathbf{B}(\mathbf{r}, t))$ can be written as

$$\mathcal{A}(\mathbf{r}, t) = \mathcal{A}_\mathrm{n} e^{i(k_\perp^n z + \mathbf{k}_\parallel^\mathbf{n} \cdot \mathbf{r} - \omega t + \phi_0)}. \tag{2.1}$$

The total field above the grating surface comprises a Fourier series of all spatial harmonics.

We assume a single particle traveling parallel to the plane with the trajectory

$$\mathbf{r}(t) = \mathbf{v}t, \tag{2.2}$$

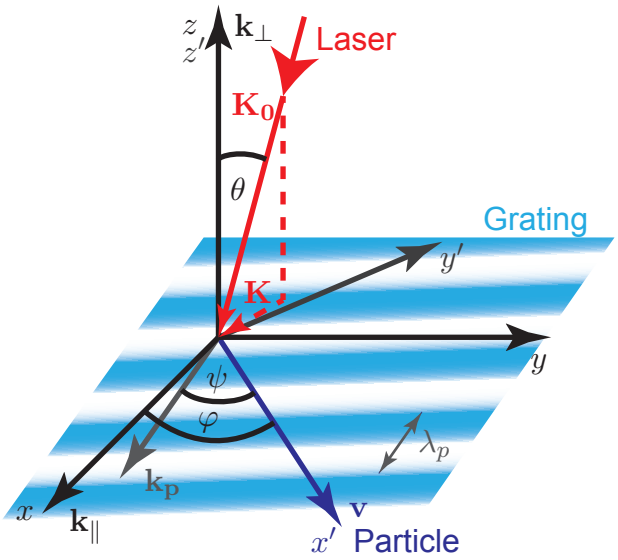

Figure 2.1: $\{x, y, z\}$ represents the coordinate system for a spatial harmonic, which is excited at an infinitely large grating with grating period λ_p and grating vector $k_\mathrm{p} = 2\pi/\lambda_\mathrm{p}$. $\{x', y', z'\}$ is the reference frame for a particle moving parallel to the grating surface. ψ is the angle between $\mathbf{k}_\mathrm{p}$ and the particle's velocity $\mathbf{v}$; φ is the angle between the propagation direction $\mathbf{k}_\parallel$ of the spatial harmonic and $\mathbf{v}$. The wave vector of the exciting plane wave is $\mathbf{K_0}$ with the in-plane projection $\mathbf{K}$. The in-plane wave vector of the n-th diffracted wave can be written as $\mathbf{k}_\parallel{}^n = \mathbf{K} + n\mathbf{k}_\mathrm{p}$ and hence φ is determined by $\mathbf{K_0}$ and ψ.

with the velocity $v = |\mathbf{v}| = \beta c$. The spatial harmonic has the in-plane phase velocity of

$$\mathbf{v}_{\mathrm{ph}} = \frac{\omega \mathbf{k}_{\parallel}}{k_{\parallel}^2}, \tag{2.3}$$

with the incident wave's angular frequency ω. Continuous motional control of the particle requires

$$\mathbf{v}_{\mathrm{ph}} \cdot \frac{\mathbf{v}}{v} = \frac{\omega}{k_{\parallel}} \cos\varphi \stackrel{!}{=} \beta c, \tag{2.4}$$

that is, the accelerating mode's phase velocity projected onto the particle's trajectory has to match the particle's velocity. This requirement yields the synchronicity condition

$$k_{\parallel} = \frac{\omega}{\beta c \cos\varphi} = \frac{k_0}{\beta \cos\varphi}, \tag{2.5}$$

with the wave vector in vacuum $k_0 = |\mathbf{K_0}| = \omega/c = 2\pi/\lambda$ and wavelength λ.

In the following we will consider only the synchronous mode for which Equation 2.5 is satisfied. We focus on acceleration in vacuum which implies that the fields have to satisfy the wave equation

$$\left(\nabla^2 - \frac{1}{c^2}\partial_t^2\right) \mathcal{A}(\mathbf{r}, t) = 0. \tag{2.6}$$

Substituting Equation 2.1 and omitting the superscript n, because all asynchronous modes are neglected, yields $k_{\perp}^2 + k_{\parallel}^2 - \omega^2/c^2 = 0$. Therefore

$$k_{\perp} = k_0 \sqrt{1 - \frac{1}{\beta^2 \cos^2\varphi}} = k_0 \sqrt{\frac{-(1 - \beta^2 \cos^2\varphi)}{\beta^2 \cos^2\varphi}} = i \frac{k_0}{\widetilde{\beta}\widetilde{\gamma}}, \tag{2.7}$$

with $\widetilde{\beta} = \beta \cos\varphi$ and $\widetilde{\gamma} = \left(1 - \widetilde{\beta}^2\right)^{-1/2}$. The accelerating fields perpendicularly to the particle trajectory always fall off exponentially, since $\beta < 1$ and γ is real. In other words, just evanescent fields contribute to the acceleration, in agreement with the violation of the second condition of the Lawson-Woodward theorem (Section 1.1). Particles have to pass the grating surface within a distance on the order of

$$\delta := \frac{i}{k_{\perp}} = \frac{\widetilde{\beta}\widetilde{\gamma}\lambda}{2\pi}, \tag{2.8}$$

to experience efficient acceleration. Synchronous steering (i.e., continuous motional control) of particles with $\beta \to 0$ is virtually impossible with this scheme.

Figure 2.2 shows the concept of synchronous particle acceleration exploiting the first and third spatial harmonic of a transparent grating, which is excited by a laser beam incident perpendicularly to the grating surface.

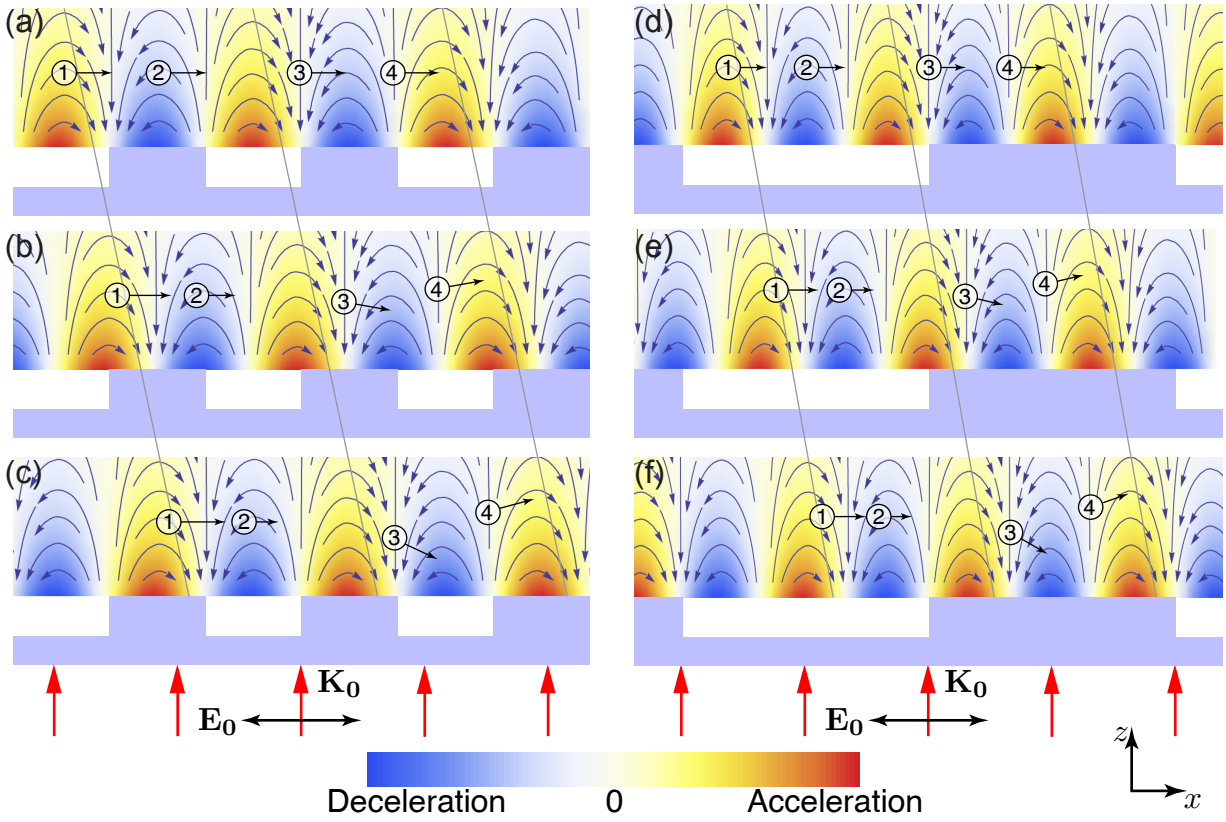

Figure 2.2: (a-c), Three subsequent conceptual pictures of four electrons (circles) passing the transparent grating (light blue structure). A laser beam with linear polarization in the plane of projection is incident from below. The time step between each picture is a quarter optical period. Only the electric field of the first spatial harmonic is shown. It is synchronous with the electrons and falls off exponentially in the z-direction (color-coded). Depending on the position of the electron inside the laser field the force acting on the electron can be accelerating (1), decelerating (2) or deflecting (3,4). Note that the geometry implies that the fields are transverse magnetic (TM), so the only field components are E_x, E_z and B_y ($\varphi = \psi = \theta = 0$ in Figure 2.1). (d-f), Illustration of four electrons interacting with the third spatial harmonic of the grating, which oscillates three times per grating period.

The electromagnetic field of the synchronous mode can be calculated using

$$\mathbf{k} = k_0 \begin{pmatrix} 1/\widetilde{\beta} \\ 0 \\ i/(\widetilde{\beta}\widetilde{\gamma}) \end{pmatrix}, \tag{2.9}$$

$$\nabla \times \mathbf{E} = -\frac{\partial \mathbf{B}}{\partial t} \qquad \text{and} \qquad \nabla \times \mathbf{B} = \frac{1}{c^2}\frac{\partial \mathbf{E}}{\partial t}. \tag{2.10}$$

We obtain

$$\mathbf{E} = \begin{pmatrix} icB_y/(\widetilde{\beta}\widetilde{\gamma}) \\ E_y \\ -cB_y/\widetilde{\beta} \end{pmatrix}, \qquad \mathbf{B} = \begin{pmatrix} -iE_y/(\widetilde{\beta}c\widetilde{\gamma}) \\ B_y \\ E_y/(\widetilde{\beta}c) \end{pmatrix}, \tag{2.11}$$

where we have omitted the position and time dependence of the fields. There are two independent solutions corresponding to the transverse electric (TE) and the transverse magnetic (TM) modes. The amplitudes E_y and B_y of these modes, respectively, have to be calculated for each geometry individually.

From the fields we can compute the Lorentz force

$$\begin{aligned} \mathbf{F} &= q(\mathbf{E} + \mathbf{v} \times \mathbf{B}) \\ &= q \begin{pmatrix} icB_y/(\widetilde{\beta}\widetilde{\gamma}) + \tan\varphi E_y \\ 0 \\ -cB_y(1-\widetilde{\beta}^2)/\widetilde{\beta} + i\tan\varphi E_y/\widetilde{\gamma} \end{pmatrix}. \end{aligned} \tag{2.12}$$

Projecting into the particles coordinate system $\{x', y', z'\}$ yields

$$\mathbf{F}_{\mathbf{r}'} = q \begin{pmatrix} icB_y/(\beta\widetilde{\gamma}) + E_y \sin\varphi \\ -icB_y \tan\varphi/(\beta\widetilde{\gamma}) - E_y \sin\varphi \tan\varphi \\ -cB_y/(\widetilde{\beta}\widetilde{\gamma}^2) + iE_y \tan\varphi/\widetilde{\gamma} \end{pmatrix}. \tag{2.13}$$

It is important to note that the longitudinal force $F_{x'}$ is always accompanied by a transverse force component $F_{z'}$ that causes deflection of the electrons towards or away from the grating. However, the accelerating and deflecting forces are out of phase. Stable acceleration takes place when electrons are accelerated and at the same time temporally bunched (i.e., focused in time). In this case, the geometry of the accelerating fields leads to a defocusing of the electron bunch, which can be readily explained by Earnshaw's theorem

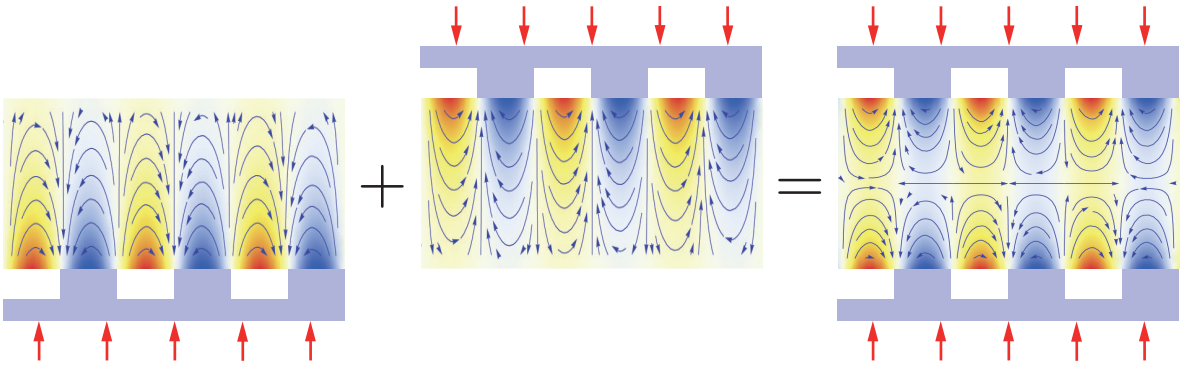

Figure 2.3: Schematic illustration of the advantage of double grating structures. The superposition of the exponentially decaying field pattern of two single gratings leads to the symmetric field pattern of the double grating. The color scale, which represents the electric field strength of the first spatial harmonic, differs for the single and double grating.

$\nabla \cdot \mathbf{E} = 0$ [127]: Longitudinal (i.e., temporal) focusing leads to transverse defocusing. Confinement of the beam can be achieved, e.g., by alternating phase focusing. Here the consecutive alternation of accelerating and focusing elements, in which the electron bunch is injected at different positions relative to the synchronous field (see Figure 2.2), leads to stable acceleration [42,128,129]. Alternatively, Naranjo *et al.* have proposed a biharmonic structure which exploits a synchronously accelerating mode while focusing the electron bunch through ponderomotive interaction with an asynchronous mode [76].

A drawback of exploiting single gratings for particle acceleration is the skew acceleration pattern, i.e., the exponential dependence of the accelerating force as a function of the electron's distance from the surface. This can lead to a distortion of the electron beam passing the grating. However, by exciting phase stable fields on two close, parallel gratings, the setup can be arranged in a manner that the deflecting forces cancel each other and create a force pattern that is symmetric around the axis of the vacuum channel [80, 130]. A sketch of the basic idea is depicted in Figure 2.3. The distance between the two surfaces has to be on the order of δ (Equation 2.8) in order to efficiently accelerate electrons inside such a double grating structure.

It can also be seen that a single grating cannot be used to accelerate particles close to the speed of light ($\beta \sim 1$) unless $\varphi \neq 0$ [62]. However, the double grating structure exhibits a speed-of-light mode, which can be used to continuously accelerate $\beta \sim 1$ particles. This can be explained as follows. For $k_{\parallel} = k_0$ the synchronicity condition implies that $d^2\mathcal{A}/dz^2 = 0$ and therefore $\mathcal{A}(\mathbf{r}) = \mathcal{A}(x, y)(1+\kappa z)$. In the case of a single surface this mode cannot exist, because a constant or linearly increasing electric field extending to infinity is unphysical. However, in the presence of a second boundary there is a linear solution, which is associated with a constant longitudinal (accelerating) force component [130].

The TE mode ($B_y = 0$) cannot be used to accelerate particles because $F_{z'} = 0$ in the case of $\varphi = 0$. In the following we will therefore restrict our discussion to a TM mode

($E_y = 0$) with $\varphi = \psi = \theta = 0$, as it is shown in Figure 2.2. Hence,

$$\mathbf{F_r} = q \begin{pmatrix} icB_y/(\beta\gamma) \\ 0 \\ -cB_y/(\beta\gamma^2) \end{pmatrix}. \tag{2.14}$$

2.2 Estimate for the dephasing length

In order to satisfy the synchronicity condition for an accelerating non-relativistic particle, the phase velocity of the accelerating mode has to change continuously to account for the velocity change of the particle. In case of a constant phase velocity of the accelerating mode the relative position of the particle with respect to the mode changes as the particle gains speed. This has been schematically depicted in Figure 2.2. The electron that experiences the largest acceleration (encircled number one) slips ahead of the synchronous mode. We call this effect dephasing. We now derive an estimate on the maximum acceleration distance over which acceleration can take place if the mode *remains* at the same phase velocity. We can also ask: when does the particle become accelerated so much that it starts experiencing deceleration upon dephasing?

The only assumption is that $\Delta\beta/\beta \ll 1$ during the acceleration. This is true for relativistic $\beta \sim 1$ particles, as the change in velocity in the laboratory frame is practically zero. In the non-relativistic case the particle's velocity gain $\Delta\beta$ is limited due to dephasing. $\Delta\beta$ is much smaller than the initial velocity β if the particle's energy gain ΔE over one wavelength λ of the driving field is well below the particle's rest energy m_0c^2, i.e., $G \ll m_0c^2/\lambda$. For larger acceleration gradients $G > m_0c^2/\lambda$, the particles can be accelerated from rest to relativistic energies within one cycle of a speed-of-light mode, which then travels synchronously with the particles.

Dephasing effects will play an important role in optical accelerators ($\lambda \sim 1\,\mu$m) for non-relativistic electrons ($m_0c^2 = 511\,$keV), because an acceleration gradient larger than 500 GeV/m would be required to boost the electrons to relativistic energies within one cycle of the laser field. For conventional RF linacs ($\lambda \sim 10\,$cm) dephasing of electrons can often be neglected, because typical gradients are larger than 5 MeV/m. However, dephasing or longitudinal phase slippage effects are well-known in proton and ion linacs, where much heavier particles are accelerated [42].

The accelerating force acting on an electron passing the grating surface at a distance z_0 has been derived in the previous section (Equation 2.14) and can be written as

$$\begin{aligned} F_x(x, z_0, t) &= \frac{ecB_y}{\beta\gamma} e^{-k_0 z_0/(\beta\gamma)} \mathrm{Re}\left[e^{i(k_0 x/\beta_0 - \omega t + \phi_0)}\right] \\ &= G(z_0) \mathrm{Re}\left[e^{i(k_0 x/\beta_0 - \omega t + \phi_0)}\right], \end{aligned} \tag{2.15}$$

with the acceleration gradient

$$G(z_0) := \frac{ec\,|B_y|}{\beta\gamma} e^{-k_0 z_0/(\beta\gamma)}. \tag{2.16}$$

In the electron's co-moving frame, i.e., $\omega t = \omega x/(\beta(x)c) = k_0 x/\beta(x)$, with the instantaneous velocity $\beta(x) = \beta_0 + \Delta\beta(x)$, we derive the instantaneous force

$$F_x(x, z_0) = G(z_0) \cos\left(\frac{k_0 x}{\beta_0^2} \int_0^x \beta'(u)du + \phi_0\right), \tag{2.17}$$

using

$$\begin{aligned} \frac{\beta_0}{\beta(x)} &= \frac{\beta_0}{\beta_0 + \Delta\beta(x)} \\ &= \frac{1}{1 + \frac{\int_0^x \beta'(u)du}{\beta_0}} \approx 1 - \frac{\int_0^x \beta'(u)du}{\beta_0}. \end{aligned} \tag{2.18}$$

The validity of Equation 2.17 can be verified with the simulations presented in Figure 3.3 on page 33. The first term in the cosine is the dephasing term, which we estimate here. It is useful to recapitulate the following identities:

$$E_{\text{kin}} = m_0 c^2(\gamma - 1), \tag{2.19}$$

$$\beta = \sqrt{1 - \frac{1}{\gamma^2}}. \tag{2.20}$$

With $d\gamma/dx = 1/(m_0c^2) \cdot dE_{\text{kin}}/dx$, we derive

$$\frac{d\beta}{dx} = \frac{d}{dx}\sqrt{1 - \frac{1}{\gamma^2}} = \frac{1}{\gamma^3\sqrt{1 - \frac{1}{\gamma^2}}}\frac{d\gamma}{dx} = \frac{1}{m_0c^2\beta\gamma^3}\frac{dE_{\text{kin}}}{dx}. \tag{2.21}$$

We only consider the particle motion in one dimension and neglect deflecting forces. Therefore we can write $dE_{\text{kin}}/dx = F_x$. Hence, the dephasing angle $\Delta\phi$ can be estimated with

$$\begin{aligned} \Delta\phi(x) &:= \frac{k_0 x}{\beta_0^2} \int_0^x \beta'(u)du \\ &= \frac{k_0 x}{m_0 c^2 \beta_0^2} \int_0^x \frac{F_x(u, z_0)}{\beta(u)\gamma^3(u)}du < \frac{k_0 x^2 G_{\max}(z_0)}{m_0 c^2 \beta_0^3 \gamma_0^3}, \end{aligned} \tag{2.22}$$

because for an *accelerating* particle $F_x < G_{\max}$, the maximum acceleration gradient (Equation 2.15), $\beta(u) > \beta_0$, the initial velocity, and $\gamma(u) > \gamma_0 = (1 - \beta_0^2)^{-1/2}$. Using $\beta^2\gamma^2 = \gamma^2 - 1 = (\gamma - 1)(\gamma + 1)$ and demanding that the dephasing angle has to be smaller than $\pi/2$ for efficient acceleration, we obtain an estimate for the maximum length, over

which a particle can be accelerated until acceleration ceases. This *dephasing length* is given by

$$x_{\mathrm{deph}} = \left(\frac{\beta_0 \lambda E_{\mathrm{kin}} \left(\frac{E_{\mathrm{kin}}}{m_0 c^2} + 1 \right) \left(\frac{E_{\mathrm{kin}}}{m_0 c^2} + 2 \right)}{4 G_{\mathrm{max}}(z_0)} \right)^{1/2} . \tag{2.23}$$

It depends strongly on the initial kinetic energy E_{kin}. This approximation shows the intuitively correct behavior: relativistic particles ($E_{\mathrm{kin}} > m_0 c^2$) dephase after a longer distance, and larger acceleration gradients cause stronger dephasing. In Section 3.2 we calculate the dephasing lengths for non-relativistic and relativistic electrons inside a double grating structure.

Chapter 3

Simulation of grating-based particle acceleration

In this chapter we describe the simulations we have performed to calculate the electron acceleration in close vicinity of dielectric gratings. The first two sections present general simulation results for single and double grating structures, which exploit the first spatial harmonic for synchronous particle acceleration. In the last section we show the results of the simulated electron acceleration with the third spatial harmonic of the fused silica grating that has been used for the experiment presented in Chapter 4. We also discuss the calculation of the accelerated fraction of electrons, based on the parameters of the initial electron beam. The content of this chapter follows [126].

3.1 Simulation of acceleration at a single dielectric grating

There is a variety of methods to simulate the propagation of electromagnetic waves through media such as the finite-difference time-domain (FDTD) method [131], the finite element method (FEM) [132,133], the finite integration technique (FIT) [134] or the pseudospectral time domain (PSTD) method [135]. We chose yet another method, namely an eigenmode expansion method for our simulations of a plane wave propagating through a dielectric grating [136]. It is used to compute the amplitudes of the spatial harmonics at a grating with an infinitely periodic, rectangular profile. The method allows the direct computation of the amplitudes E_y and B_y of the TE and TM mode (Equation 2.11). We have verified this method by comparison with published results [136, 137].

3.1.1 Acceleration efficiency of single fused silica gratings

We focus on the TM mode again, as shown in Figure 2.2, because of the longitudinal accelerating electric field component (Equation 2.14). In our simulation we choose the exciting laser wavelength λ and determine the grating period such that the n-th spatial

harmonic is synchronous with electrons with velocity βc. This implies a grating period of $\lambda_\mathrm{p} = n\beta\lambda$. We directly simulate the magnetic field amplitude $B_y^{(n)}$ of the n-th harmonic. With the definition of the acceleration gradient $G(z_0)$ at a fixed distance z_0 in Equation 2.16 on page 24 and the peak electric field E_p of the exciting laser, we obtain the acceleration efficiency

$$\epsilon_\mathrm{acc} := \frac{G(z_0)}{eE_\mathrm{p}} = \frac{c\left|B_y^{(n)}\right|}{E_\mathrm{p}} \cdot \frac{e^{-k_0 z_0/(\beta\gamma)}}{\beta\gamma}. \tag{3.1}$$

Finally, we optimize the grating depth and aspect ratio to maximize $B_y^{(n)}$. The first term in Equation 3.1 represents the excitation efficiency of the spatial harmonic

$$\epsilon_\mathrm{exc} := cB_y^{(n)}/E_\mathrm{p}, \tag{3.2}$$

which is directly related to the magnetic field amplitude B_y of the TM mode at the grating surface (Equation 2.11).

In Figure 3.1 (a) we show ϵ_exc as a function of the electron velocity β, directly related to the grating period via $\lambda_\mathrm{p}(\beta) = n\beta\lambda$, for the first, second and third spatial harmonic of a single fused silica grating. It can be seen that ϵ_exc increases as $\beta \to 1$, which is due to wave matching between the wave vector of the incident laser k_0 and of the synchronous spatial harmonic $k = k_0/\beta$.

In Figure 3.1 (b) we show the acceleration efficiency ϵ_acc as a function of the electron velocity β exploiting the first, second and third spatial harmonic 100 nm away from a fused silica grating. For highly relativistic velocities ($\beta \sim 1$) ϵ_acc drops to zero with $1/\gamma = \sqrt{1-\beta^2}$. This is expected for the particle acceleration at a single grating with grating grooves perpendicular to the particle's trajectory [62]. However, ϵ_acc can be on the order of one for double grating structures that support a speed-of-light eigenmode [68], as discussed in Section 2.1. We show a linear fit of ϵ_acc, which allows us to estimate the length of a non-relativistic DLA in Table 5.2 on page 74.

3.1.2 Particle tracking simulation in the vicinity of single fused silica gratings

To gain further insight we perform a particle tracking simulation in the field above the grating. The field consists of a Fourier series of all spatial harmonics. Thereby we study deflecting forces and dephasing effects. In our simulation we use the MATLAB® ode45 routine to numerically integrate the Lorentz force.

We track a single electron passing the grating surface with a velocity βc. The exciting laser pulse is incident perpendicularly to the electron's trajectory and exhibits a cycle-averaged optical electric field

$$\tilde{E}_\mathrm{p} = E_\mathrm{p} e^{-(x/w_\mathrm{l})^2 - 2\ln(2)(t/\tau_\mathrm{p})^2}, \tag{3.3}$$

with the $1/e$ focal waist radius w_l and the laser pulse duration τ_p (full width at half maximum of the intensity envelope). Hence, in its co-moving frame the electron experiences

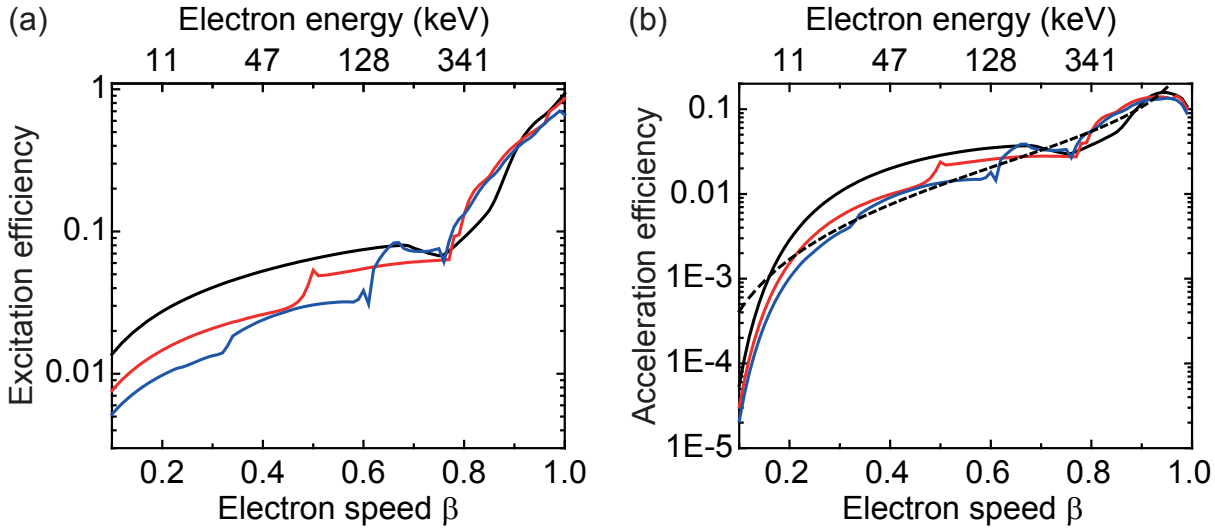

Figure 3.1: (a), Excitation efficiency $\epsilon_{\mathrm{exc}} = cB_y^{(n)}/E_{\mathrm{p}}$ of the n-th spatial harmonic (first: black, second: red, third: blue) as a function of the electron velocity β (bottom axis) and of the electron energy E_{kin} (top axis). The grating period is $\lambda_{\mathrm{p}}(\beta) = n\beta\lambda$. The exciting laser wavelength is $\lambda = 800\,\mathrm{nm}$. The aspect ratio (i.e., the ratio of the trench width to the grating period) and grating depth have been optimized to maximize $cB_y^{(n)}$ for each β. During the optimization we first varied the aspect ratio between 0 and 1 for a fixed grating depth of 250 nm. Afterwards we varied the grating depth between 0 and λ_{p} for the optimum aspect ratio. (b), The acceleration efficiency $\epsilon_{\mathrm{acc}} = G(z_0)/(eE_{\mathrm{p}})$ at a distance of $z_0 = 100\,\mathrm{nm}$ from the grating surface as a function of β (bottom axis) and E_{kin} (top axis), exploiting the first (black), second (red) and third (blue) spatial harmonic. For highly relativistic velocities ($\beta \sim 1$) ϵ_{acc} drops to zero with $\sqrt{1-\beta^2}$ for a single grating (Equation 3.1). The black dashed line shows the linear fit of $G/(eE_{\mathrm{p}}) = E_{\mathrm{kin}} \cdot 1.61 \cdot 10^{-7}\,\mathrm{eV}^{-1}$ up to an energy of 1 MeV for the first spatial harmonic, which we use to estimate the length of an optical linac in Table 5.2 on page 74. The kinks in the efficiency in (a) and (b), e.g., for the second spatial harmonic at $\beta \sim 1/2$ and for the third spatial harmonic at $\beta \sim 2/3$ occur when the next lower order spatial harmonic starts to propagate, i.e., $k_0 > k^{(n-1)} = (n-1)k_{\mathrm{p}} = (n-1)k_0/(n\beta)$ and hence $\beta > (n-1)/n$.

the instantaneous electric field

$$\tilde{E}_\mathrm{p} = E_\mathrm{p} e^{-(x/w_\mathrm{int})^2}, \tag{3.4}$$

with the characteristic interaction distance

$$w_\mathrm{int} = \left(\frac{1}{w_\mathrm{l}^2} + \frac{2\ln(2)}{(\beta c \tau_\mathrm{p})^2} \right)^{-1/2}. \tag{3.5}$$

In Figure 3.2 we show the results of the particle tracking for single non-relativistic (30 keV) and relativistic (1 MeV) electrons interacting with the first spatial harmonic close to a fused silica grating. We simulate the energy gain, the deflection, as well as the final angle of the electron trajectory with respect to the grating surface. The acceleration shows the expected behavior: a phase shift between the accelerating and deflecting force (Equation 2.14) and a larger decay constant δ (Equation 2.8) for relativistic electrons (Figure 3.2 (g-i)) compared to non-relativistic electrons (Figure 3.2 (a-f)). The maximum acceleration gradient $G_\mathrm{max}(z_0)$ at a distance z_0 can be directly inferred from the maximum energy gain $\Delta E(z_0)$ via

$$G_\mathrm{max}(z_0) = \frac{\Delta E(z_0)}{\sqrt{\pi} w_\mathrm{int}}. \tag{3.6}$$

For example, in Figure 3.2 (a) we obtain $\Delta E = 100\,\mathrm{eV}$ at $z_0 = 100\,\mathrm{nm}$, corresponding to $G_\mathrm{max} = 13\,\mathrm{MeV/m}$ for $w_\mathrm{int} = 4.3\,\mu\mathrm{m}$. This is in perfect agreement with a peak electric field of 1 GV/m and an acceleration efficiency $\epsilon_\mathrm{acc} = 1.3 \cdot 10^{-2}$ for $\beta = 0.33$, shown in Figure 3.1 (b). In Figure 3.2 (g) we calculate $\Delta E = 14\,\mathrm{keV}$ at $z_0 = 100\,\mathrm{nm}$ and therefore $G_\mathrm{max} = 1.6\,\mathrm{GeV/m}$ for $w_\mathrm{int} = 4.9\,\mu\mathrm{m}$. This also agrees with $E_\mathrm{p} = 10\,\mathrm{GV/m}$ and $\epsilon_\mathrm{acc} = 0.16$ for $\beta = 0.94$ (Figure 3.1 (b)).

The strong deflection of the non-relativistic electrons in Figure 3.2 (d-f) is indicated by the white areas that represent initial electron parameters for which the electron becomes deflected into the grating during the simulation. It suggests to choose laser peak electric fields well below 10 GV/m for the acceleration of non-relativistic electrons in order to prevent beam loss as well as surface charging of the dielectric material that can cause

Figure 3.2 *(following page)*: Particle tracking results of a single electron interacting with laser pulses in close proximity of a fused silica grating. The laser parameters are: wavelength $\lambda = 800\,\mathrm{nm}$, focal waist radius $w_\mathrm{l} = 5\,\mu\mathrm{m}$, pulse duration $\tau_\mathrm{p} = 100\,\mathrm{fs}$, laser peak electric field $E_\mathrm{p} = 1\,\mathrm{GV/m}$ (a-c) and $E_\mathrm{p} = 10\,\mathrm{GV/m}$ (d-i). The initial electron energies are $E_\mathrm{kin} = 29\,\mathrm{keV}$ ($\beta = 0.33$) (a-f) and $E_\mathrm{kin} = 957\,\mathrm{keV}$ ($\beta = 0.94$) (g-i). The first spatial harmonic interacts synchronously with the electrons, hence $\lambda_\mathrm{p} = 260\,\mathrm{nm}$ (a-f) and $\lambda_\mathrm{p} = 750\,\mathrm{nm}$ (g-i). Color-coded plots show the energy gain ΔE_kin (a,d,g), the deflection Δz (b,e,h) and the final angle β_z/β_x (c,f,i) as a function of the initial distance z_0 from the grating surface before the interaction with the laser, and of the relative start phase between the electron and the laser field. For the white areas the electron was deflected into the grating during the simulation. The characteristic interaction distance is $w_\mathrm{int} = 4.3\,\mu\mathrm{m}$ (a-f) and $w_\mathrm{int} = 4.9\,\mu\mathrm{m}$ (g-i). See text for more details.

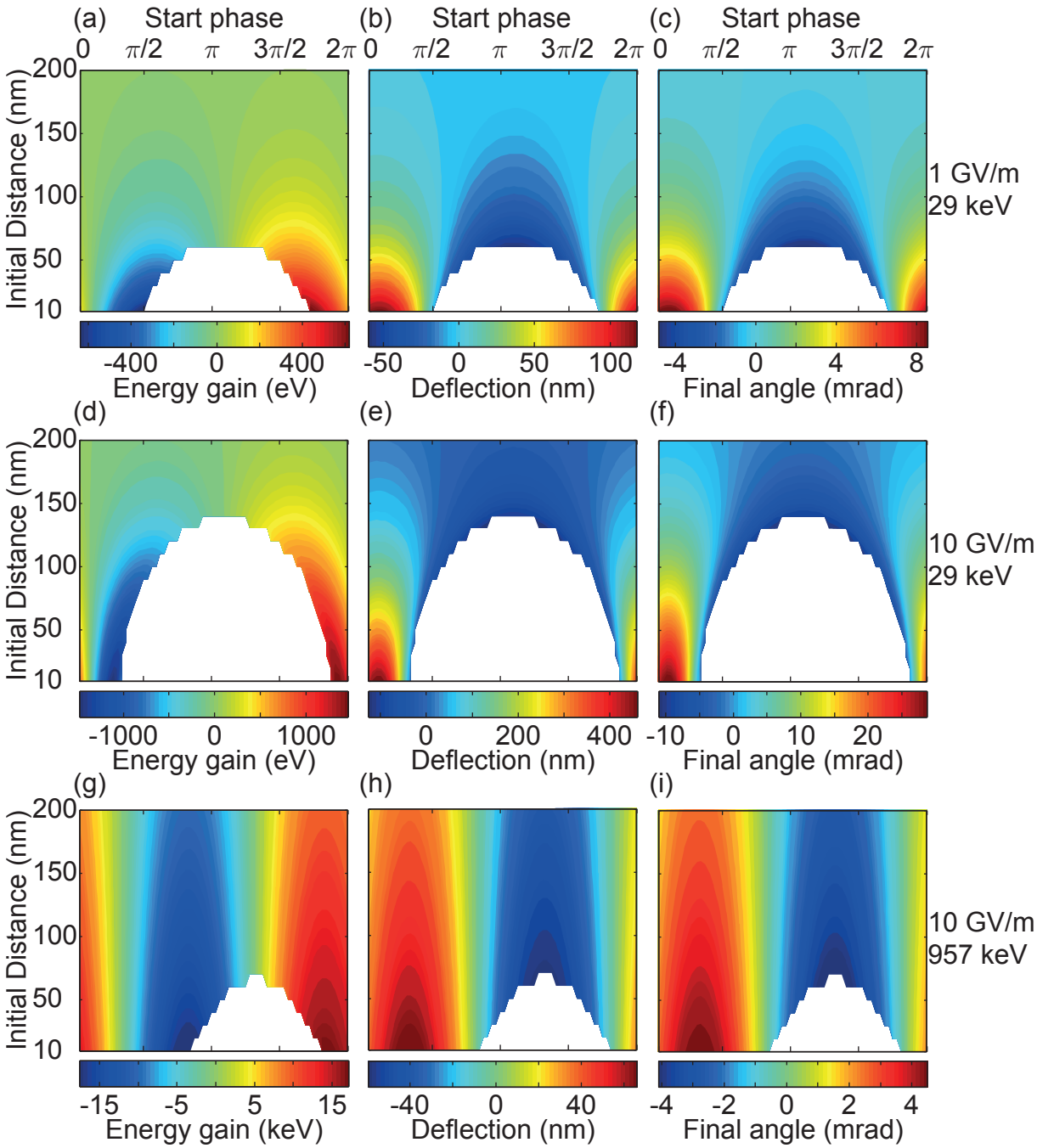
(a) Start phase
(b) Start phase
(c) Start phase
0 π/2 π 3π/2 2π
Initial Distance (nm)
200
150
100
50
10
-400 0 400
Energy gain (eV)
-50 0 50 100
Deflection (nm)
-4 0 4 8
Final angle (mrad)
1 GV/m
29 keV
(d)
(e)
(f)
-1000 0 1000
Energy gain (eV)
0 200 400
Deflection (nm)
-10 0 10 20
Final angle (mrad)
10 GV/m
29 keV
(g)
(h)
(i)
-15 -5 5 15
Energy gain (keV)
-40 0 40
Deflection (nm)
-4 -2 0 2 4
Final angle (mrad)
10 GV/m
957 keV

further deflection. Of course this would not be necessary if a microbunched electron beam, phase-stabilized to the laser field, with a microbunch duration much smaller than the optical cycle was used and if the electrons only occupied start phases for which deflection is negligible.

The simulation of the final angle β_z/β_x of the electron trajectory with respect to the grating surface, shown in Figure 3.2 (c,f,i), confirms that relativistic electrons are less affected by a deflecting force compared to non-relativistic electrons. However, for the moderately relativistic energy of 1 MeV the electrons can be deflected by a few mrad over an interaction distance of only 5 μm. This cannot be neglected and has to be taken into account for the design of future DLAs. Note that in our simulation a larger start phase corresponds to a later start time. Hence, temporal bunching (i.e., focusing in time) takes place when electrons with a smaller start phase (earlier start time) become less accelerated than electrons with a larger start phase (later start time).

The maximum laser peak electric field, which we use for the simulation shown in Figure 3.2, is $E_\mathrm{p} = 10\,\mathrm{GV/m}$. It corresponds to a peak fluence $F_\mathrm{p} = 1.42\,\mathrm{J/cm^2}$, close to the damage threshold reported in [138], for the laser parameters: wavelength $\lambda = 800\,\mathrm{nm}$, focal waist radius $w_\mathrm{l} = 5\,\mu\mathrm{m}$ and pulse duration $\tau_\mathrm{p} = 100\,\mathrm{fs}$.

3.1.3 Simulation of dephasing effects

In Figure 3.3 we show the instantaneous kinetic energy $\tilde{E}_\mathrm{kin}(x)$, the instantaneous acceleration gradient $\tilde{G}(x)$, the instantaneous laser electric field $\tilde{E}_\mathrm{p}(x)$ and the dephasing angle $\Delta\phi(x)$ as a function of the longitudinal position of the electron. Note that the instantaneous acceleration gradient $\tilde{G}(x)$ is identical to the accelerating force $F_x(x)$ used in the derivation of the dephasing length in Equation 2.17 on page 24. Hence, here we can compare the particle tracking results with the theoretical calculation of Section 2.2.

First, we differentiate the kinetic energy and obtain

$$\tilde{G}(x) = \frac{d\tilde{E}_\mathrm{kin}(x)}{dx}. \tag{3.7}$$

We then use the simulated instantaneous laser electric field $\tilde{E}_\mathrm{p}(x)$ and dephasing angle $\Delta\phi(x)$ as input parameters, and fit $\tilde{G}(x)$ according to Equation 2.17 with

$$\tilde{G}(x, z_0) = \epsilon\tilde{E}_\mathrm{p}(x)e^{-z_0/\delta}\cos\left(\Delta\phi(x) + \phi_0\right), \tag{3.8}$$

with the free fit parameters ϵ and ϕ_0. The agreement between the fit and the directly calculated $\tilde{G}(x)$ in Figure 3.3 (a) and (c) confirms Equation 2.17.

For negligible dephasing $(\Delta\phi+\phi_0) \sim 0$ the fit parameter ϵ is identical to the acceleration efficiency ϵ_acc defined in Equation 3.1 on page 28, as $\delta = \beta\gamma/k_0$ (Equation 2.8). This explains why we obtain $\epsilon = 1.3 \cdot 10^{-2}$ in Figure 3.3 (a,b), which equals ϵ_acc for the electron speed $\beta = 0.33$, shown in Figure 3.1 (b).

In Figure 3.3 (c,d) the dephasing of the electron is severe and causes deceleration after initial acceleration. The width of the instantaneous laser electric field $\tilde{E}_\mathrm{p}(x)$ equals the

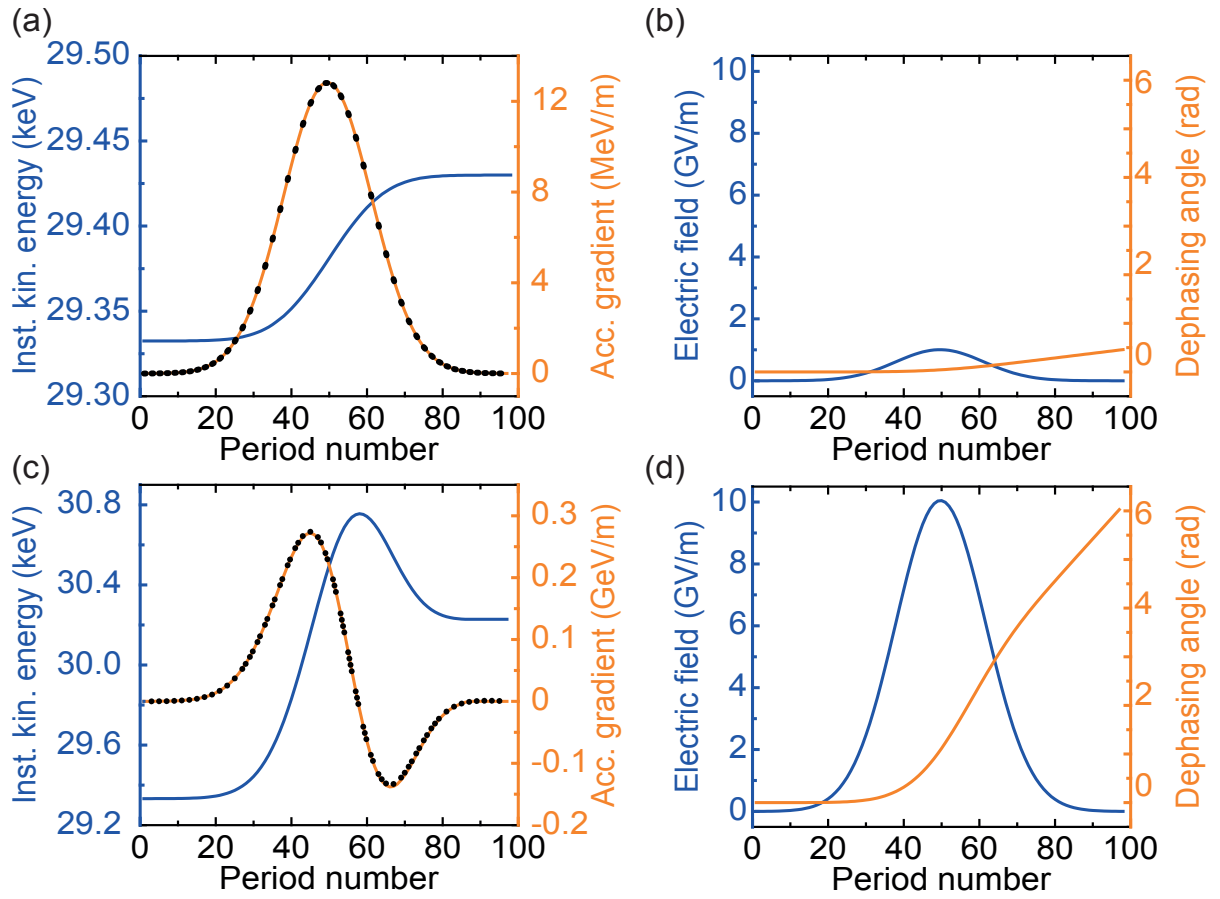

Figure 3.3: Effect of dephasing. We show the instantaneous parameters of a single electron interacting with laser pulses in close proximity of a fused silica grating as a function of the number of grating periods passed (x-coordinate). We include the instantaneous kinetic energy $\tilde{E}_{\mathrm{kin}}(x)$ ((a,c), blue curve), acceleration gradient $\tilde{G}(x)$ ((a,c), orange curve, black dots), laser electric field $\tilde{E}_{\mathrm{p}}(x)$ ((b,d), blue curve) and dephasing angle $\Delta\phi(x)$ ((b,d), orange curve). The acceleration gradient has been directly derived from $\tilde{E}_{\mathrm{kin}}(x)$ via $\tilde{G}(x) = \mathrm{d}\tilde{E}_{\mathrm{kin}}(x)/\mathrm{d}x$ (orange curve). It has also been fitted according to Equation 2.17 (black dots), with the input parameters $\tilde{E}_{\mathrm{p}}(x)$ and $\Delta\phi(x)$. (a,b), Identical simulation parameters as used in Figure 3.2 (a-c) for a start phase of $1.6\,\pi$ and an initial distance $z_0 = 100\,\mathrm{nm}$. For those parameters dephasing and deflection can be neglected, as $\Delta\phi < \pi/2$. (c,d), Identical simulation parameters as used in Figure 3.2 (d-f) for a start phase of $1.8\,\pi$ and an initial distance $z_0 = 50\,\mathrm{nm}$. Here, dephasing is severe: after initial acceleration over ∼60 grating periods, the electron is decelerated. See text for more details.

characteristic interaction distance $w_{\mathrm{int}} = 4.3\,\mu$m. Note that the dephasing angle $\Delta\phi(x)$ continues to increase after the interaction of the electron with the laser field. This is because after the acceleration process the electron's increased velocity does not match the phase speed of the accelerating mode. However, the value of the dephasing angle after the interaction has no importance for the maximum acceleration gradient.

3.2 Simulation of acceleration inside double grating structures

3.2.1 Geometry and field profile of double grating structures

We call the geometry with two gratings facing each other double grating structure. It exhibits the advantage of enabling a symmetric acceleration pattern because the synchronous mode of a double grating structure does not generally decay exponentially with increasing distance from the grating surface, as it is the case for a single grating. Instead the field pattern at a distance z is given by

$$B_y = (C_{\mathrm{s}} \sinh(k_z z) + C_{\mathrm{c}} \cosh(k_z z)) \cos(k_x x - \omega t), \tag{3.9}$$

with $k_x = k_0/\beta$ and $k_z = k_0/(\beta\gamma)$ (Equation 2.9) [80, 130]. Double grating structures also support a speed-of-light mode which can be used to synchronously accelerate relativistic particles [130], as mentioned in Section 2.1. Following the same discussion as in Section 2.1, we obtain for the Lorentz force

$$\mathbf{F_r} = qc \begin{pmatrix} \frac{1}{\beta\gamma} \left(C_{\mathrm{s}} \cosh(k_z z) + C_{\mathrm{c}} \sinh(k_z z)\right) \sin(k_x x - \omega t) \\ 0 \\ -\frac{1}{\beta\gamma^2} \left(C_{\mathrm{s}} \sinh(k_z z) + C_{\mathrm{c}} \cosh(k_z z)\right) \cos(k_x x - \omega t) \end{pmatrix}. \tag{3.10}$$

In Figure 3.4 (a) we show the electric field profile of a double grating structure, for which $C_{\mathrm{s}} = \text{max.}$ and $C_{\mathrm{c}} = 0$. As for the single grating, regions of acceleration and deceleration exist. However, around the axis of the structure the accelerating force component is rather uniform, as can be seen from $dF_x/dz \propto d\cosh(k_z z)/dz|_{z=0} = 0$. Moreover, the transverse force component can focus electrons towards the axis, because $F_z(z < 0) \propto -\sinh(k_z z)|_{z<0} > 0$ and $F_z(z > 0) \propto -\sinh(k_z z)|_{z>0} < 0$. The longitudinal and transverse forces are out of phase. Therefore an electron passing through the structure at a relative position to the field where it is maximally accelerated does not experience any focusing force, and vice versa. This is analogous to the acceleration at single gratings and can be explained with Earnshaw's theorem [127], as discussed in Section 2.1.

In Figure 3.4 (b) and (c) we show two different field patterns of the double grating structures where $C_{\mathrm{c}} \neq 0$. It can be seen that both profiles are not suited for useful particle acceleration. In Figure 3.4 (b), where $C_{\mathrm{c}} = \text{max.}$ and $C_{\mathrm{s}} = 0$, the accelerating

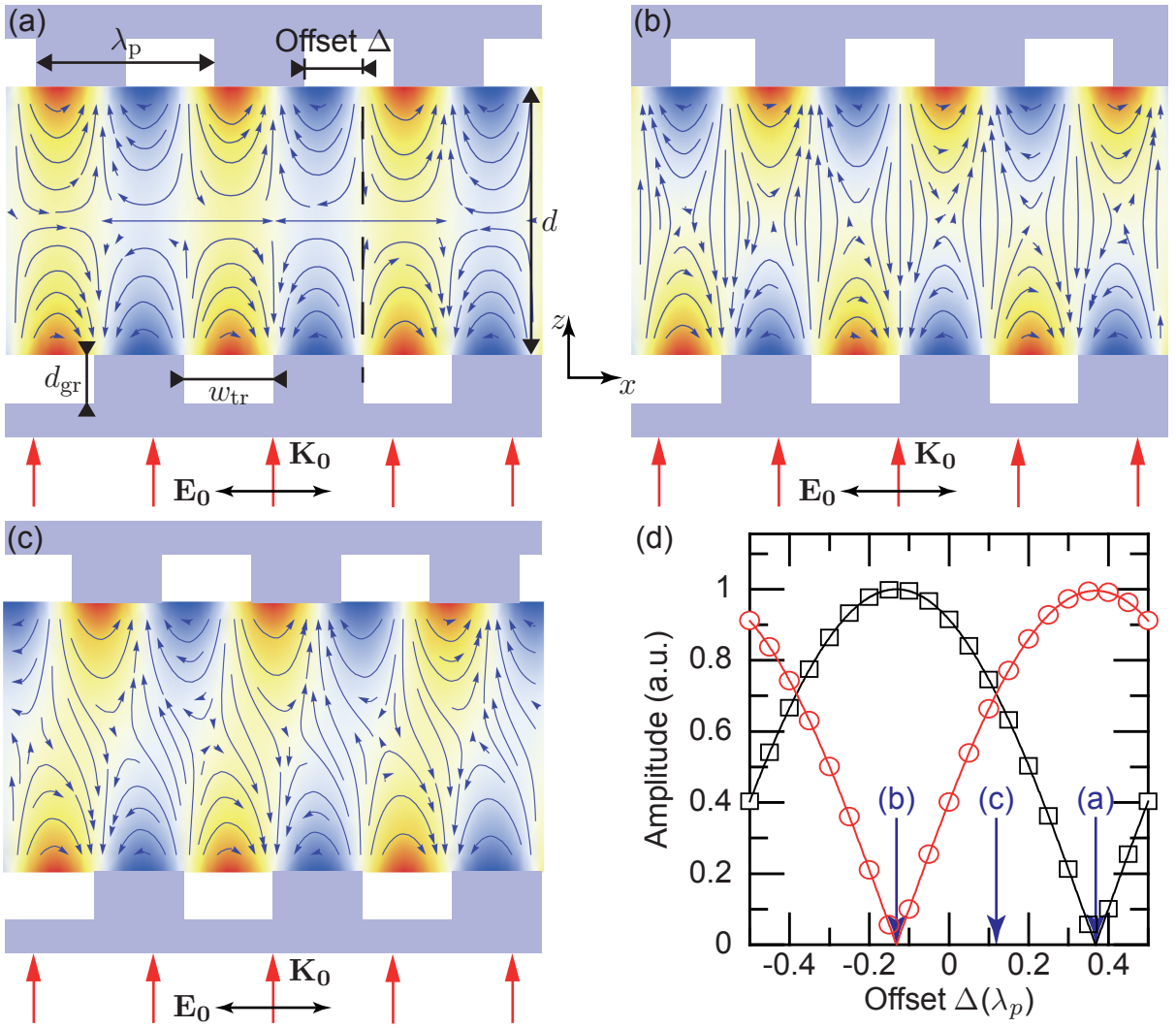

Figure 3.4: (a-c), Conceptual pictures of the dielectric double grating structure (light blue), which is illuminated by a single laser from below. The separation between the two grating surfaces is d and the upper grating has a longitudinal offset Δ compared to the lower one. The accelerating electric field profile of the first spatial harmonic (color-coded, red: acceleration, blue: deceleration) as a function of z can be $\cosh(k_z z)$ (a), $\sinh(k_z z)$ (b) or a superposition thereof (c). The individual offsets Δ for the geometries in (a-c) are indicated in (d). Not to scale. (d), Simulated amplitudes C_c (black squares) and C_s (red circles) as a function of the offset Δ. The solid lines are fitted curves with the fit function $|\sin(\pi\Delta)|$. The grating parameters are: grating period $\lambda_p = 260\,\text{nm}$, grating depth $d_{gr} = 190\,\text{nm}$, trench width $w_{tr} = 0.47\,\lambda_p$, optimized for a maximum excitation efficiency of the single grating, and grating distance $d = 200\,\text{nm}$ (see Figure 3.5(a)). The laser wavelength is $\lambda = 800\,\text{nm}$.

force component F_x vanishes on axis, as $\sinh(k_z z)|_{z=0} = 0$. Figure 3.4 (c) corresponds to a superposition of the cosh- and sinh-profile, which would lead to a skew acceleration pattern and to simultaneous deflection of electrons, resulting in a distortion of the beam profile.

To obtain the field distributions shown in Figure 3.4 (a-c) we again use the eigenmode expansion method [136]. We calculate the amplitudes of the spatial harmonics excited by a single laser source. The speed-of-light mode, which only occurs for $\lambda_\mathrm{p} = \lambda$ is not included in our simulations because the method by Pai and Awada [136], which was developed primarily for single gratings, does not include this particular mode. However, Plettner *et al.* have proposed adjustments that have to be made to the original method in order to include the speed-of-light mode [130].

The different superpositions of the cosh- and sinh-profile in Figure 3.4 (a-c) were found by changing the relative offset Δ between the upper and the lower grating. This longitudinal shift between the grating grooves of the upper as compared to the lower grating is related to a time delay between the excitation of the two single gratings. Hence by changing the offset the relative phase between the exponentially decaying fields at both grating surfaces is shifted. This shift can be inferred from Figure 3.4(d) where we show the simulated amplitudes C_c and C_s as a function of Δ.

3.2.2 Examples for acceleration efficiency and dephasing length of dielectric double gratings

In the following we will restrict the discussion to double grating structures for which the accelerating force exhibits a cosh-profile, because this is the only case that leads to useful acceleration. Therefore $C_\mathrm{c} = 0$ in Equation 3.9 and 3.10. Similarly to Equation 3.1 we define the acceleration efficiency of the double grating as

$$\epsilon_\mathrm{acc}^\mathrm{dg} := \frac{F_x|_{z=0}}{eE_\mathrm{p}} = \frac{cC_\mathrm{s}}{\beta\gamma E_\mathrm{p}}. \tag{3.11}$$

It relates the axial acceleration gradient $G(z_0 = 0) = F_x|_{z=0}$ to the peak electric field E_p of the exciting laser pulse.

The double grating structure depicted in Figure 3.5 (a) has identical parameters as the sketch shown in Figure 3.4 (a). Its first spatial harmonic is synchronous with non-relativistic ($\beta = 0.33$) electrons. We directly extract C_s from the magnetic field profile according to Equation 3.9. We obtain $C_\mathrm{s} = 9.2 \cdot 10^{-3} E_\mathrm{p}/c$. The corresponding acceleration efficiency is $\epsilon_\mathrm{acc}^\mathrm{dg} = 2.7 \cdot 10^{-2}$. It is twice as large as the acceleration efficiency of a single grating $\epsilon_\mathrm{acc}(\beta = 0.33) = 1.3 \cdot 10^{-2}$, shown in Figure 3.1 (b) on page 29, because both the upper and lower grating of the double grating structure have the optimized parameters of the single grating for the design electron velocity $\beta = 0.33$. This illustrates that the field pattern inside the double grating structure is composed of the two evanescent waves from both gratings, which is schematically depicted in Figure 2.3 on page 22.

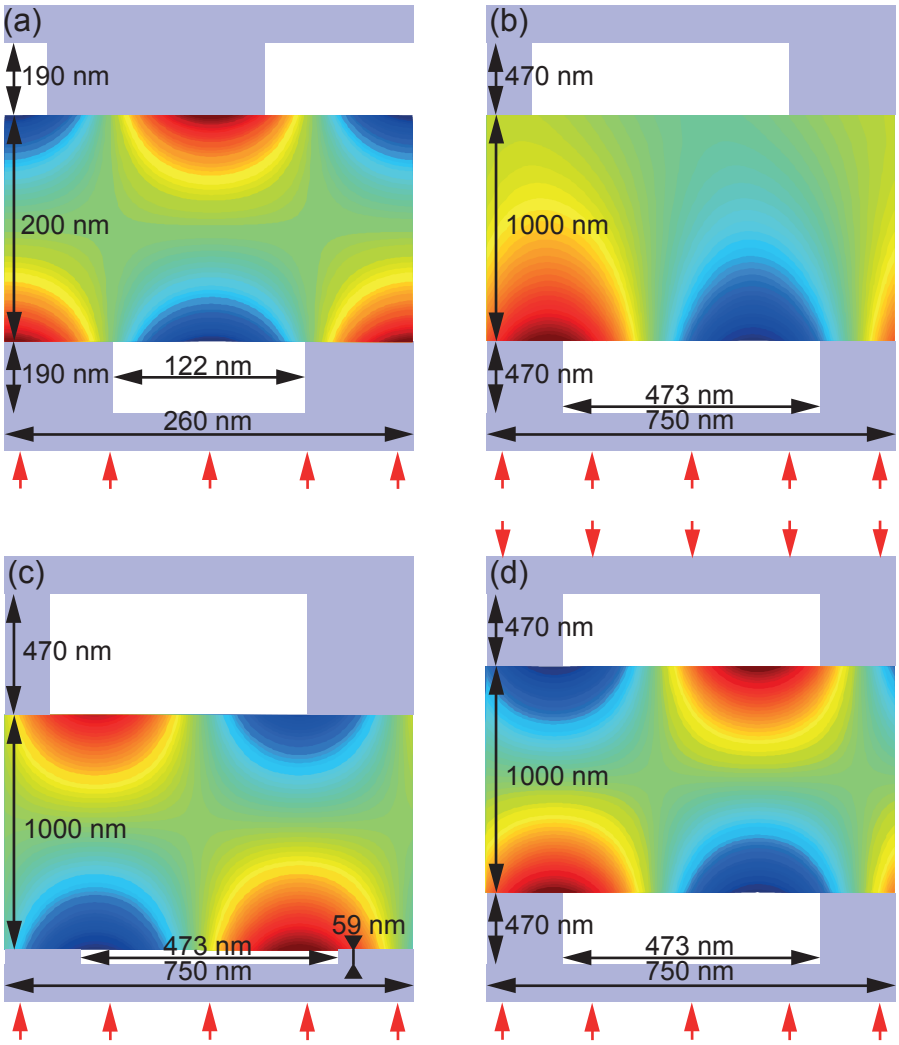

Figure 3.5: Magnetic field distribution of the first spatial harmonic for four different double grating geometries from which we directly extract C_s according to Equation 3.9. The grating parameters are shown in the sketch. The wavelength of the exciting laser is $\lambda = 800\,\mathrm{nm}$. (a), The first spatial harmonic is synchronous with non-relativistic electrons ($\beta = \lambda_p/\lambda = 0.33$). The offset between the upper and lower grating is $\Delta = 0.37\,\lambda_p$. We obtain $C_s = 9.2 \cdot 10^{-3} E_p/c$. In (b-d) the first spatial harmonic is synchronous with relativistic electrons ($\beta = 0.94$). (b), The grating parameters of the lower and upper grating correspond to the optimized values used in Figure 3.2(g-i) on page 30. The offset is $\Delta = -0.08\,\lambda_p$. The excitation efficiency of the spatial harmonic at the upper grating is negligible. Hence, the field profile looks similar to the field profile of a single grating. (c), The grating depth of the lower grating has been reduced to adjust the excitation efficiency at the lower grating to the efficiency of the upper one. This leads to the desired sinh-profile of the magnetic field for single beam illumination ($C_s = 0.05 E_p/c$). (d), Two-sided illumination of the symmetric double grating structure ($\Delta = 0$) also yields the favorable sinh-profile with the advantage of maximum efficiency ($C_s = 0.25 E_p/c$).

$\lambda\,(\mu\mathrm{m})$	$E_{\mathrm{kin}} = 29\,\mathrm{keV}$, $\beta = 0.33$ (Figure 3.5(a))		$E_{\mathrm{kin}} = 957\,\mathrm{keV}$, $\beta = 0.94$ (Figure 3.5(d))	
	$1\,\mathrm{GV/m}$	$10\,\mathrm{GV/m}$	$1\,\mathrm{GV/m}$	$10\,\mathrm{GV/m}$
0.8	$12\,\mu\mathrm{m}$	$4\,\mu\mathrm{m}$	$149\,\mu\mathrm{m}$	$47\,\mu\mathrm{m}$
2	$19\,\mu\mathrm{m}$	$6\,\mu\mathrm{m}$	$236\,\mu\mathrm{m}$	$75\,\mu\mathrm{m}$
5	$31\,\mu\mathrm{m}$	$10\,\mu\mathrm{m}$	$373\,\mu\mathrm{m}$	$118\,\mu\mathrm{m}$

Table 3.1: Dephasing length x_{deph} for non-relativistic (29 keV) and relativistic (957 keV) electrons inside a double grating structure. The 29 keV electrons pass the structure depicted in Figure 3.5 (a) which is excited by a single laser with wavelength λ and peak electric field E_{p}. The 957 keV electrons are accelerated inside the symmetrically pumped structure shown in Figure 3.5 (d), excited by two lasers with λ and E_{p}. We assume an acceleration gradient at the center of the vacuum channel of $G(z_0 = 0) = 0.027 \cdot eE_{\mathrm{p}}$ for the non-relativistic case and $G(z_0 = 0) = 0.09 \cdot eE_{\mathrm{p}}$ for the relativistic case. For $\lambda = 2\,\mu\mathrm{m}$ and $\lambda = 5\,\mu\mathrm{m}$ the dimensions shown in Figure 3.5 have been scaled up. See text for more details.

In Figure 3.5 (b) and (c) we show the magnetic field profile of the first spatial harmonic, which is synchronous with relativistic ($\beta = 0.94$) electrons, for two different double grating geometries illuminated by a *single laser*. In Figure 3.5 (b) the center of the sinh-profile does not coincide with the center of the vacuum channel, which can be explained by a different excitation efficiency of the spatial harmonic at the lower and upper grating. This difference can be compensated by changing the grating parameters of the lower grating (Figure 3.5 (c)) at the expense of a lower acceleration efficiency which we calculate to be $\epsilon_{\mathrm{acc}}^{\mathrm{dg}} = 1.8 \cdot 10^{-2}$, assuming $C_{\mathrm{s}} = 5 \cdot 10^{-2} E_{\mathrm{p}}/c$.

Alternatively, in Figure 3.5 (d) we achieve a symmetric mode profile by illuminating the double grating structure with *two lasers* from both sides [80]. This has the advantage of a maximum efficiency of $\epsilon_{\mathrm{acc}}^{\mathrm{dg}} = 9 \cdot 10^{-2}$, assuming $C_{\mathrm{s}} = 0.25 E_{\mathrm{p}}/c$. Note that for symmetric illumination the offset Δ has to be either zero or half a grating period, otherwise the 1^{st} and $\text{-}1^{\mathrm{st}}$ spatial harmonic are not excited with equal strength. This leads to a skew acceleration profile, because for the upward propagating beam the 1^{st}, and for the downward propagating beam the $\text{-}1^{\mathrm{st}}$ spatial harmonic is synchronous with electrons passing through the structure from left to right.

In Table 3.1 we list the dephasing lengths x_{deph} for the non-relativistic and relativistic electrons inside the double grating structures shown in Figure 3.5 (a) and (d). We have calculated x_{deph} according to Equation 2.23 on page 25 using the maximum acceleration gradient $G_{\mathrm{max}}(z_0 = 0) = \epsilon_{\mathrm{acc}}^{\mathrm{dg}} eE_{\mathrm{p}}$. For example, assuming $E_{\mathrm{p}} = 1\,\mathrm{GV/m}$, 30 keV electrons that are accelerated inside the double grating structure, depicted in Figure 3.5 (a), dephase after only $12\,\mu\mathrm{m}$ with respect to the first spatial harmonic. 1 MeV electrons inside the structure, shown in Figure 3.5 (d), stay in phase with the accelerating fields for about a factor of ten larger distances. Increasing the laser peak field reduces x_{deph} by a factor of

$1/\sqrt{E_\mathrm{p}}$.

The dephasing length scales with the exciting laser's wavelength λ according to $\sqrt{\lambda}$. In the calculation of x_deph we assume the same acceleration efficiency for all wavelengths. This implies, first, that the refractive index of the grating material is constant and, second, that the dimensions of the double grating structures have to be scaled up proportionally to the wavelength. Hence, for an exciting wavelength of 2 μm the dimensions in Figure 3.5 are increased by a factor of 2.5. For $\lambda = 5\,\mu$m the dimensions are a factor of 6.3 larger.

These calculated dephasing lengths are important for the choice of the injection energy of a large-scale DLA, which we discuss in Section 5.2.

3.2.3 Particle tracking simulation

We also perform particle tracking simulations of single electrons in the field of a double grating structure. In contrary to the particle tracking in the fields of a single grating, discussed in Section 3.1.2, here we only include the synchronous spatial harmonic and neglect all other field components. This does not generally pose a problem, because the force exerted onto the electrons by asynchronous modes averages to zero over time. However, it simplifies the input of the field into the simulation, as the synchronous harmonic is specified only by the parameter C_s, according to Equation 3.10. We again only consider modes for which $C_\mathrm{c} = 0$.

The results of a particle tracking simulation for electrons inside the fused silica double grating geometries depicted in Figure 3.5 (a,c,d) are shown in Figure 3.6. We simulate the energy gain, the deflection, as well as the final angle of the electron trajectory with respect to the grating surface. The results can be directly compared with the single grating simulation in Figure 3.2 on page 30. The advantage of the symmetric field pattern can clearly be seen: the energy gain for electrons passing the grating at a distance z_0 from the axis equals the gain for electrons passing at $-z_0$. Moreover there exists an initial start phase ($\sim \pi$) for which electrons starting at positive z_0 are deflected downwards and electrons starting at negative z_0 are deflected upwards. This corresponds to a focusing force towards the axis of the structure. It can also be seen that the acceleration and focusing are out of phase ($\pi/2$ phase shifted), which is expected from Equation 3.10.

In Figure 3.6 (a-c) we show the particle tracking results of non-relativistic 30 keV electrons passing through the double grating structure depicted in Figure 3.5 (a) for a laser peak electric field of $E_\mathrm{p} = 1\,\mathrm{GV/m}$. The maximum on-axis energy gain of $\Delta E = 200\,\mathrm{eV}$ corresponds to a maximum acceleration gradient of $G_\mathrm{max} = \Delta E/(\sqrt{\pi} w_\mathrm{int}) = 26\,\mathrm{MeV/m}$ (Equation 3.6), using $w_\mathrm{int} = 4.3\,\mu$m. This agrees with the above calculated acceleration efficiency of $\epsilon_\mathrm{acc}^\mathrm{dg} = 2.7 \cdot 10^{-2}$ and E_p. Note that if a continuous electron beam is passing through the structure, the beam diameter should be smaller than $\sim$100 nm in order to prevent electrons from being deflected into the grating. This strongly suggests using microbunched electron beams with sub-laser-cycle microbunch durations, that are injected at start phases for which the structure acts both accelerating and focusing.

We further perform particle tracking simulations of relativistic 1 MeV electrons inside

the double gratings depicted in Figure 3.5 (c) and (d). In Figure 3.6 (d-f), corresponding to Figure 3.5 (c), we use a laser peak field of $E_\mathrm{p} = 10\,\mathrm{GV/m}$. Again, the maximum on-axis energy gain of $\Delta E = 1.5\,\mathrm{keV}$, which translates into $G_\mathrm{max} = \Delta E/(\sqrt{\pi} w_\mathrm{int}) = 170\,\mathrm{MeV/m}$ ($w_\mathrm{int} = 4.9\,\mu\mathrm{m}$), agrees with the previously calculated acceleration efficiency of $\epsilon_\mathrm{acc}^\mathrm{dg} = 1.8 \cdot 10^{-2}$.

In Figure 3.6 (g-i) 1 MeV electrons pass through the symmetrically pumped structure shown in Figure 3.5 (d). Here we choose a laser peak electric field of $E_\mathrm{p} = 7\,\mathrm{GV/m}$ in each laser beam, reduced by a factor of $1/\sqrt{2}$ compared to the single beam illumination. Therefore the overall fluence remains constant and damage to the grating is prevented. Hence, we can directly compare the two-beam with the single-beam excitation. The maximum on-axis energy gain of around 6 keV in Figure 3.6 (g) also agrees with the above computed acceleration efficiency of $\epsilon_\mathrm{acc}^\mathrm{dg} = 9 \cdot 10^{-2}$.

From these simulations it becomes clear that relativistic electrons are less affected by deflecting forces. Together with the other advantage of wider possible vacuum channels in double grating structures designed for relativistic particle acceleration, this also allows using larger electron beams (here: up to 800 nm in diameter). Consequently, larger beam currents are permitted, as will be discussed in Section 5.1.

3.3 Simulation of acceleration at the single grating used in the experiment

Here we present simulations of the particle acceleration for the fused silica grating that has been used in the experiment. The experimental parameters, which will discussed in detail in Chapter 4, are: grating period $\lambda_\mathrm{p} = 750\,\mathrm{nm}$, laser wavelength $\lambda = 787\,\mathrm{nm}$ and laser peak electric field $E_\mathrm{p} = 2.85\,\mathrm{GV/m}$. We exploit the third spatial harmonic of the grating and hence synchronously accelerate $\beta = \lambda_\mathrm{p}/(3\lambda) = 0.32$ (27.9 keV) electrons. An

Figure 3.6 *(following page)*: Particle tracking results of a single electron interacting with laser pulses in a fused silica double grating structure. Here we neglect all asynchronous modes. The laser parameters are: wavelength $\lambda = 800\,\mathrm{nm}$, focal waist radius $w_\mathrm{l} = 5\,\mu\mathrm{m}$, pulse duration $\tau_\mathrm{p} = 100\,\mathrm{fs}$, laser peak electric field $E_\mathrm{p} = 1\,\mathrm{GV/m}$ (a-c), $E_\mathrm{p} = 10\,\mathrm{GV/m}$ (d-f) and $E_\mathrm{p} = 7\,\mathrm{GV/m}$ (g-i). The initial electron energy is $E_\mathrm{kin} = 29\,\mathrm{keV}$ ($\beta = 0.33$) (a-c) and $E_\mathrm{kin} = 957\,\mathrm{keV}$ ($\beta = 0.94$) (d-i). (a-c), Grating parameters from Figure 3.5(a). (d-f), Grating parameters from Figure 3.5(c). (g-i), Grating parameters from Figure 3.5(d). Color-coded plots show the energy gain ΔE_kin (a,d,g), the deflection Δz (b,e,h) and the final angle β_z/β_x (c,f,i) as a function of the initial distance z_0 from the axis of the double grating and of the initial phase between the electron and the laser field. For the white areas the electron is deflected into the grating during the simulation. The characteristic interaction distance is $w_\mathrm{int} = 4.3\,\mu\mathrm{m}$ (a-c) and $w_\mathrm{int} = 4.9\,\mu\mathrm{m}$ (d-i). See text for more details.

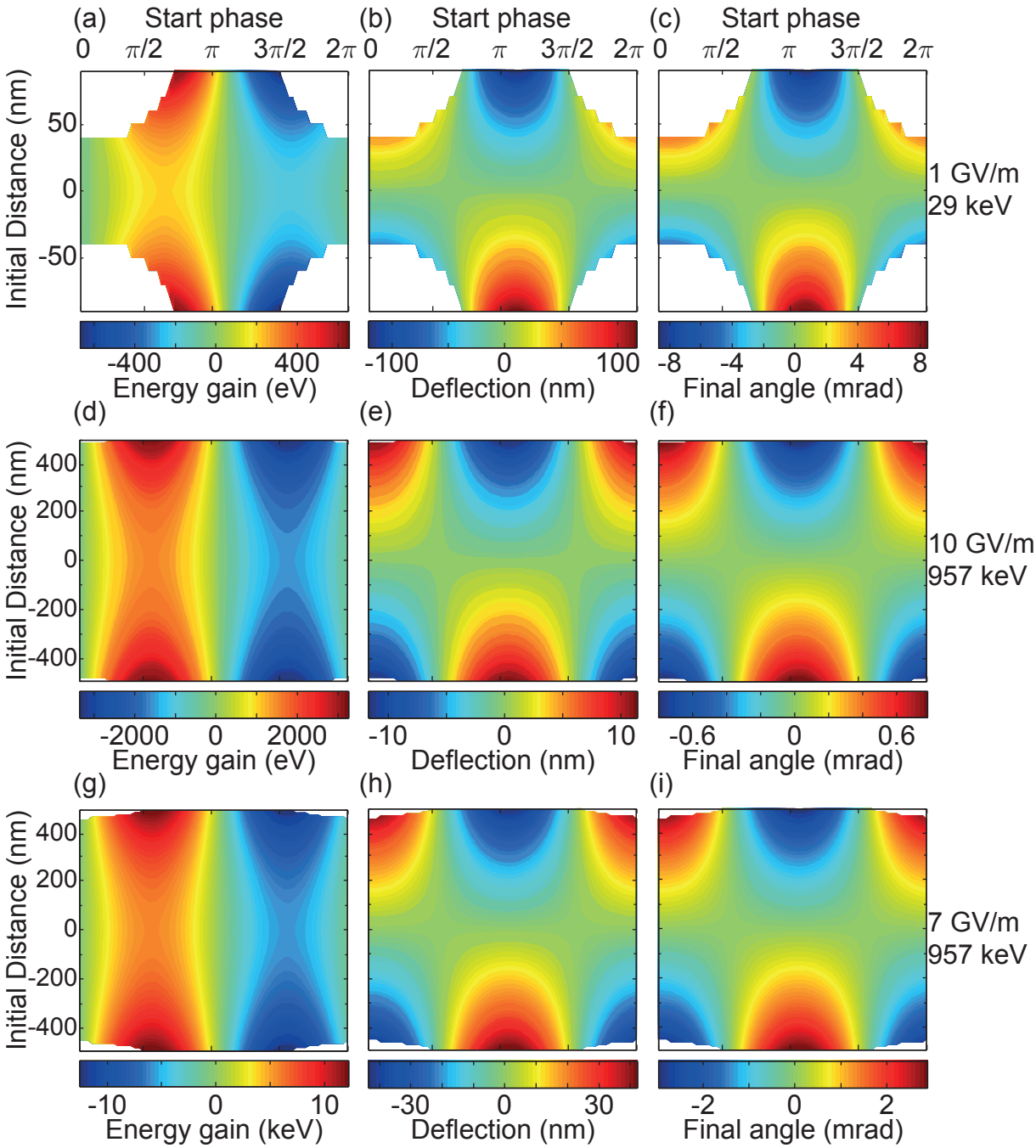
(a) Start phase
(b) Start phase
(c) Start phase
0 π/2 π 3π/2 2π
Initial Distance (nm)
50
0
-50
-400 0 400
Energy gain (eV)
-100 0 100
Deflection (nm)
-8 -4 0 4 8
Final angle (mrad)
1 GV/m
29 keV
(d)
(e)
(f)
400
200
0
-200
-400
-2000 0 2000
Energy gain (eV)
-10 0 10
Deflection (nm)
-0.6 0 0.6
Final angle (mrad)
10 GV/m
957 keV
(g)
(h)
(i)
-10 0 10
Energy gain (keV)
-30 0 30
Deflection (nm)
-2 0 2
Final angle (mrad)
7 GV/m
957 keV

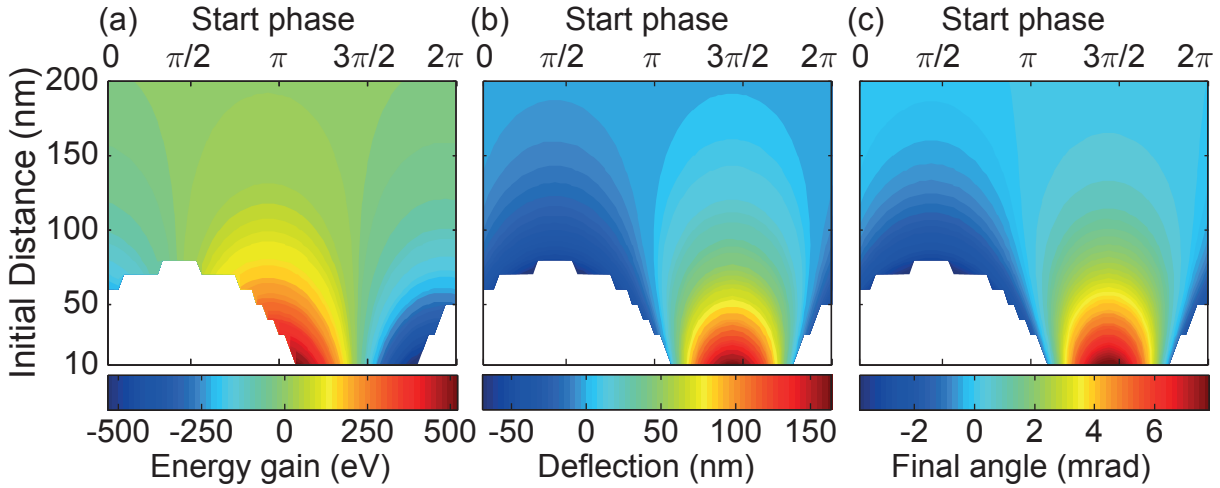

Figure 3.7: Particle tracking results of a single electron interacting with the laser pulses in close proximity of the fused silica grating used in the experiment. The experimentally realized laser parameters are: wavelength $\lambda = 787\,\mathrm{nm}$, focal waist radius $w_\mathrm{l} = 9\,\mu\mathrm{m}$, pulse duration $\tau_\mathrm{p} = 110\,\mathrm{fs}$ and laser peak electric field $E_\mathrm{p} = 2.85\,\mathrm{GV/m}$. The initial electron energy is $E_\mathrm{kin} = 27.9\,\mathrm{keV}$ ($\beta = 0.32$), hence electrons interact synchronously with the third spatial harmonic. Color-coded plots show the energy gain ΔE_kin (a), the deflection Δz (b) and the final angle β_z/β_x (c) as a function of the initial distance z_0 from the grating and the initial phase between the electron and the laser field. For the white areas the electron crashes into the grating during the simulation. The characteristic interaction distance is $w_\mathrm{int} = 6.3\,\mu\mathrm{m}$ (see Equation 3.5).

image of the grating, which we use in the experiment, is shown in Figure 4.4 on page 49.

From the eigenmode expansion method we infer an excitation efficiency (Equation 3.2) of $\epsilon_\mathrm{exc} = cB_y^{(3)}/E_\mathrm{p} = 0.01$. Therefore we obtain an acceleration efficiency (Equation 3.1)

$$\epsilon_\mathrm{acc} = 0.03e^{-z_0/\delta}, \tag{3.12}$$

as function of distance from the grating surface z_0, with the decay constant $\delta = 42\,\mathrm{nm}$ (Equation 2.8).

The results of a particle tracking simulation, depicted in Figure 3.7, show the same characteristics as discussed in Section 3.1.2. For example, we calculate a maximum energy gain $\Delta E = 90\,\mathrm{eV}$ at $z_0 = 100\,\mathrm{nm}$. This corresponds to a maximum acceleration gradient of $G_\mathrm{max} = \Delta E/(\sqrt{\pi} w_\mathrm{int}) = 8\,\mathrm{MeV/m}$ ($w_\mathrm{int} = 6.3\,\mu\mathrm{m}$), which perfectly agrees with $\epsilon_\mathrm{acc}(z_0 = 100\,\mathrm{nm}) = 2.7 \cdot 10^{-3}$ and $E_\mathrm{p} = 2.85\,\mathrm{GV/m}$. The maximum energy gain in Figure 3.7 (a) decays exponentially with increasing distance from the grating with a decay constant $\delta = 42\,\mathrm{nm}$, as expected. Note that most of the electrons passing the grating surface at distances below $\sim$50 nm crash into the grating and thus cannot be detected. A minimal distance of 50 nm agrees well with the measured maximum acceleration gradient of 25 MeV/m, discussed in Section 4.3.

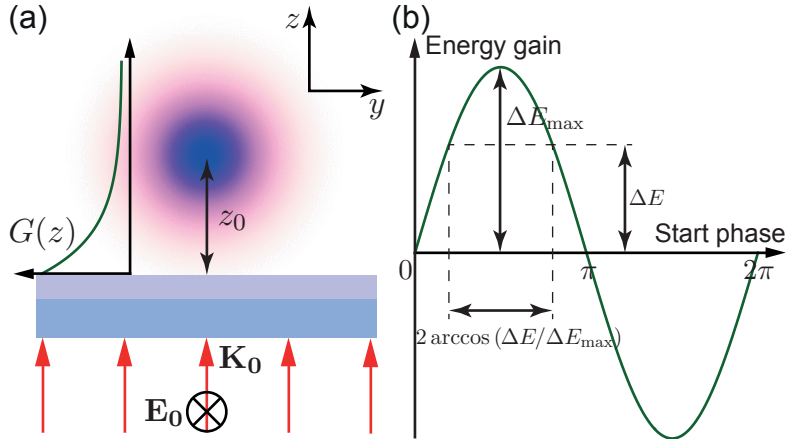

Figure 3.8: (a), Side view of a dielectric grating (light blue) with an electron beam (dark blue) passing at a distance z_0. The laser is incident from below (red arrows). We assume a constant laser field over the width of the Gaussian electron beam profile ($w_\mathrm{l} \gg w_\mathrm{e}$) and model a 1D Gaussian current density (Equation 3.14) being subject to the acceleration gradient $G(z) = 0.03 \cdot eE_\mathrm{p} \exp(-z/\delta)$, with $\delta = 42\,\mathrm{nm}$. (b), Energy gain as a function of start phase at a fixed distance from the grating surface (corresponding to a horizontal slice in Figure 3.7 (a)). The differential accelerated fraction at this distance equals $\zeta(\Delta E, z) = \arccos(\Delta E/\Delta E_\mathrm{max}(z))/\pi$.

The accelerated fraction is defined as the ratio of the number of accelerated electrons I_acc to the number of electrons I_eff that can interact with the laser pulse:

$$\alpha := \frac{I_\mathrm{acc}}{I_\mathrm{eff}}. \tag{3.13}$$

To calculate α based on the simulation results we assume a Gaussian-shaped electron beam current density

$$j(z) = \frac{I_\mathrm{eff}}{\sqrt{\pi} w_\mathrm{e}} e^{-(z-z_0)^2/w_\mathrm{e}^2}, \tag{3.14}$$

with the $1/e$ electron beam waist w_e (Figure 3.8 (a)). In the experiment we measure an integrated accelerated fraction $\alpha(\Delta E)$. That is the integrated signal of electrons which are accelerated sufficiently to pass the spectrometer and therefore gain more energy than $\Delta E = eU_\mathrm{G} - eU_\mathrm{G}^0$. Here, U_G is the applied spectrometer voltage and U_G^0 is the center spectrometer voltage of the energy spectrum, defined in Figure 4.8 (a) on page 55. We derive

$$\alpha(\Delta E) = \frac{1}{I_\mathrm{eff}} \cdot \int_{50\,\mathrm{nm}}^{z_\mathrm{max}} \zeta(\Delta E, z) j(z) f_\mathrm{rep} \tau_\mathrm{p}\, \mathrm{d}z, \tag{3.15}$$

with the differential accelerated fraction $\zeta(\Delta E, z)$ as a function of distance z and energy gain ΔE (Figure 3.8(b)), the maximum distance z_max at which electrons gain more energy than ΔE and the laser repetition rate f_rep. z_max can be directly obtained by rearranging

Equation 3.1, 3.2 and 3.6:

$$z_{\max} = \delta \ln\left(\frac{eE_{\mathrm{p}}\epsilon_{\mathrm{exc}}\sqrt{\pi}w_{\mathrm{int}}}{\beta\gamma\Delta E}\right) = 42\,\mathrm{nm}\cdot\ln\left(\frac{942\,\mathrm{eV}}{\Delta E}\right). \tag{3.16}$$

For example, electrons have to pass the grating within $z_{\max} = 94\,\mathrm{nm}$ to gain more than 100 eV in energy. The lower bound of the integral reflects the assumption that electrons cannot pass the grating any closer than 50 nm. It agrees well with $z_{\max}$ for the maximum measured energy gain of $\sim$280 eV, shown in Figure 4.12 on page 61. The factor $f_{\mathrm{rep}}\tau_{\mathrm{p}}$ corresponds to the fraction of time during which the electrons can effectively interact with the laser pulses. In the end we scale the overall amplitude of α to fit the experimental data.

With those simulation results at hand we can discuss the experimental data which is presented in the next chapter.

Chapter 4

Measurement of dielectric laser acceleration of 28 keV electrons

In this chapter we describe the experimental setup. We discuss the choice of the grating geometry and the employed scheme to overlap the electron beam with the laser at the grating surface. We also present a detailed description of the applied measurement technique. At the end we discuss the measurement results which confirm direct electron acceleration with the laser field in the vicinity of a fused silica grating via the inverse Smith-Purcell effect. They are in excellent agreement with the simulations. The results and discussion presented in this chapter follow [126, 139].

4.1 Experimental setup

A conceptual picture of the setup is shown in Figure 4.1. It shows the electron column of a conventional scanning electron microscope (SEM) which provides a well-controlled electron beam that passes the grating. Here the electrons interact with the synchronous (third) spatial harmonic which is excited by laser pulses from below. After the interaction the electrons enter a spectrometer that measures their energy gain.

4.1.1 Overview

In Figure 4.2 we show a detailed drawing of the inside of the vacuum chamber in which the experiment is conducted. The electron beam coming from the right passes through the interaction region. Here, it interacts with the evanescent field excited at the grating surface by laser pulses impinging from behind. The electrons enter a filter lens spectrometer. Accelerated electrons that pass the spectrometer are deflected by a magnetic field and are detected with a microchannel plate detector (MCP). The beam is deflected to reduce the background signal at the detector, as discussed below in Section 4.2. A camera, placed outside the vacuum chamber, can be used to observe the MCP counts. However, we

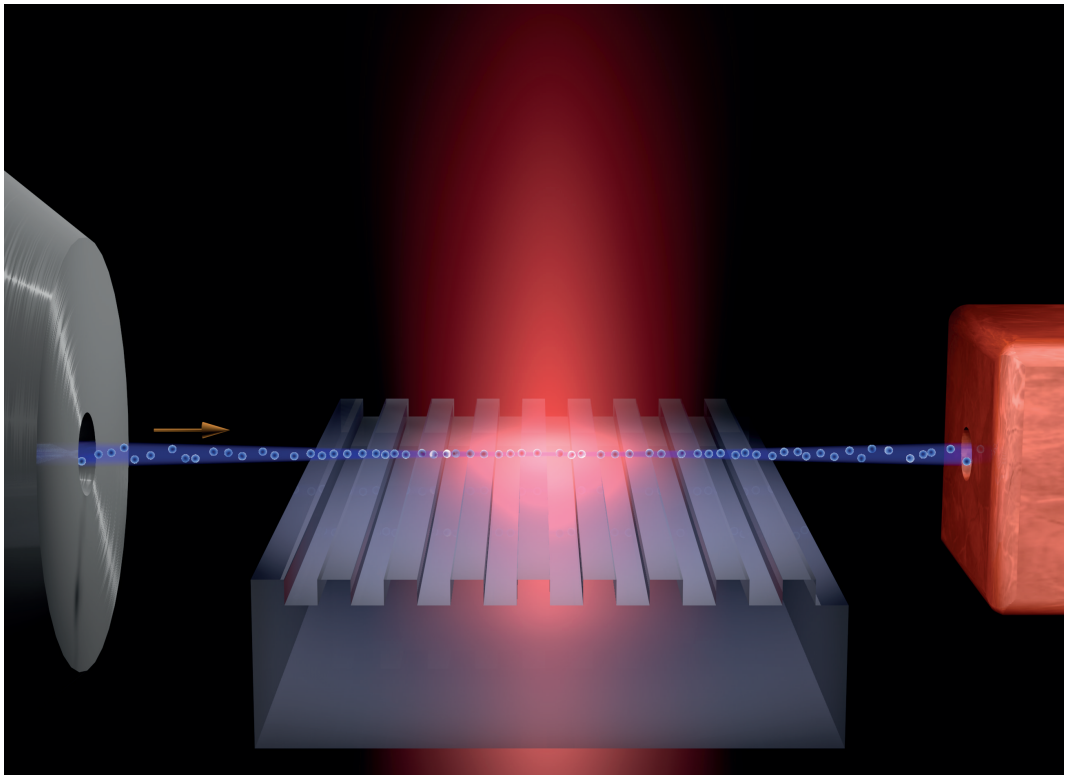

Figure 4.1: Conceptual picture of the experimental setup. Electrons (blue circles) derived from an electron column (left) pass a grating (center) and interact with evanescent modes excited by a laser pulse (red). Finally, the electrons enter the spectrometer on the right.

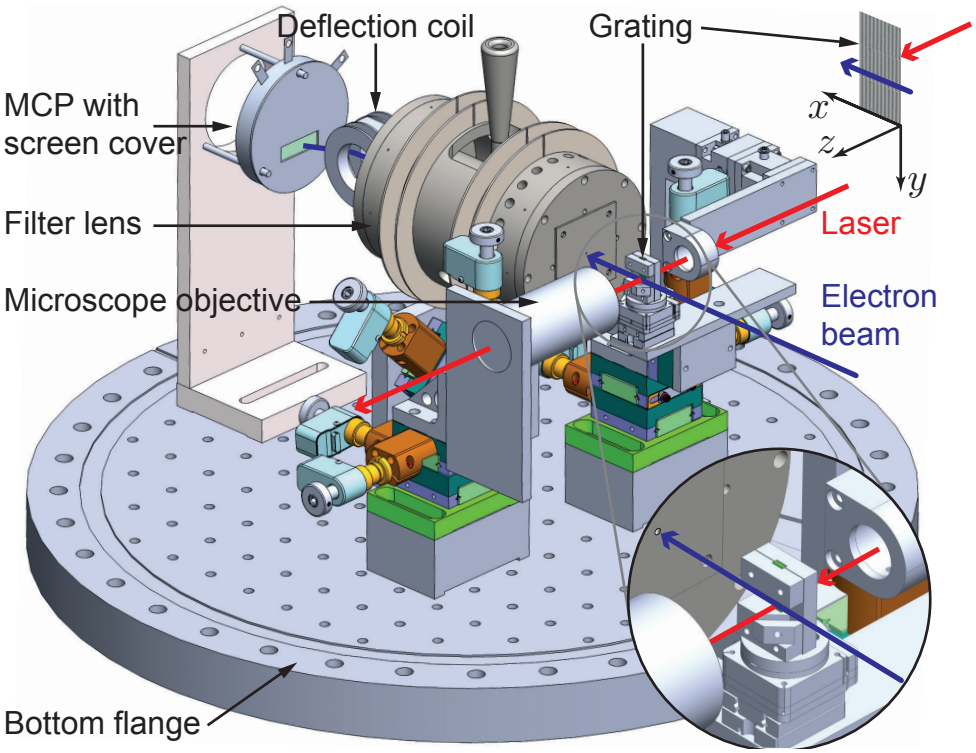

Figure 4.2: Technical drawing of the experimental setup. A zoom-in of the interaction region is shown and the grating orientation is indicated in the upper right corner. The experiment is placed inside a vacuum chamber. The microscope objective (xyz-degrees of freedom), the spectrometer (yz-degrees of freedom) and the grating mount (xyz-degrees of freedom) can be positioned relative to the electron beam with translation stages (Newport 9066 with Picomotor$^{\text{TM}}$ actuators). Additionally, the grating can be fine positioned with stick-slip piezoelectric actuators, a Smaract SLC-17 (z-direction) and a Smaract SR-1908 (rotation in xz-plane). The achromatic lens which is used to focus the laser pulses can be manually positioned with a compact dovetail linear stage (Newport DS25-XYZ). See text for more details.

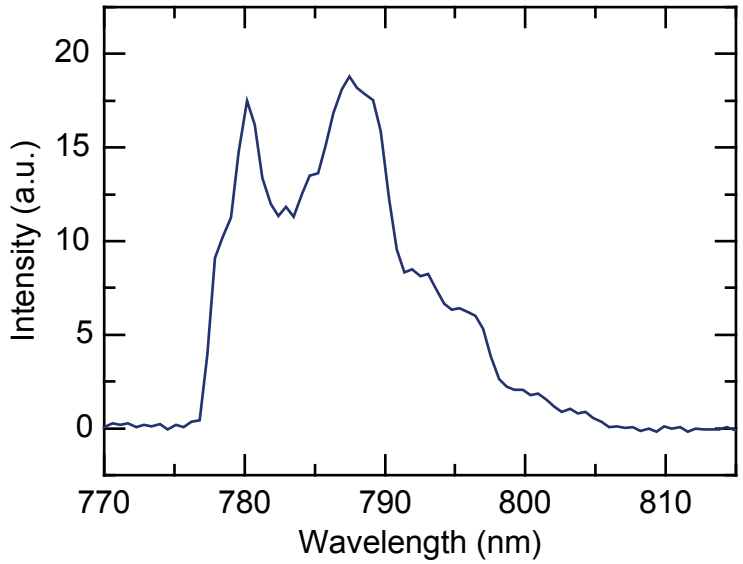

Figure 4.3: Typical spectrum of the Ti:Sa laser oscillator with central wavelength $\lambda = 787\,\mathrm{nm}$. The corresponding pulse duration is $\tau_\mathrm{p} = 110\,\mathrm{fs}$, measured with an autocorrelator (APE PulseCheck).

electronically detect the counts in our the detection scheme and therefore do not show this camera in Figure 4.2.

For the alignment procedure, which we discuss in Section 4.1.3, a microscope objective (Mitutoyo, M Plan NIR 10x) is placed inside the vacuum chamber for monitoring the electron beam, laser and grating position. Moreover, various positioning degrees of freedom are required and shown in Figure 4.2.

4.1.2 Laser parameters

As a laser source we use a Titanium:sapphire (Ti:Sa) long-cavity oscillator with a repetition rate $f_\mathrm{rep} = 2.7\,\mathrm{MHz}$, a center wavelength $\lambda = 787\,\mathrm{nm}$, a pulse duration $\tau_\mathrm{p} = 110\,\mathrm{fs}$ and a pulse energy of 160 nJ, corresponding to 450 mW average output power [140]. A typical spectrum is shown in Figure 4.3. The laser pulses are focused by an achromatic lens (Edmund Optics, NT45-827) with a focal length of 30 mm onto the grating. The focal waist radius is $w_\mathrm{l} = (9.0 \pm 0.4)\,\mu\mathrm{m}$.

4.1.3 Grating

Grating geometry and parameters

The fused silica grating, shown in Figure 4.4 (a,b), has been manufactured using electron beam and laser lithography as well as reactive ion etching, as described in Appendix A. With the laser wavelength of 787 nm, a grating period of 250 nm is needed to accelerate

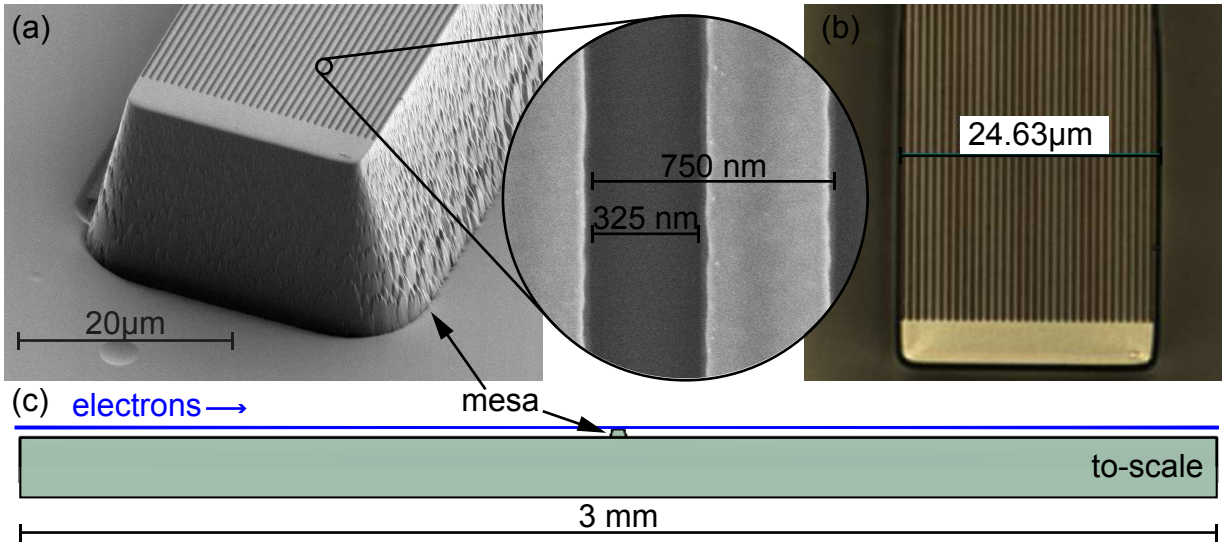

Figure 4.4: (a), Electron microscope image of the fused silica grating that is located on top of a mesa, 20 μm above the substrate. The zoom-in shows the grating with a grating period $\lambda_p = 750$ nm, a trench width of 325 nm and a depth of 280 nm. (b), Top view of the mesa with a width of 25 μm, recorded with an optical microscope. (c), To-scale sectional view of the mesa on top of the substrate. The mesa allows the electron beam to approach the grating closely without being clipped at the 3 mm-wide substrate.

$E_{kin} = 27.9$ keV electrons ($\beta = 0.32$) using the first spatial harmonic. Due to a lower bound of $\lambda_p \gtrsim 600$ nm set by the manufacturer[1], we chose a grating period of $\lambda_p = 750$ nm and use the third spatial harmonic. The grating is located on top of a mesa with dimensions 2 mm x 25 μm x 20 μm (length x width x height), which sits on top of the substrate with dimensions 3 mm x 20 mm x 1 mm (length x width x height). This mesa structure allows spatial access to the grating, i.e., the electron beam can pass by the grating surface at distances <100 nm without beam clipping at the glass substrate, shown in Figure 4.4 (c). This geometry therefore also minimizes surface charging, which leads to deflection of the beam.

To further reduce surface charging we first coated the sample (i.e., grating and substrate) with a 3 nm thick titanium layer. Afterwards we masked the mesa with a mechanical shadow mask and coated the surrounding substrate with a 10 nm gold layer. In a first attempt we coated the grating with gold as well, but laser irradiation melted the gold coating and formed a grained layer (Figure 4.5), which prevented approaching the grating surface closer than ~200 nm. Although the titanium layer is sublimated locally by the laser pulses, it does not form nanoparticles. We observe local charging of the grating surface where the titanium is locally ablated as indicated by electron beam deflection, which occurs when clipping the electron beam with the mesa. But laser irradiation of the grating reduces the surface charging. We assume that this can be explained by local

[1]Fraunhofer Institute for Applied Optics and Precision Engineering, Jena, Germany

heating of the fused silica by the laser pulses which increases the surface conductivity.

Damage threshold measurement

A damage threshold measurement of the gold-coated fused silica grating is shown in Figure 4.5. The measured damage threshold fluence of $0.5\,\mathrm{J/cm^2}$ is a factor of 3 smaller than reported in [138]. For this measurement we use a tighter laser focus of $5\,\mu$m and shorter 70 fs pulses. However, in this short-pulse regime the laser spectrum was unstable and mode-locking could not be maintained for more than a couple of minutes. That is why the main experiment was conducted with longer 110 fs pulses.

The discrepancy between our measurement and the reported damage threshold might be due to the shorter laser pulse duration as compared with the previous measurement, in which 1 ps pulses have been used [138]. This is supported by a fused silica damage threshold measurement from Lenzner *et al.*, who measure an about twice as large damage threshold for 1 ps pulses as compared with 100 fs pulses [71]. Another reason may be a field enhancement at the gold nanoparticles, although the gold layer is already ablated below the damage threshold.

Alignment procedure of electron beam, laser and grating

We coated a grating substrate with fine grain phosphor to measure the overlap between the laser focus and the electron beam above the grating surface (Figure 4.6 (a)). The median phosphor grain size is $2.5\,\mu$m, much smaller than the mesa height. Here the mesa was covered with a mask to keep the grating clear. Details of the coating procedure are discussed in Appendix B.

In the experiment we first align the axis of the spectrometer, which is located on a translation stage (Figure 4.2), with the axis of the electron column. This is done by operating the column in SEM imaging mode and centering the spectrometer entrance within the scanning area of the column. Similarly, we position the grating parallel and closely (within $\sim 1\,\mu$m) to the electron beam by translating and rotating the grating while observing the live SEM image.

From now on the electron beam is fixed in space by turning off the scanning mode of the SEM. The laser focus, monitored by the microscope objective, is then overlapped vertically with the beam (Figure 4.6 (b)) and horizontally with the mesa. Once the coarse alignment between the electron beam and the laser focus using the phosphor-coated grating has been found, fine-adjustment is achieved by monitoring the electron beam deflection (i.e., beam walk-off on a second timescale) while moving the edge of the mesa structure into the beam. Good overlap is indicated by minimal deflection, because laser irradiation reduces surface charging, as discussed above. With this fine-adjustment procedure at hand we can exchange the grating without need for another coarse alignment.

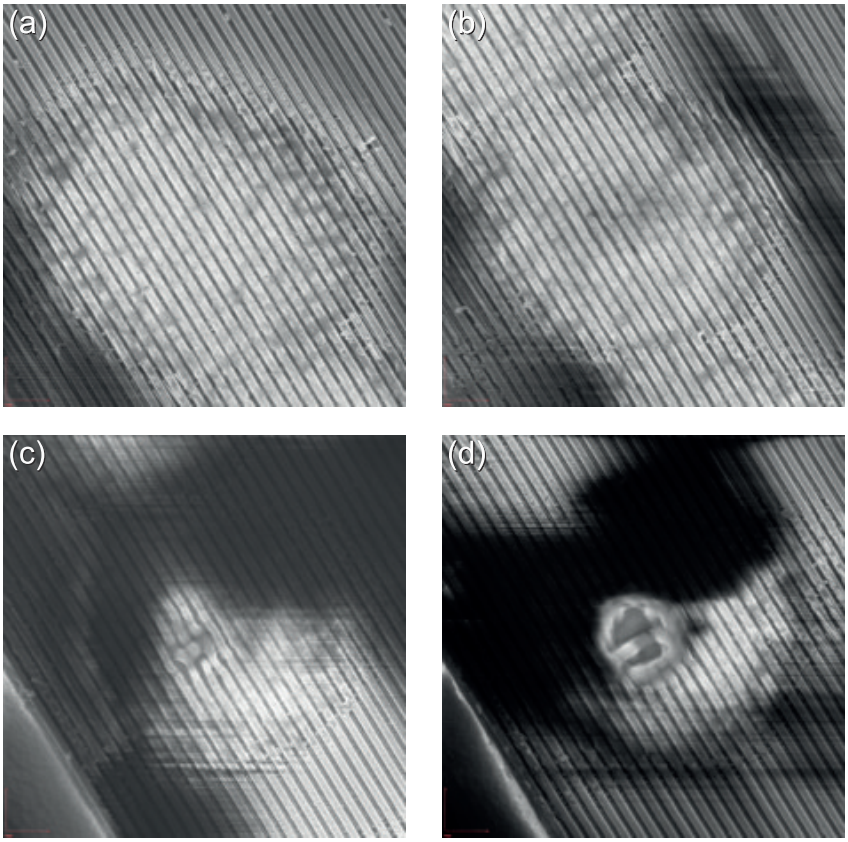

Figure 4.5: Laser damage threshold measurement of a 10 nm gold-coated fused silica grating performed under vacuum ($\sim 10^{-6}$ mbar). Shown are scanning electron microscope images of the grating after irradiation with laser pulses for less than a minute. All four measurements are performed at different locations of the grating, which instantly experienced the full laser power, i.e., there was no slow ramp-up of the power. (a), Ablation of gold coating and formation of gold nanoparticles around the laser focus. Laser parameters: average power $P = 400\,\mathrm{mW}$, peak electric field $E_\mathrm{p} = 6.1\,\mathrm{GV/m}$, peak intensity $I_\mathrm{p} = 1.0 \cdot 10^{13}\,\mathrm{W/cm^2}$, peak fluence $F_\mathrm{p} = 0.37\,\mathrm{J/cm^2}$. (b), Small visible distortion of the grating in the beam center. Laser parameters: $P = 500\,\mathrm{mW}$, $E_\mathrm{p} = 6.9\,\mathrm{GV/m}$, $I_\mathrm{p} = 1.3 \cdot 10^{13}\,\mathrm{W/cm^2}$, $F_\mathrm{p} = 0.47\,\mathrm{J/cm^2}$. (c), Visible damage to the grating. Laser parameters: $P = 550\,\mathrm{mW}$, $E_\mathrm{p} = 7.2\,\mathrm{GV/m}$, $I_\mathrm{p} = 1.4 \cdot 10^{13}\,\mathrm{W/cm^2}$, $F_\mathrm{p} = 0.51\,\mathrm{J/cm^2}$. (d), Melting of fused silica. Laser parameters: $P = 620\,\mathrm{mW}$, $E_\mathrm{p} = 7.6\,\mathrm{GV/m}$, $I_\mathrm{p} = 1.5 \cdot 10^{13}\,\mathrm{W/cm^2}$, $F_\mathrm{p} = 0.57\,\mathrm{J/cm^2}$. The large dark areas in (c) and (d) indicate surface charging.

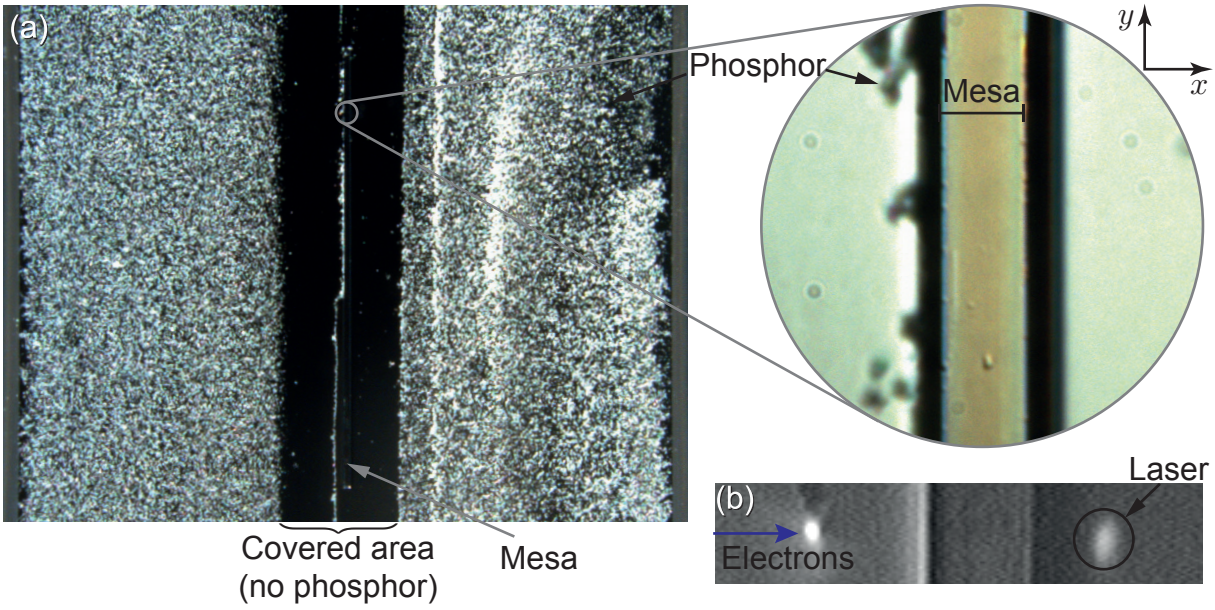

Figure 4.6: (a), Microscope image of the phosphor-coated grating with zoom-in of the mesa. The phosphor (white grains) covers the substrate except for a 0.5 mm wide area around the mesa, which was covered during the coating procedure. For coarse alignment of the laser focus we use phosphor grains that have by chance accumulated right next to the mesa inside the otherwise phosphor-free region. (b), Image of the phosphor-coated grating (mesa in the center) in the experiment recorded with the microscope objective (Figure 4.2). A single grain of phosphor is illuminated by the electron beam (white spot, left). We vertically overlap the laser focus (right). In this alignment procedure the grating is slightly tilted around the y-axis, such that the electron beam is not clipped at the substrate.

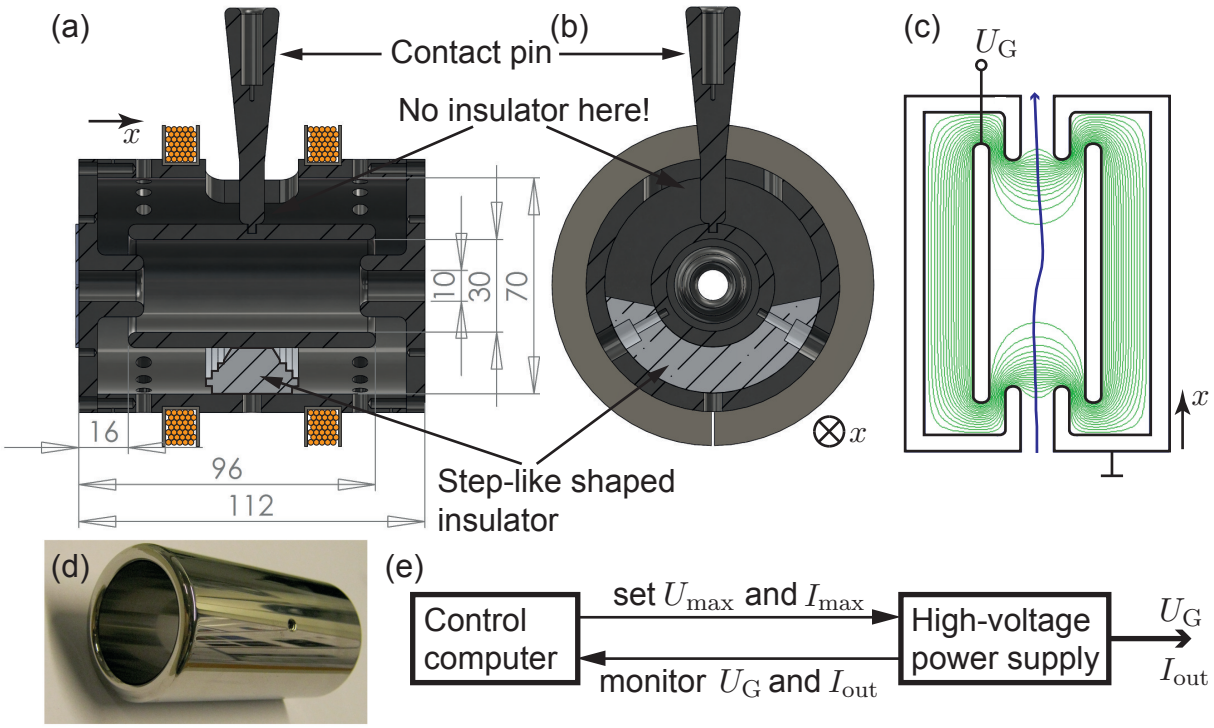

Figure 4.7: (a,b), Sectional views of the electrostatic filter lens with dimensions in mm. We use stainless steal electrodes (dark gray). The vespel insulator (light gray) has been designed following the example of [141, 142]. Multiple steps near the cathode collect emitted electrons, resulting in a space charge that lowers the surface electric field at the cathode and reduces electron emission [141]. The two circular u-profiles are coiled with wires (orange circles) to apply an axial magnetic field, which we did not use during the experiment as it distorted the electron beam focus at the grating. (c), Charged particle optics (CPO) simulation of the filter lens for $U_G = -28.2\,\mathrm{kV}$ with the electrodes (black lines), equipotential surfaces (green lines) and a sample trajectory of a 28 keV electron (blue). From the CPO simulation we infer an offset between the applied voltage U_G and the potential barrier at the center of the filter lens of 260 V due to field penetration, which is why the electron still passes for the given numbers. (d), Picture of inner electrode that has been superpolished to prevent high-voltage breakdown. (e), Schematic illustration of the high-voltage control. A control computer is used to set the maximum voltage U_{max} and current I_{max} of the high-voltage (HV) power supply. It is also used to monitor the actual output voltage U_G and current I_{out}. See text for more details.

4.1.4 Filter lens spectrometer

To measure the electron energy we use an electrostatic filter lens designed in the style of [143], shown in Figure 4.7 (a-c). The design of the electrode and insulator geometry as well as high-voltage conditioning has been crucial to prevent high-voltage breakdown. Breakdowns mostly originate at the metal-dielectric junction [144], which is why we removed any insulating material around the contact pin and chose a specific step-like shape for the vespel insulator [141, 142]. Furthermore, the inner electrode has been mechanically polished to almost mirror quality (Figure 4.7 (d)).

In Figure 4.7 (e) we show a schematic diagram of the high-voltage (HV) control. We use a switch mode HV power supply (Heinzinger PNC 100000-1 neg) which provides a negative static voltage up to $-100\,\mathrm{kV}$ and currents up to 1 mA. To control and monitor the HV output we use its analog interface. A control computer supplies two voltages that are related to the desired output voltage U_{max} and I_{max}. As we are only interested in generating a static counter voltage to block all unaccelerated electrons in the experiment, we set I_{max} to the lowest possible value of $\sim 40\,\mu\mathrm{A}$. In the case of normal operation, the output voltage of the power supply equals the set voltage, i.e., $U_{\mathrm{G}} = U_{\mathrm{max}}$, and the output current $I_{\mathrm{out}} \sim 0$. However, during a HV breakdown event $U_{\mathrm{G}} < U_{\mathrm{max}}$ and $I_{\mathrm{out}} = I_{\mathrm{max}}$. To monitor the actual output parameters the HV power supply provides two monitor voltages that are proportional to U_{G} and I_{out}, which we measure with the control computer.

High-voltage conditioning is a well-known procedure to improve the insulation [145, 146]. Before measurements we routinely increase U_{G} starting from $\sim 20\,\mathrm{kV}$ to 35 kV in 1 kV-steps as soon as there are less than three high-voltage breakdown events in 20 minutes, i.e., events with $U_{\mathrm{G}} < U_{\mathrm{max}}$ and $I_{\mathrm{out}} = I_{\mathrm{max}} \sim 40\,\mu\mathrm{A}$. U_{G} is then kept at 35 kV at least overnight before performing a measurement. Anytime the high-voltage has been turned off this procedure has to be repeated. The whole conditioning process takes typically 12 to 18 hours. More time is required after the initial assembly of the spectrometer, because breakdown events can originate at surface contaminations that are removed during the conditioning.

4.1.5 Electron source

The electrons are derived from the column of a conventional SEM (Hitachi S-570) providing energies of up to 30 keV. The acceleration voltage U_{acc} is generated by an internal power supply inside the SEM control unit. In Figure 4.8(a) we show a measurement of the integrated energy spectrum which we recorded by blocking the electron beam by increasing U_{G} inside the filter lens spectrometer and integrating the intensity of MCP images. We measure a spectral energy width of 10 eV. This value represents an upper limit on the energy spread of the beam as well as on the voltage fluctuations between the two independent power supplies that generate U_{acc} and U_{G}. For U_{G} the voltage fluctuations are specified to be smaller than $\sim 3\,\mathrm{V}$.

At a working distance of 25 mm, the $1/e$ focal waist radius is $w_{\mathrm{e}} = (70 \pm 20)\,\mathrm{nm}$, as inferred from knife-edge measurements, e.g., shown in Figure 4.8(b). The DC beam

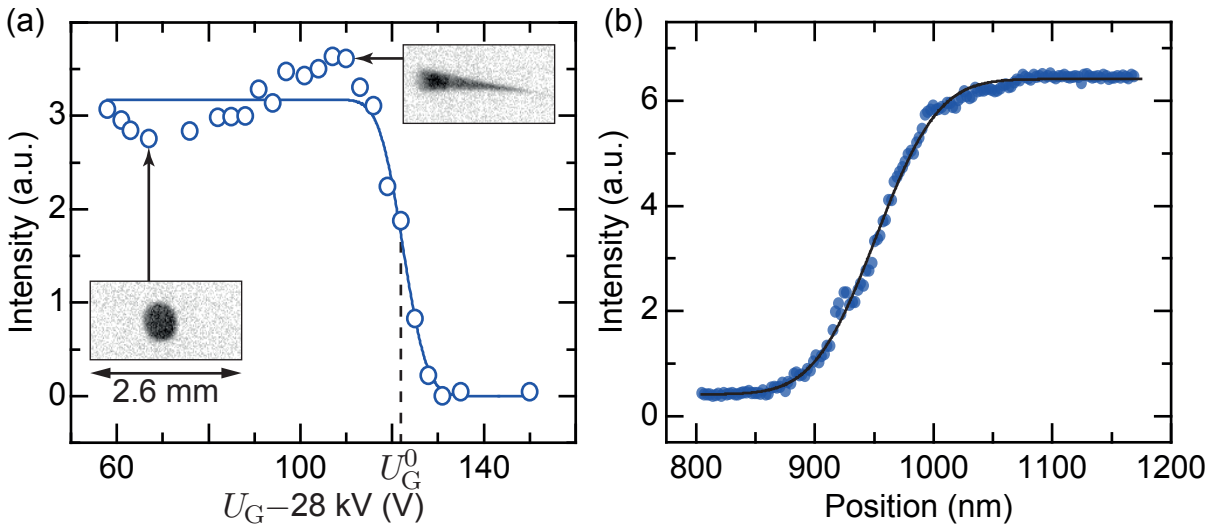

Figure 4.8: (a), Integrated energy spectrum of the electron beam measured with the retarding field spectrometer shown in Figure 4.7. The fitted width of the cut-off edge is 9.7 eV (FWHM), at a center spectrometer voltage $U_G^0 = 28122$ V. The intensity in (a) and (b) has been obtained by integrating the intensity of MCP images. The wavy behavior between 60 V and 110 V is due to defocusing of the electron beam by the retarding field analyzer acting as an einzel lens. The integrated intensity appears smaller if the electron beam is more localized on the MCP. Corresponding MCP images (gray scale; white: no electrons) are shown as insets. (b), Typical measurement of the electron beam focal spot size measured by moving the edge of the mesa structure into the beam (knife-edge method). The fit corresponds to a $1/e$ focal waist radius of $w_e = 58$ nm. Consecutive measurements scatter between $w_e = 50$ nm and $w_e = 90$ nm, from which we infer $w_e = (70 \pm 20)$ nm.

current is $I_\mathrm{b} = (4.2 \pm 0.5)$ pA. We measure an opening angle of (1.29 ± 0.04) mrad implying a "Rayleigh length" of $(58 \pm 12)\,\mu$m, i.e., the distance along the beam axis from the focus to the place where the beam radius is $\sqrt{2}w_\mathrm{e}$. Therefore the beam divergence over the width of the mesa structure ($25\,\mu$m) can be neglected, which facilitates a close approach of the electrons to the grating surface. In accelerator physics language the Rayleigh length of a particle beam is often referred to as the betatron function at the waist β_w [147].

Because of the continuous-wave nature of the electron beam, only a small fraction of electrons interacts with the laser pulses. The effective electron current which interacts with the laser light is given by $I_\mathrm{eff} \approx I_\mathrm{b}\tau_\mathrm{p}f_\mathrm{rep} = 10$ electrons per second. However, a standard SEM provides a well-controlled electron beam with a sub-100 nm beam waist that can be positioned with nm-accuracy. The stability of the electron beam position is better than ∼20 nm and mostly limited by oscillating stray magnetic fields with a large component originating from the turbomolecular pump (Figure 4.9). Moreover, the SEM provides the possibility to scan the electron beam and image its position via a secondary electron detector. This excellent beam control together with the near unity detection efficiency of single electrons at energies around 30 keV outweigh the low expected count rate in this proof-of-concept experiment.

4.1.6 Vacuum system

The vacuum chamber has a base flange size DN 350 CF and is shown in Figure 4.9. The vacuum pump system consists of a backing pump (Edwards RV3 rotary vane pump) creating a fore-vacuum of $\sim 5 \cdot 10^{-3}$ mbar and a turbomolecular pump (Pfeiffer HiPace® 300) evacuating the chamber to $\sim 5 \cdot 10^{-7}$ mbar. The final pressure is mainly limited by the vacuum system of the electron column, which is not suited for ultra-high vacuum.

4.2 Detection scheme

In the experiment we need to measure the low expected count rate of accelerated electrons (I_eff ∼10 counts/s) on top of a background count rate of ∼50-70 counts/s. The background originates from high-energy photons emitted from the electron column, from photoelectrons liberated by those photons and from scattered electrons coming directly from the electron column or from field-emission sites at the high-voltage connectors inside the vacuum chamber. We apply a static magnetic field $\mathbf{B}_\mathrm{defl}$, which deflects the electron beam between the einzel lens and the microchannel plate detector (MCP) to separate them from photons passing through the lens, as shown in Figure 4.2 and Figure 4.10. Without the cover in front of the MCP, which blocks the high-energy photons and only leaves a small detection region open where we expect the accelerated electrons, the background count rate would be ∼600 counts/s. We assume that the majority of the remaining background signal originates from scattered electrons and photoelectrons, because it slightly decreases for increasing U_G relative to the electron energy and appears to be affected by the magnetic field $\mathbf{B}_\mathrm{defl}$.

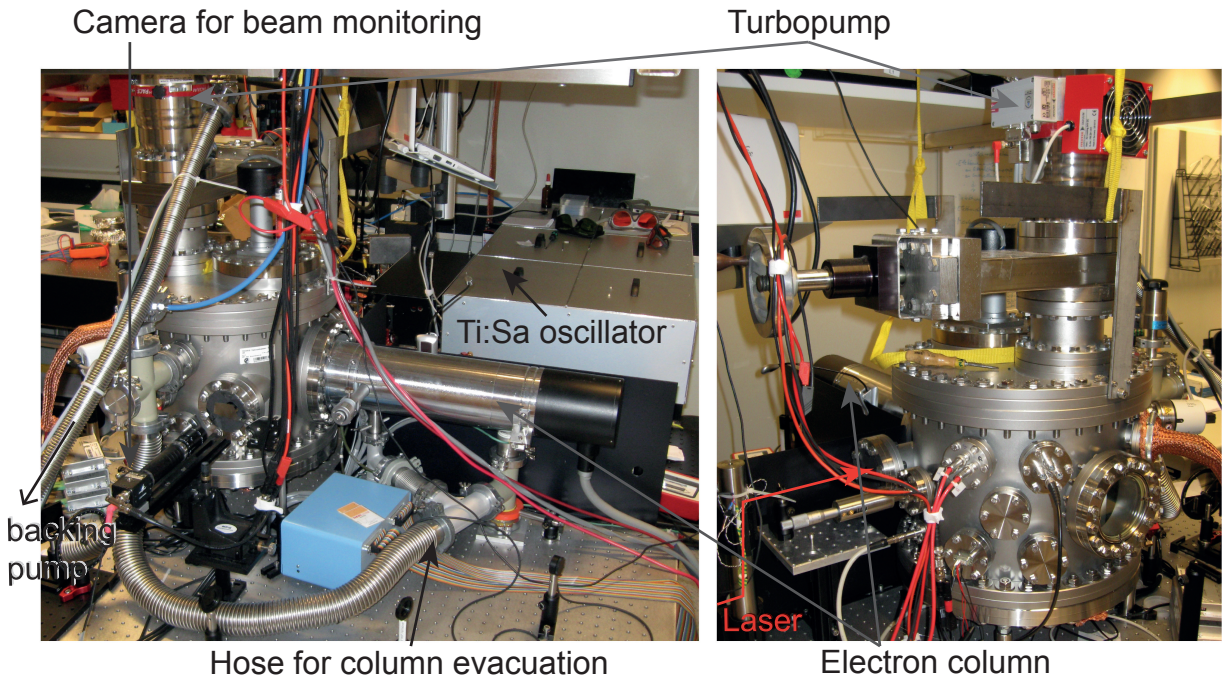

Figure 4.9: Two photographs of the experimental setup showing the vacuum chamber with the attached electron column and the turbomolecular pump. In the background the Ti:Sa oscillator can be seen. The laser pulses enter the vacuum chamber through a fused silica window.

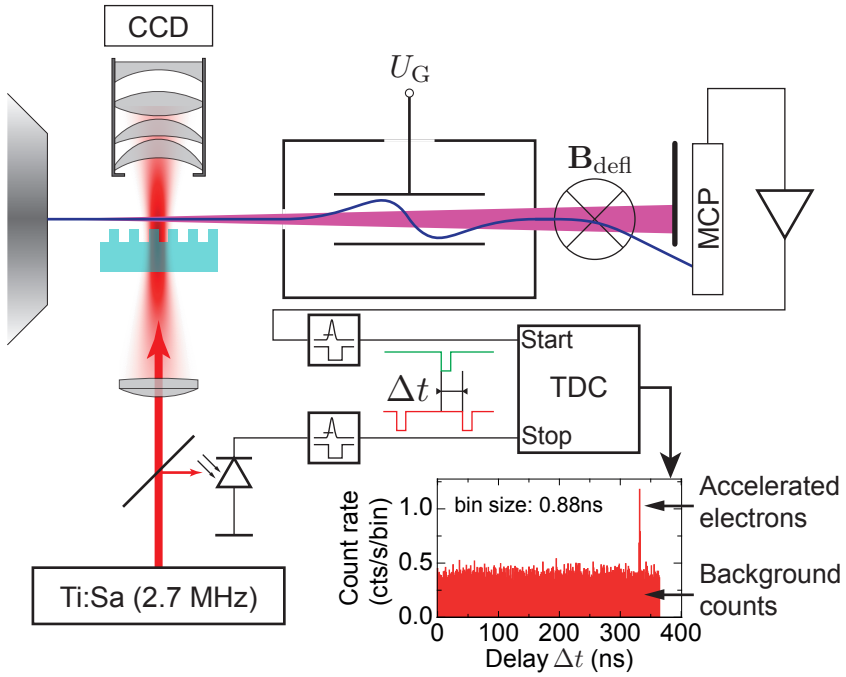

Figure 4.10: Conceptual picture of the electron acceleration detection scheme. Electrons (blue trajectory) are emitted from an electron column (left) and interact with the laser pulses (red) at the fused silica grating. A microscope objective is used to monitor the position of the laser focus. The electrons pass through the filter lens spectrometer, which blocks all unaccelerated electrons (counter voltage U_G). Accelerated electrons are detected with a microchannel plate detector (MCP). A magnetic field $\mathbf{B}_{defl}$ deflects the electrons by $\sim$10 mm to separate them from high energy photons originating inside the electron column. A time-to-digital converter (TDC) is used to measure the time delay Δt between a detector event and the following laser pulse. This way, a signal of accelerated electrons appears at a defined time delay Δt while background counts are distributed equally over all delays (inset).

The detection scheme, which represents a coincidence detection or digital lock-in technique, is depicted in Figure 4.10. We use a MCP (Photonis, Advanced Performance Long-Life^{TM}) to detect the electrons. We apply a voltage of 5 kV to the phosphor screen and ∼2-2.5 kV to the backside of the MCP. The frontside is grounded via a bias tee (Picosecond 5530B). The detector counts from the bias tee's AC port are amplified (Miteq AM-1299) and fed into a discriminator (LeCroy Model 821). Separately, an avalanche photodiode measures the arrival time of the laser pulses. A time-to-digital converter (Surface Concept SC-TDC-1000/02 D) measures the time difference between a detector count (start) and the following laser pulse (stop). The signal of accelerated electrons is directly correlated with the laser pulses and hence appears at a fixed time delay in the histogram, which includes delays from 0 to $1/f_{\mathrm{rep}} = 360$ ns. Background counts are uncorrelated with the laser pulses and are hence distributed equally in time.

Figure 4.11 (a) illustrates the basic features of such histograms and the evaluation of the signal-to-noise ratio (SNR). The interesting region of the histogram contains the time delays in which the signal of accelerated electrons is located. This region includes N_{CTR} counts of accelerated electrons on top of $N_{\mathrm{BG}} \pm \sqrt{N_{\mathrm{BG}}}$ background counts. If the histogram is recorded within a measuring time T, the noise level within the peak position is given by $\sqrt{N_{\mathrm{BG}}/T}$ and the SNR is $N_{\mathrm{CTR}}/\sqrt{N_{\mathrm{BG}}}$.

In order to test this detection scheme, we generated a fake signal by focusing frequency-doubled laser pulses onto the MCP detector. The laser pulses had to be frequency-doubled, because the detection efficiency of the MCP detector decreases exponentially for radiation with wavelength longer than ∼150 nm [148]. For example, the histogram in Figure 4.11 (b) shows a fake signal with a count rate of 0.9 cts/s.

In Figure 4.11 (c) we show a histogram containing a signal of accelerated electrons measured at a spectrometer voltage of $U_{\mathrm{G}} = 28380$ V and an initial electron energy spectrum centered around $U_{\mathrm{G}}^0 = 28300$ V. Hence, the detected N_{CTR}=160 electrons gain more than $e(U_{\mathrm{G}} - U_{\mathrm{G}}^0) = 80$ eV in energy. We measure a noise level of $1.2/\sqrt{\mathrm{s}}$ within the time delay window where the signal is located and a SNR of 21. Figure 4.11 (d) shows a histogram including $N_{\mathrm{CTR}} = 31$ electrons that are accelerated beyond 250 eV ($U_{\mathrm{G}} = 28550$ V and $U_{\mathrm{G}}^0 = 28300$ V). The signal extends over 4 bins. We measure a noise level of $\sim 1/\sqrt{\mathrm{s}}$ and a SNR of 3.6.

With this detection scheme at hand, we are capable of measuring the low expected count rate of accelerated electrons despite the relatively large background. For example, assuming a noise level of $1/\sqrt{\mathrm{s}}$ we are able to detect a signal of accelerated electrons of ∼1 cts/s with a SNR of 5 after a measuring time of ∼25 s.

4.3 Results

We first recapitulate the important experimental parameters, which have been discussed in the previous chapter. We focus $\lambda = 787$ nm laser pulses with a repetition rate of $f_{\mathrm{rep}} = 2.7$ MHz onto a fused silica grating with grating period $\lambda_{\mathrm{p}} = 750$ nm and hence exploit the third spatial harmonic to synchronously accelerate 27.9 keV electrons. The

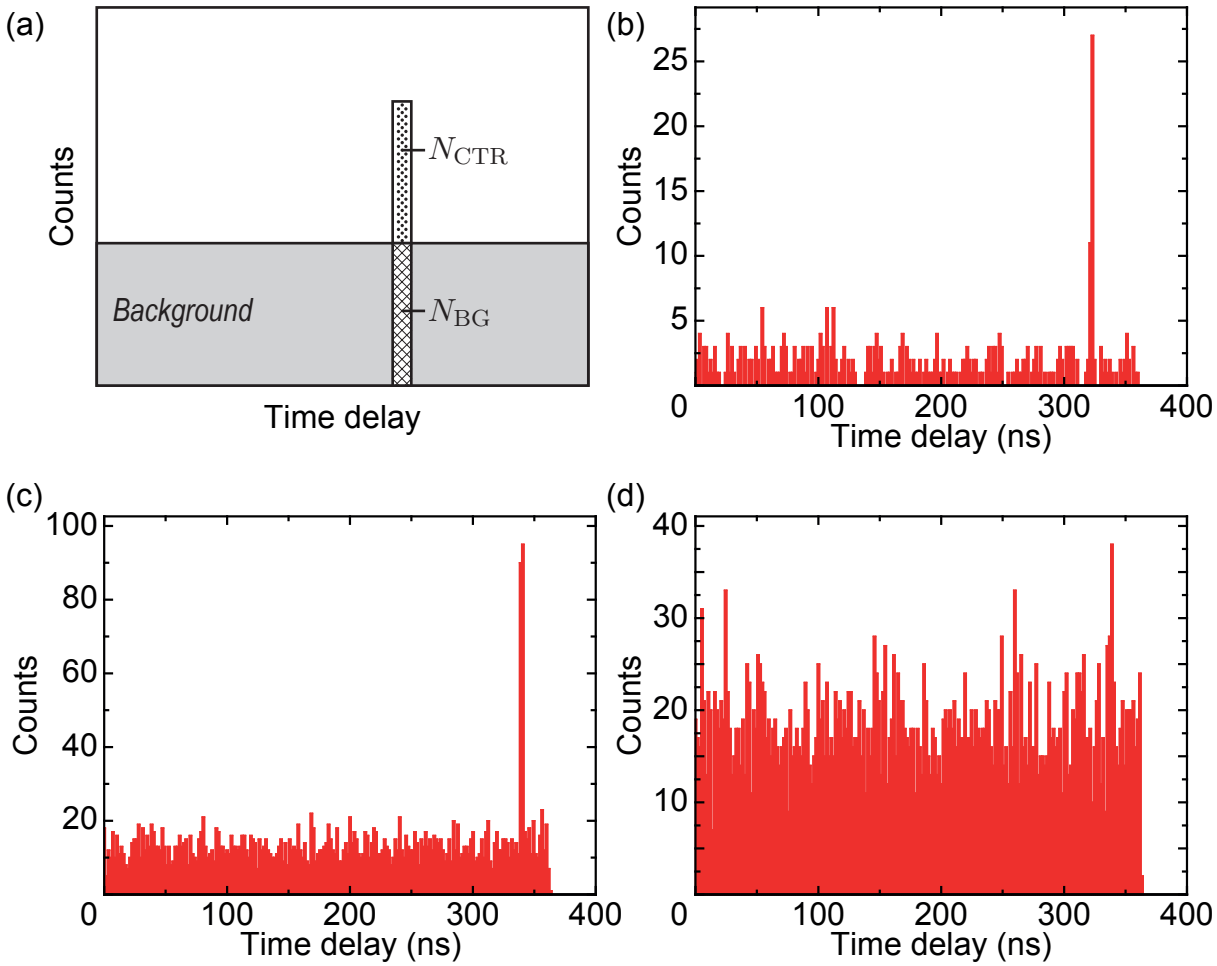

Figure 4.11: (a), Sketch of a histogram with background signal (grey shaded area), correlated signal with N_{CTR} counts and background signal at the peak position with N_{BG} counts. For a histogram recorded within a time T, the noise level at the peak position is given by $\sqrt{N_{BG}/T}$ and the signal-to-noise ratio (SNR) is $N_{CTR}/\sqrt{N_{BG}}$. (b), This histogram, which includes counts from 0 to $1/f_{rep} = 360\,\text{ns}$, shows the correlated signal with a count rate of 0.9 cts/s originating from frequency-doubled laser pulses impacting on the MCP. This measurement has been performed to test the measurement scheme. (c), This histogram shows a signal of accelerated electrons gaining more than 80 eV in kinetic energy. It is located around a time delay of 340 ns and has been recorded within $T = 40\,\text{s}$. The bin size is 1.8 ns. Within the peak, which extends over 4 bins, we measure $N_{CTR} = 160$ counts and $N_{BG} = 60$ counts, yielding a noise level of $1.2/\sqrt{\text{s}}$ and a SNR of 21. (d), This histogram with a recording time of $T = 80\,\text{s}$ includes a peak containing $N_{CTR} = 31$ counts of electrons that have gained more than 250 eV in energy. We measure $N_{BG} = 74$ counts, implying a noise level of $1.0/\sqrt{\text{s}}$ and a SNR of 3.6. See text for more details.

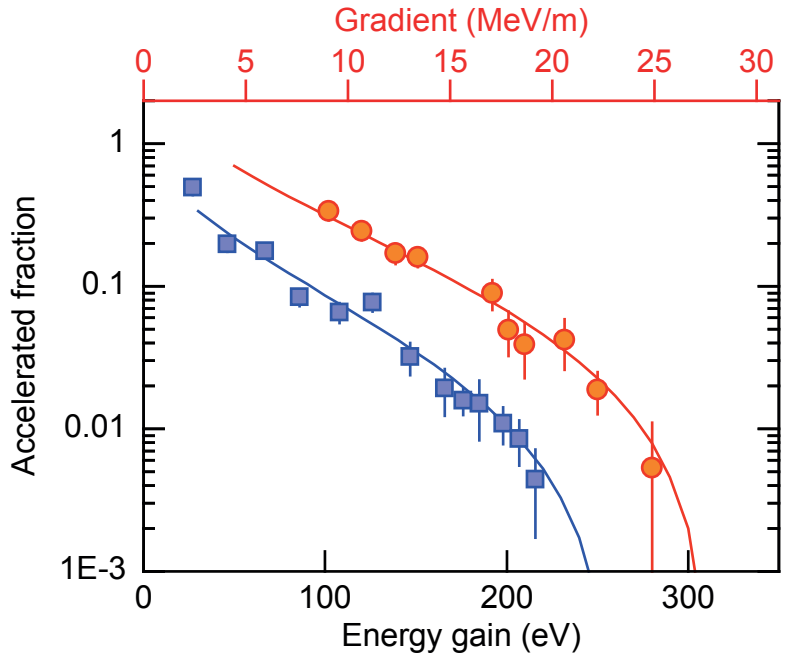

Figure 4.12: Measurement of the accelerated fraction as a function of energy gain (bottom axis) and acceleration gradient (top axis) for two different laser peak electric fields ($E_\mathrm{p} = 2.85\,\mathrm{GV/m}$ (orange circles), $E_\mathrm{p} = 2.36\,\mathrm{GV/m}$ (blue squares)). We measure a maximum energy gain of 280 eV corresponding to a maximum acceleration gradient of 25 MeV/m. The curves represent simulation results, which were obtained according to Equation 3.15 for $z_0 = 120\,\mathrm{nm}$ and $w_\mathrm{e} = 77\,\mathrm{nm}$. The overall amplitude of the simulated values has been scaled to fit the experimental data. The penultimate orange data point at an energy gain of 250 eV corresponds to the histogram shown in Figure 4.11 (d)

laser pulse duration is $\tau_\mathrm{p} = 110\,\mathrm{fs}$ and the focal waist radius is $w_\mathrm{l} = 9\,\mu\mathrm{m}$.

In Figure 4.12 we compare measurements of the accelerated fraction, defined in Equation 3.13, as a function of the acceleration gradient for two different laser peak electric fields of $E_\mathrm{p} = 2.85\,\mathrm{GV/m}$ ($P = 450\,\mathrm{mW}$, $I_\mathrm{p} = 2.2 \cdot 10^{12}\,\mathrm{W/cm^2}$, $F_\mathrm{p} = 0.13\,\mathrm{J/cm^2}$) and $E_\mathrm{p} = 2.36\,\mathrm{GV/m}$ ($P = 300\,\mathrm{mW}$, $I_\mathrm{p} = 1.5 \cdot 10^{12}\,\mathrm{W/cm^2}$, $F_\mathrm{p} = 0.09\,\mathrm{J/cm^2}$) with simulation results. We observe a maximum measured energy gain of $\Delta E = 280\,\mathrm{eV}$. It corresponds to a maximum acceleration gradient of $G_\mathrm{max} = \Delta E/(\sqrt{\pi} w_\mathrm{int}) = 25\,\mathrm{MeV/m}$, with $w_\mathrm{int} = 6.3\,\mu\mathrm{m}$. This is already comparable with state-of-the-art RF linacs. The simulated curves of the accelerated fraction assume a distance of the electron beam center from the grating surface of $z_0 = (120 \pm 10)\,\mathrm{nm}$ and an electron beam waist of $w_\mathrm{e} = 77\,\mathrm{nm}$. We deduce from an excitation efficiency simulation, discussed in Section 3.3, that the maximum acceleration occurs for electrons that pass the grating at a distance of $\sim$50 nm due to the finite beam width. We infer this to be the experimental limit for the minimum distance between the electrons and the grating. We assume that beam clipping together with residual surface charging prevent a closer approach in the current setup.

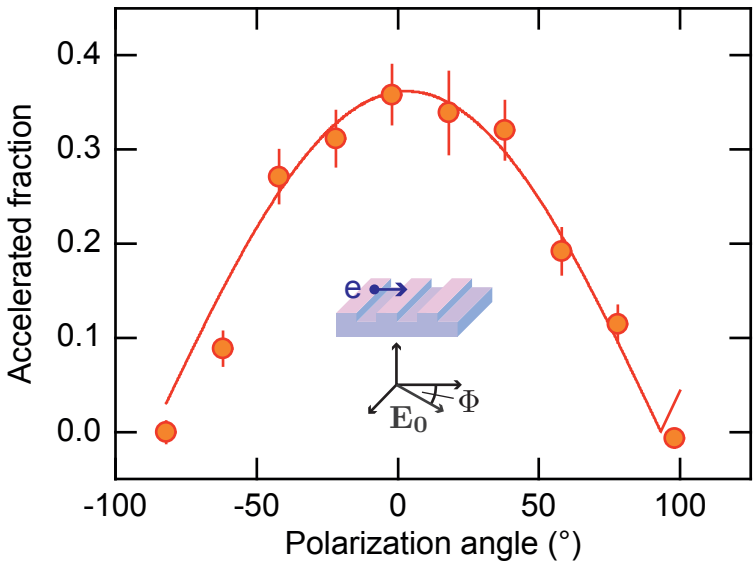

Figure 4.13: Accelerated fraction of electrons as a function of the laser polarization angle Φ relative to the electrons' trajectory. $\Phi = 0°$ means that the laser polarization is parallel to the electrons' momentum, $\Phi = 90°$ that it is perpendicular to it (see inset). The data agrees well with the expected cosine behavior (orange fit curve) and proves that the electrons are directly accelerated by the light field. The negative value of $(-7 \pm 9) \cdot 10^{-3}$ at $\Phi = 100°$ indicates that for this measurement the count rate at the expected peak position was below the background count rate (Figure 4.11).

The electrons are only accelerated by the electric field component that is parallel to their momentum as can be seen from the dependence of the acceleration on the laser polarization angle Φ, in Figure 4.13. This strongly supports acceleration with the electromagnetic light *field* and clearly rules out the much weaker intensity-dependent but polarization-independent ponderomotive acceleration [23]. The ponderomotive force is given by

$$F_{\mathrm{pond}} = -\frac{e^2}{4m_{\mathrm{e}}\omega^2}\nabla\mathbf{E^2}, \tag{4.1}$$

with the laser angular frequency ω. Assuming a laser electric field as seen from the electron's moving frame of $E(x) = E_{\mathrm{p}}\exp(-(x/w_{\mathrm{int}})^2)$ (Equation 3.3), we obtain

$$F_{\mathrm{pond}}(x) = \frac{e^2E_{\mathrm{p}}^2}{m_{\mathrm{e}}\omega^2w_{\mathrm{int}}^2}xe^{-2(x/w_{\mathrm{int}})^2}. \tag{4.2}$$

We compute a maximum ponderomotive acceleration gradient of $G_{\mathrm{max}}^{\mathrm{pond}} = F_{\mathrm{pond}}|_{x=w_{\mathrm{int}}/2} = 12\,\mathrm{keV/m}$, assuming $w_{\mathrm{int}} = 6.3\,\mu\mathrm{m}$. This would be more than three orders of magnitude smaller than the observed 25 MeV/m.

The sinusoidal fit in Figure 4.13 gives a limit on a possible angular misalignment of the grating with respect to the electron beam of $\Phi_0 = (3.2 \pm 5.3)^\circ$. This angular misalignment implies an offset between the experimentally measured electron energy and the energy used in the simulations, where we set $\Phi_0 = 0$, in the following way. The component of the electron velocity that is parallel to the grating vector has to satisfy the synchronicity condition $\beta\cos(\Phi_0) = \lambda_{\mathrm{p}}/(n\lambda)$ (Equation 2.5). However, in the experiment we measure the total kinetic energy related to an electron velocity β, which is a factor of $1/\cos\Phi_0$ larger than the design velocity $\lambda_{\mathrm{p}}/(n\lambda)$. We calculate the resulting shift of the measured kinetic energy to be $-100^{+100}_{-570}\,\mathrm{eV}$.

The measurement of the accelerated fraction as a function of the relative distance z_0 between the electron beam and the grating surface is shown in Figure 4.14. It confirms that acceleration is only possible in close vicinity of the grating surface, where the evanescent field is pronounced. The data can be fitted with a Gaussian of width $(119 \pm 11)\,\mathrm{nm}$. From simulations of the accelerated fraction (Equation 3.15) for varying z_0 and for the experimental parameters ($E_{\mathrm{p}} = 2.36\,\mathrm{GV/m}$ and $\Delta E = 30\,\mathrm{eV}$) we also obtain a Gaussian dependence. The measured width of the Gaussian can be reproduced with simulation results for $w_{\mathrm{e}} = (77 \pm 8)\,\mathrm{nm}$, in good agreement with the experimental result $w_{\mathrm{e}} = (70 \pm 20)\,\mathrm{nm}$ (Figure 4.8).

In Figure 4.15 we compare a measurement of the maximum acceleration gradient for varying electron energy with simulation results. Here, we observe the largest acceleration gradient for an initial electron energy of $\sim$27.7 keV. The acceleration efficiency decreases for larger and smaller electron energies. Hence, this proves that for efficient acceleration the synchronicity condition has to be fulfilled. The simulation results correspond to electrons passing the grating at $z_0 = 60\,\mathrm{nm}$ and show good agreement with the experiment.

All experimental values in Figure 4.15 have been shifted by $-340\,\mathrm{eV}$ to match the simulation results. This shift can be attributed to $-260\,\mathrm{eV}$ due to field penetration inside

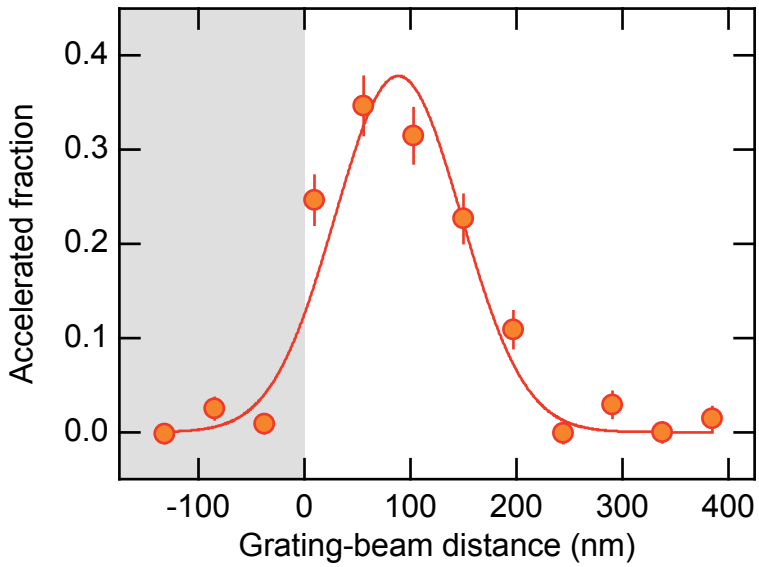

Figure 4.14: Measurement of the accelerated fraction versus the distance between the grating surface (shaded area) and the electron beam center, with Gaussian fit (solid curve). This measurement has been performed with a laser peak electric field of $E_\mathrm{p} = 2.36\,\mathrm{GV/m}$ and at a fixed energy gain $\Delta E = 30\,\mathrm{eV}$. Due to the finite width w_e of the electron beam we measure a few accelerated electrons even when the beam center hits the grating surface. The absolute position ($z_0 = 0$) of the data relative to the grating surface has been determined from simulations according to Equation 3.15.

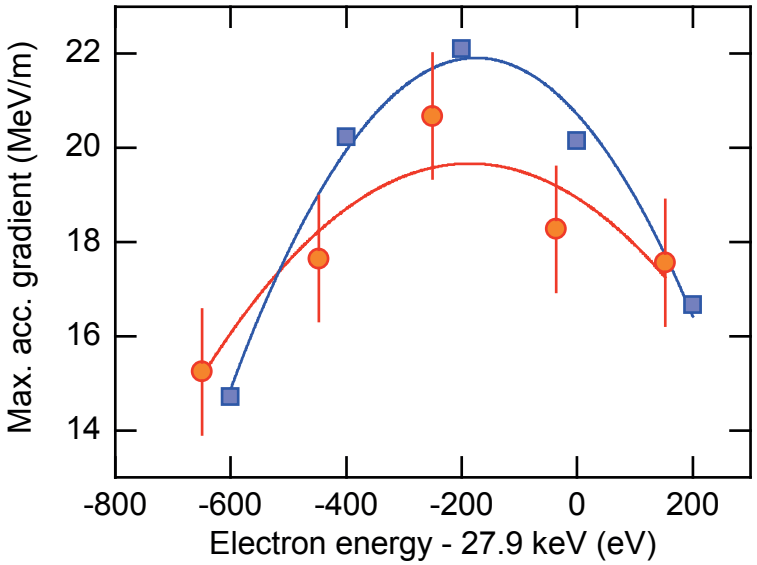

Figure 4.15: Measurement (orange circles) and simulation (blue squares) of the maximum acceleration gradient as a function of the initial electron energy, with quadratic fits as guides to the eye (solid lines). The largest acceleration gradient occurs 200 eV below the synchronous energy (27.9 keV) because the acceleration at the rising edge of the Gaussian-shaped interaction, with width w_{int}, ensures synchronicity during the presence of the laser peak electric field. See text for more details.

the filter lens spectrometer and -100^{+100}_{-570} eV due to angular misalignment of the grating, as discussed above. In order to reduce the measuring time and increase the statistics we define the maximum acceleration gradient in this measurement at a larger accelerated fraction than in Figure 4.12 (a) ($4 \cdot 10^{-2}$ vs. $5 \cdot 10^{-3}$), which explains why we measure a maximum gradient of ∼20 MeV/m instead of 25 MeV/m.

These measurements confirm the dielectric laser acceleration of non-relativistic electrons via the inverse Smith-Purcell effect at a fused silica grating. The measured maximum acceleration gradient of 25 MeV/m is already comparable with state-of-the-art RF accelerators. This also represents the first demonstration of the inverse Smith-Purcell effect in the optical regime. In the next chapter we will discuss the importance of non-relativistic DLA structures in envisioned large-scale optical accelerators, as well as their application in future light sources.

Chapter 5

Design and application of future large-scale optical accelerators

In this chapter we present an outlook on the application of DLA structures. We first derive an estimate on the maximum attainable peak current of optical accelerators limited by the space charge effect. We then examine the design of a large-scale DLA, including the injection scheme, size and power consumption, based on our simulation results. Finally, we discuss the application of novel acceleration structures in future light sources, such as free electron lasers. We have reported a similar discussion in [126, 139].

5.1 Space charge forces

The transverse dimension of the particle beam inside an accelerator has to be smaller than the size of the accelerating structures, which is directly connected to the driving wavelength. While conventional RF accelerators can support beams with diameters on the cm-scale, optical linear accelerator will provide particle beams with sub-micron diameters. Hence, space charge forces limit the maximum bunch charge of the particle ensemble especially in DLAs, because this repulsive force is inversely proportional to the transverse dimension of the beam and therefore more than four orders of magnitude larger in optical linacs as compared to RF accelerators. Elliptical or sheet beams with a large transverse dimension perpendicularly to the vacuum channel have been suggested to minimize defocusing due to the space charge effect [11].

To estimate the maximum bunch charge of a beam with a circular profile we use the paraxial ray equation [30]. It describes the beam envelope radius r_m via

$$\begin{aligned} r_\mathrm{m}'' + \frac{\gamma' r_\mathrm{m}'}{\beta^2\gamma} + \frac{\gamma'' r_\mathrm{m}}{2\beta^2\gamma} + \left(\frac{qB}{2mc\beta\gamma}\right)^2 r_\mathrm{m} \\ - \left(\frac{p_\theta}{mc\beta\gamma}\right)^2 \frac{1}{r_\mathrm{m}^3} - \frac{\tilde{\epsilon}_\mathrm{n}}{\beta^2\gamma^2 r_\mathrm{m}^3} - \frac{K}{r_\mathrm{m}} = 0. \end{aligned} \tag{5.1}$$

Here B is an axial (static) magnetic field, p_θ the canonical angular momentum of the particles, $\tilde{\epsilon}_\mathrm{n}$ the normalized emittance and $K = 2I/(I_0\beta^3\gamma^3)$ the generalized perveance, with the Budker or Alfvén current for electrons: $I_0 = 17000\,\mathrm{A}$. The perveance is a measure for the space charge effect [30, 149]. The radial ray equation describes the beam dynamics and includes acceleration in a longitudinal electric field with $\gamma' = eE_\parallel/(mc^2)$ (2^nd term), focusing in a radial electric field with $\gamma'' = 2eE_\perp/(mc^2 r_\mathrm{m})$ (3^rd term), focusing in an axial magnetic field (4^th term), defocusing due to angular momentum and normalized emittance (5^th and 6^th term) as well as defocusing due to space charge (last term).

To estimate the maximum bunch charge in an optical accelerator we assume $B = p_\theta = 0$, a space-charge-limited beam ($\tilde{\epsilon}_\mathrm{n} \ll K\beta^2\gamma^2 r_\mathrm{m}^2$) and focusing in the radial electric field provided by the optical accelerator. As discussed in Section 2.1, the focusing and accelerating force components, F_z and F_x, respectively, are out of phase according to Equation 2.14:

$$\mathbf{F_r} = q \begin{pmatrix} icB_y/(\beta\gamma) \\ 0 \\ -cB_y/(\beta\gamma^2) \end{pmatrix}. \tag{5.2}$$

Therefore $\mathrm{Re}\,(F_x) = 0$ for $|\mathrm{Re}\,(F_z)| = qc\,|B_y|\,/(\beta\gamma^2)$. Hence, for a focusing structure and a microbunched electron beam with sub-laser-cycle microbunch duration we can neglect acceleration, $\gamma' = 0$. Therefore we obtain

$$r_\mathrm{m}'' + \frac{\gamma'' r_\mathrm{m}}{2\beta^2\gamma} - \frac{K}{r_\mathrm{m}} = 0. \tag{5.3}$$

The maximum acceleration gradient of the structure is defined as

$$G = \frac{dE_\mathrm{kin}}{dx} = |F_x| = \frac{qc}{\beta\gamma}\,|B_y|\,. \tag{5.4}$$

The transverse focusing force is equivalent to a radial electric field with amplitude $E_\perp = |F_z|/q = G/(q\gamma)$, thus

$$\gamma'' = \frac{2qE_\perp}{mc^2 r_\mathrm{m}} = \frac{2G}{mc^2 r_\mathrm{m}\gamma}. \tag{5.5}$$

We request that in equilibrium this transverse focusing force balances the outward radial acceleration due to the space charge, i.e., $r_\mathrm{m}'' = 0$. This yields the maximum beam current

$$I_\mathrm{b} = I_0 \frac{G\beta\gamma r_\mathrm{m}}{2mc^2}. \tag{5.6}$$

We calculate I_b for non-relativistic and relativistic electrons inside double grating structures based on the simulation results presented in Section 3.2. We assume an electron beam with radius r_m propagating on-axis inside the structure. The acceleration gradient at the envelope of the beam is given by (Equation 3.10)

$$G = F_x|_{z=r_\mathrm{m}/2} = \frac{C_\mathrm{s}}{\beta\gamma}\cosh\left(\frac{k_0 r_\mathrm{m}}{2\beta\gamma}\right). \tag{5.7}$$

In Table 5.1 we show the maximum peak beam currents for a 30 keV electron beam, with $r_\mathrm{m} = 50\,\mathrm{nm}$, inside the double grating structure (Figure 3.5 (a) on page 37), which is excited by a single laser, for various laser peak electric fields E_p. For example, for $E_\mathrm{p} = 10\,\mathrm{GV/m}$ this structure can sustain a peak beam current of $I_\mathrm{b} = 90\,\mathrm{mA}$. We further calculate I_b for a 1 MeV electron beam, with $r_\mathrm{m} = 300\,\mathrm{nm}$, inside the symmetrically pumped structure depicted in Figure 3.5(d). Here, the attainable peak currents are more than two orders of magnitude larger than in the non-relativistic case and a laser peak field $E_\mathrm{p} = 10\,\mathrm{GV/m}$ implies $I_\mathrm{b} = 14\,\mathrm{A}$.

The maximum bunch charge that can be kept inside the accelerator without beam expansion due to space charge forces is

$$Q_\mathrm{b} = I_\mathrm{b}\tau_\mathrm{b}, \tag{5.8}$$

with the bunch duration τ_b. The bunch duration inside the accelerator is ideally smaller than the optical cycle $\tau_\mathrm{cycle} = \lambda/c$, so that the bunch experiences a homogeneous force. Assuming $\tau_\mathrm{b} = 0.1\tau_\mathrm{cycle}$ we obtain for the 30 keV electrons and $E_\mathrm{p} = 10\,\mathrm{GV/m}$ a maximum bunch charge of 24 aC, corresponding to 150 electrons. For the 1 MeV electrons and $E_\mathrm{p} = 10\,\mathrm{GV/m}$ the structure can support 3.7 fC.

The values given in Table 5.1 correspond to a laser wavelength of 800 nm. As the space charge force is inversely proportional to the beam radius, a laser wavelength of 2 μm allows 2.5 times larger peak currents assuming that the grating dimensions and electron beam radius are scaled up in size accordingly. Moreover, we assume that the refractive index of the dielectric material is constant for all wavelengths, which assures the same excitation efficiency of the spatial harmonics. Similarly, a driving wavelength of 5 μm allows a 6.3 times larger peak current. This implies that the bunch charge Q_b scales with λ^2, assuming that τ_b is proportional to τ_cycle.

Note that in the derivation of the maximum current I_b we assume that the focusing force of the grating structure is used to counteract the defocusing force due to space charge, i.e., we choose a start phase of the microbunch for which the focusing force is maximum and acceleration is zero. For a useful accelerator structure transversal confinement in conjunction with longitudinal bunching and acceleration is required. As discussed in Section 2.1, this can be achieved, e.g., with alternating phase focusing [42, 128, 129] or with biharmonic structures [76]. Hence, the given numbers are estimates and might slightly vary in a realistic setup.

5.2 Design of a dielectric laser accelerator

Here, we will discuss important features that have to be taken into account for the design of a DLA. The beam parameters for an optical accelerator are fundamentally different from the ones in today's RF linacs. The much smaller beam size implies that DLAs support lower bunch charges limited by the space charge effect and wakefield radiation losses [68]. Furthermore, to couple electrons into these microstructures an ultralow emittance and

E_p (GV/m)	$E_\mathrm{kin} = 29\,\mathrm{keV}$, $r_\mathrm{m} = 50\,\mathrm{nm}$ (Figure 3.5(a))	$E_\mathrm{kin} = 957\,\mathrm{keV}$, $r_\mathrm{m} = 300\,\mathrm{nm}$ (Figure 3.5(d))
1	9 mA	1 A
7	62 mA	10 A
10	89 mA	14 A

Table 5.1: Maximum peak beam current I_b for a 29 keV electron beam ($r_\mathrm{m} = 50\,\mathrm{nm}$) inside the grating geometry shown in Figure 3.5(a), and for a 957 keV electron beam ($r_\mathrm{m} = 300\,\mathrm{nm}$) inside the grating geometry depicted in Figure 3.5(d) for three different peak electric fields of the laser. We assumed an acceleration gradient at the center of the vacuum channel of $G = 0.027 \cdot eE_\mathrm{p}$ for the non-relativistic case and $G = 0.11 \cdot eE_\mathrm{p}$ for the relativistic case. The laser wavelength is 800 nm.

high brightness electron source is required [11]. The larger acceleration gradient implies a smaller overall size. And finally, laser technology will enable the possibility to operate at very high repetition rates in the megahertz to gigahertz range.

In Figure 5.1 we show a sketch of the envisioned design of a DLA. It consists of a laser-triggered DC electron gun, a non-relativistic and a relativistic DLA section, as well as intermediate focusing sections. A common laser source, amplified in various sections in a phase-stable manner, can be used to drive the accelerator. This greatly facilitates the synchronization and optical phase-stability between the different acceleration and focusing stages, which is essential for proper functioning, and nowadays routinely possible. The non-

Figure 5.1 *(following page)*: Sketch of the envisioned design of an all-optical accelerator consisting of an electron gun (A), non-relativistic (B) and relativistic (C) DLA sections. Grating-based focusing structures (F) are inserted as intermediate sections to recollimate the electron beam. All parts are driven by a common laser source, for ease of operation fiber-based. The non-relativistic section comprises grating structures with a tapered grating period to assure synchronicity with the accelerating electrons using the third (B1), second (B2) and first (B3) spatial harmonic. We expect the electrons to enter the relativistic section at an energy of ∼1 MeV. The embedded graph illustrates the increasing acceleration gradient as the electrons gain energy inside the DLA. Assuming, for example, a minimum fabricable grating period of $\lambda_\mathrm{p} = 650\,\mathrm{nm}$ and a driving wavelength of 800 nm, the injection energy is 20 keV ($\beta = \lambda_\mathrm{p}/(n\lambda) = 650/(3 \cdot 800) = 0.27$) for acceleration with the third spatial harmonic ($n = 3$). At 50 keV ($\beta = 650/(2 \cdot 800) = 0.41$) the electrons can be accelerated with the second spatial harmonic and at 360 keV ($\beta = 650/800 = 0.81$) the first spatial harmonic can be exploited. Inside the non-relativistic section the channel width can gradually increase because of the increasing decay constant δ of the accelerating fields with the electrons' velocity. Not to scale.

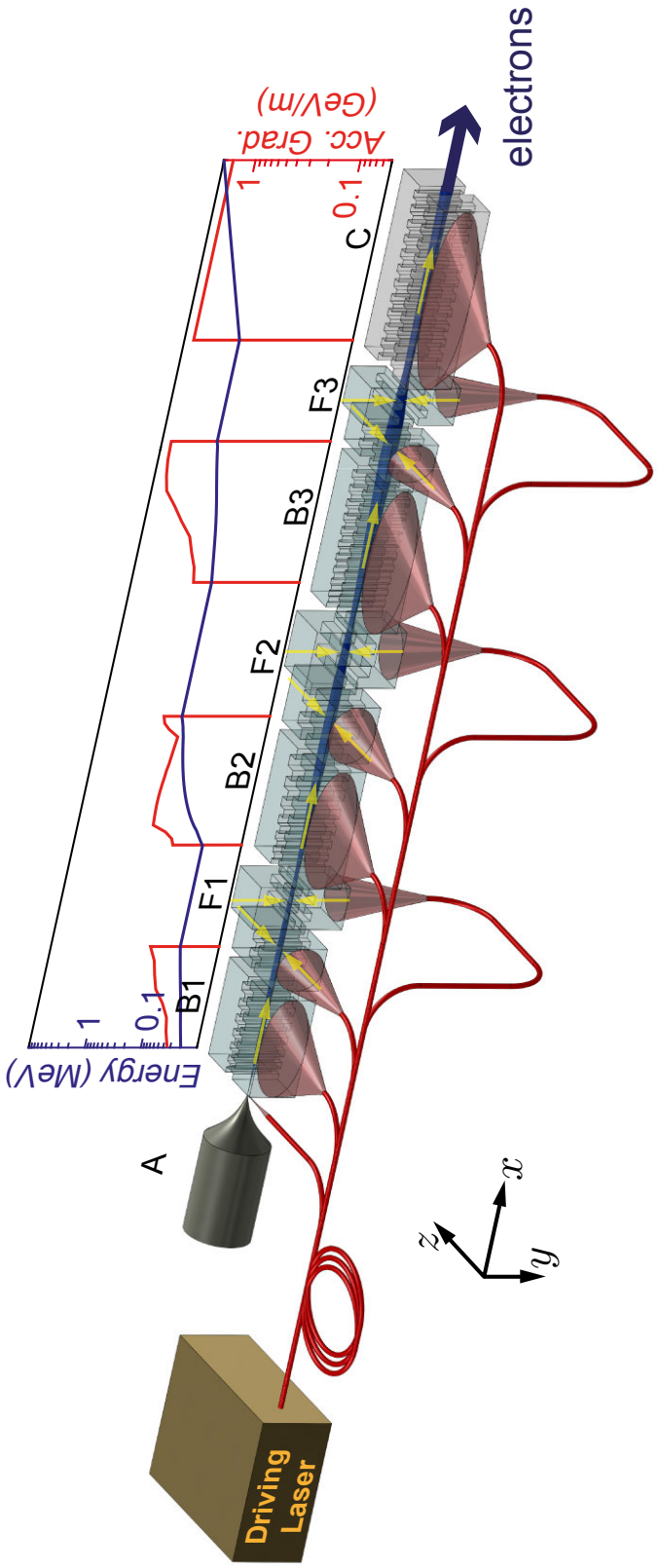
electrons
Acc. Grad. (GeV/m)
1
0.1
C
F3
B3
F2
B2
F1
B1
Energy (MeV)
1
0.1
A
Driving Laser
x
z
y

relativistic part (up to ∼1 MeV) may consist of subsections of tapered dielectric gratings, in which an adaptively increasing grating period accounts for the change in electron velocity. For this part, either single or double grating structures may be used. While single gratings offer a simpler setup, the evanescent nature of the acceleration can lead to beam distortion. Double grating structures have the advantage of larger efficiency and a symmetric profile of the accelerating fields [130]. Exploiting different spatial harmonics allows to overcome fabrication limitations on the grating period by starting, for example, with 20 keV electrons at the point of injection. After using the third spatial harmonic to accelerate up to ∼50 keV, one may switch to the more efficient second harmonic and at ∼400 keV to the first harmonic to accelerate further.

In our envisioned design we use a set of two crossed double grating structures to recollimate the beam at intermediate points. We note that grating-based focusing structures with tilted grating grooves that can focus and deflect electrons transversely, in the y-direction, have been proposed [80]. These focusing structures rely on a variation of the laser electric field amplitude along the y-axis. Because we assume an electron beam with a radial profile with sub-micron transverse dimensions and shaping of the laser focus on a scale well below the wavelength is impossible, focusing with these planar structures is not feasible. However, if the DLA uses elliptical electron beams with sub-micron dimensions in the z-direction and much larger ∼10 μm along the y-direction, it may be feasible to use the proposed planar focusing structures.

5.2.1 Bunch charge

In the preceding discussion in Chapter 2 we have calculated the acceleration gradient directly from the simulated amplitude of the synchronous spatial harmonic, which corresponds to the maximum acceleration gradient that can, strictly speaking, only be reached for a single electron per bunch. If beam loading is taken into account, wakefields related to the backaction of the electrons on the accelerating mode reduce the acceleration gradient. Optimum efficiency is achieved when the loaded gradient equals half the maximum gradient, limiting the number of electrons that can be loaded into the structure [68]. Plettner *et al.* have calculated a wakefield-limited bunch charge of $Q_\mathrm{b} = 0.2\,\mathrm{pC}$ ($\sim 9 \cdot 10^5$ electrons) for a double grating structure excited by 800 nm laser pulses with a duration of 100 fs [68]. That work assumes a bunch duration of $\tau_\mathrm{b} = \tau_\mathrm{cycle}/2$, i.e., only one bunch per laser pulse is accelerated. The corresponding peak current is given by $Q_\mathrm{b}/\tau_\mathrm{b} \sim 100\,\mathrm{A}$. This peak current cannot be reached with 1 MeV electrons ($\gamma \sim 3$) due to the space charge effect (Table 5.1). However, as the space-charge-limited peak current I_b scales linearly with γ, increasing the injection energy to 15 MeV ($\gamma \sim 30$) will increase I_b by one order of magnitude and therefore enable the wakefield-limited bunch charge of 0.2 pC.

For single- or few-cycle laser pulses it is not feasible to accelerate more than one bunch per laser pulse, because the pulse envelope changes too quickly and consecutive microbunches would experience largely different acceleration gradients. But for slightly larger τ_p it may also be possible to accelerate a bunch train with n_b microbunches with

a microbunch duration τ_{mb} to increase the average beam current. For example, for $\tau_{\mathrm{p}} = 100\,\mathrm{fs}$ and $\lambda = 800\,\mathrm{nm}$ an electron beam may consists of a bunch train with $n_{\mathrm{b}} = 10$ microbunches with $\tau_{\mathrm{mb}} = 1\,\mathrm{fs}$. Assuming a microbunch charge of $Q_{\mathrm{mb}} = 0.2\,\mathrm{pC}$ and a train repetition rate of $f_{\mathrm{rep}} = 1\,\mathrm{MHz}$, the average beam current is $n_{\mathrm{b}} Q_{\mathrm{mb}} f_{\mathrm{rep}} = 2\,\mu\mathrm{A}$.

5.2.2 Injection of electrons

It is impossible to synchronously accelerate electrons from rest with evanescent fields, as discussed in Section 2.1. Hence an important question for the design of a DLA is the electron energy at which the beam is fed into the dielectric structure. The first step of acceleration up to this injection energy has to be provided either by a static electric field or by an RF gun, in which electrons can be accelerated to relativistic energies within one half-cycle of the RF fields [150]. Note that an optical gun design similar to an RF gun is impossible, because the energy gain per cycle is much lower in a DLA ($\sim 1\,\mathrm{GV/m} \cdot 1\,\mu\mathrm{m} = 1\,\mathrm{keV}$) than in an RF gun ($\sim 10\,\mathrm{MeV/m} \cdot 10\,\mathrm{cm} = 1\,\mathrm{MeV}$). To take full advantage of the high repetition rate we expect that the favorable design is a laser-triggered DC gun, i.e., a photocathode or nanotip-based photoelectron source in conjunction with a static acceleration section [40], which operates synchronously with the DLA laser system. The optimum injection energy has to be a trade-off between size and beam current considerations and will probably depend on the application. On the one hand, a lower injection energy will allow a more compact design, because of a shorter distance of DC acceleration where the maximum gradient is limited to $\sim 10\,\mathrm{MeV/m}$. Moreover, a smaller scale electron optics inside the injector can be used. On the other hand, a larger injection energy has the advantages of a larger dephasing length (Table 3.1), a larger space-charge-limited peak current (Table 5.1) and a stiffer electron beam.

In the envisioned design of the DLA, shown in Figure 5.1, we assume a non-relativistic injection energy and therefore require a non-relativistic DLA section. The intercompatibility of the non-relativistic DLA with the relativistic part facilitates the compact design. Moreover, the non-relativistic section has the additional advantage of preserving the emittance and bunch duration of the electron beam during the acceleration process due to the sub-micron transversal dimension of the structures and the acceleration at optical frequencies. However, we note that the non-relativistic DLA may nevertheless be rendered unnecessary, if a DC or RF injector providing relativistic electron bunches is realized. The criterion for exclusion of one or the other scheme will be the emittance and the bunch duration at the injection point.

To reach the above mentioned bunch charges and bunch durations at the point of injection, a bunch compression or emittance exchange scheme should be employed. This results in a microbunched beam, which is needed for efficient operation of the DLA. Bunch compression increases the peak current [120, 151–153], which is considerably lower during the non-relativistic acceleration section due to the space charge effect (Table 5.1). Emittance exchange converts a transversely modulated beam from a field emitter array into a longitudinally microbunched beam [33]. Instead of using a field emitter array one may

$E_{\mathrm{kin}}^{(\mathrm{i})}$ (keV)	$E_{\mathrm{p}} = 1\,\mathrm{GV/m}$	$E_{\mathrm{p}} = 10\,\mathrm{GV/m}$
20	24 mm	2.4 mm
100	14 mm	1.4 mm
300	7 mm	0.7 mm

Table 5.2: Length of the non-relativistic optical accelerator for a final energy of 1 MeV, depending on the injection energy $E_{\mathrm{kin}}^{(\mathrm{i})}$ and the laser peak field E_{p}. We assume a linearly increasing acceleration gradient as discussed in Section 3.1.1 on page 27.

also combine multiple lower charge bunches, which have been accelerated by separate, but synchronized, guns. Electron optics, known from electron microscopy, can be used to focus the bunches into the DLA.

5.2.3 Length scaling

We estimate the length of a future DLA in two steps. First, we evaluate the length for the non-relativistic part of the accelerator, which starts at an injection energy $E_{\mathrm{kin}}^{(\mathrm{i})}$ and accelerates to 1 MeV. We assume that $G(E_{\mathrm{kin}}) = eE_{\mathrm{p}}E_{\mathrm{kin}} \cdot 1.61 \cdot 10^{-7}\,\mathrm{eV}^{-1}$, which has been obtained by linearly fitting $G/(eE_{\mathrm{p}})$ exploiting the first spatial harmonic of a single grating in Figure 3.1 (b) on page 29. We note that acceleration exploiting the first spatial harmonic may not be feasible for non-relativistic electrons due to fabrication limitations on the grating period. However, even using the third spatial harmonic merely reduces the acceleration gradient by a factor of three. For simplicity we assume acceleration with the first harmonic for this rough estimate.

Although we expect a maximum acceleration gradient about twice as large for a double grating structure as compared with the single grating, we can still assume the single grating efficiency because another factor of 1/2 comes in when considering the loaded gradient [68]. The differential equation $\mathrm{d}E_{\mathrm{kin}}/\mathrm{dx} = G(E_{\mathrm{kin}})$ can be solved with $E_{\mathrm{kin}}(x) = E_{\mathrm{kin}}^{(\mathrm{i})} \exp\left(eE_{\mathrm{p}}x \cdot 1.61 \cdot 10^{-7}\,\mathrm{eV}^{-1}\right)$. Note that in this estimate we have not included the length of focusing structures that are especially needed inside the non-relativistic DLA. However, we do not expect focusing structures to increase the length by more than a factor of two.

In Table 5.2 we show the estimated length of the non-relativistic DLA for different injection energies and laser peak electric fields. For example, a non-relativistic DLA driven by a laser with $E_{\mathrm{p}} = 1\,\mathrm{GV/m}$ can accelerate 100 keV electrons up to 1 MeV on a distance of 14 mm. The length of this non-relativistic section scales inversely with E_{p}.

In a second step we calculate the length of the relativistic DLA, which starts at an injection energy of 1 MeV and accelerates to a final energy $E_{\mathrm{kin}}^{(\mathrm{f})}$ assuming a constant (loaded) acceleration gradient $G = 0.12eE_{\mathrm{p}}$, adapted from [68]. The results are shown in Table 5.3 for various final energies. For example, a 10 GeV DLA driven by a laser with $E_{\mathrm{p}} = 10\,\mathrm{GV/m}$ is expected to be less than 10 m long. The length scales linearly with

$E_{\mathrm{kin}}^{(\mathrm{f})}$	$E_{\mathrm{p}} = 1\,\mathrm{GV/m}$	$E_{\mathrm{p}} = 10\,\mathrm{GV/m}$
100 MeV	83 cm	8.3 cm
10 GeV	83 m	8.3 m
1 TeV	8.3 km	830 m

Table 5.3: Length of the relativistic optical accelerator with an injection energy of 1 MeV and a final energy $E_{\mathrm{kin}}^{(\mathrm{f})}$ using a laser with a peak field E_{p}. We assume a constant (loaded) acceleration gradient $G = 0.12eE_{\mathrm{p}}$ (also in [68]).

the final energy for relativistic electrons and inversely with the laser peak electric field. Although our simulation does not include the speed-of-light mode which is needed for this part of the accelerator, we expect that a loaded gradient of $0.2eE_{\mathrm{p}}$ to $0.3eE_{\mathrm{p}}$ is feasible. This increases the acceleration gradient and therefore the length of the DLA is reduced by a factor of two to three compared to the values given in Table 5.3.

5.2.4 Power scaling

To estimate the power consumption of a DLA, we assume a width of the laser focus $\sigma_y \sim\lambda$ perpendicular to the electron beam direction (y-coordinate in Figure 5.1). The peak laser power is defined as $P_{\mathrm{L}}^{\mathrm{p}} = \sigma_x\sigma_y E_{\mathrm{p}}^2/(2Z_0)$, with the dimension of the laser focus σ_x along the beam direction and the vacuum impedance $Z_0 = 377\,\Omega$. The average laser power is $P_{\mathrm{L}} = P_{\mathrm{L}}^{\mathrm{p}}\tau_{\mathrm{p}} f_{\mathrm{rep}}$. We further assume that electrical power can be converted into laser power with a wall-plug efficiency of 30%, which is realistic for state-of-the-art fiber laser technology [154]. The estimated electrical power consumption per unit length is shown in Table 5.4 for various laser parameters. It scales linearly with f_{rep}, τ_{p} and E_{p}^2. Because we assume the transverse focal spot size of the laser to be proportional to the driving wavelength λ, it also scales linearly with λ. We note that including the laser power needed for the focusing elements, which is neglected here, may increase the power consumption by up to 50%.

For example, a 50 GeV DLA operating with a laser peak electric field of 10 GV/m, a laser pulse duration of 100 fs, a driving wavelength of 800 nm and a repetition rate of 1 MHz is 42 m long (5 times 8.3 m that are needed for a 10 GeV beam, Table 5.3) and requires approximately 1.7 MW of electrical power. For comparison, the 50 GeV Stanford Linear Collider (SLC) at SLAC is 3.2 km long and requires over 67 MW of electrical power [17]. Another example is a 3 TeV DLA operated with a peak electric field of 10 GV/m, a laser pulse duration of 100 fs, a driving wavelength of 800 nm and a repetition rate of 1 MHz, with a length of 2.5 km (3 times 830 m, Table 5.3) and a power consumption of 100 MW of electrical power. For comparison, the proposed 3 TeV Compact Linear Collider (CLIC), with a train repetition rate of 50 Hz and 312 bunches per train, is planned to be ∼50 km long with an estimated power consumption of 400 MW [155]. Note that our power consumption estimate does not include recycling of the laser power, i.e., the laser power

$\lambda\,(\mu\mathrm{m})$	$f_{\mathrm{rep}}\,(\mathrm{Hz})$	$E_{\mathrm{p}} = 1\,\mathrm{GV/m}$		$E_{\mathrm{p}} = 10\,\mathrm{GV/m}$	
		$10\,\mathrm{fs}$	$100\,\mathrm{fs}$	$10\,\mathrm{fs}$	$100\,\mathrm{fs}$
0.8	$1\,\mathrm{kHz}$	$4 \cdot 10^{-2}$	$4 \cdot 10^{-1}$	4	$4 \cdot 10^{1}$
	$1\,\mathrm{MHz}$	$4 \cdot 10^{1}$	$4 \cdot 10^{2}$	$4 \cdot 10^{3}$	$4 \cdot 10^{4}$
	$1\,\mathrm{GHz}$	$4 \cdot 10^{4}$	$4 \cdot 10^{5}$	$4 \cdot 10^{6}$	$4 \cdot 10^{7}$
2	$1\,\mathrm{kHz}$	10^{-1}	1	10^{1}	10^{2}
	$1\,\mathrm{MHz}$	10^{2}	10^{3}	10^{4}	10^{5}
	$1\,\mathrm{GHz}$	10^{5}	10^{6}	10^{7}	10^{8}
5	$1\,\mathrm{kHz}$	$2 \cdot 10^{-1}$	2	$2 \cdot 10^{1}$	$2 \cdot 10^{2}$
	$1\,\mathrm{MHz}$	$2 \cdot 10^{2}$	$2 \cdot 10^{3}$	$2 \cdot 10^{4}$	$2 \cdot 10^{5}$
	$1\,\mathrm{GHz}$	$2 \cdot 10^{5}$	$2 \cdot 10^{6}$	$2 \cdot 10^{7}$	$2 \cdot 10^{8}$

Table 5.4: Estimated electrical power consumption per unit length $P_{\mathrm{el}}/\sigma_x = 3.3 \cdot P_{\mathrm{L}}/\sigma_x$ of a DLA (unit: W/m) as a function of driving wavelength λ, repetition rate f_{rep}, laser peak electric field E_{p} and for the laser pulse duration $\tau_{\mathrm{p}} = 10\,\mathrm{fs}$ and $\tau_{\mathrm{p}} = 100\,\mathrm{fs}$. For simplicity we assume the laser to have a constant intensity along the beam direction ($\sigma_x \to \infty$) and a tight transverse laser focus of $\sigma_y = \lambda$, corresponding to a focusing optics with a numerical aperture of NA ~ 0.5.

transmitted through the double grating structure is assumed to be lost. Therefore we expect a lower power consumption in a DLA collider, which most likely will contain power recycling.

5.2.5 Luminosity

An important figure of merit for a collider facility is the luminosity, i.e., the number of particles per unit area and unit time at the target, which is defined as [156]

$$\mathcal{L} = \frac{N^2 f_{\mathrm{rep}} n_{\mathrm{b}}}{4\pi\sigma_x\sigma_y}. \tag{5.9}$$

Here N is the number of particles per bunch, f_{rep} the (train) repetition rate, n_{b} the number of bunches per train and $\sigma_x\sigma_y$ the spot area at the target. CLIC is expected to provide a maximum luminosity of $\mathcal{L} = 6 \cdot 10^{38}\,\mathrm{m^{-2}s^{-1}}$ [155]. Note that by increasing the repetition rate the number of particles per bunch remains constant, which is why $\mathcal{L}$ scales linearly with f_{rep}.

For the DLA collider with $N = 10^6$, $f_{\mathrm{rep}} = 1\,\mathrm{MHz}$, $n_{\mathrm{b}} = 10$ and $\sigma_x = \sigma_y = 1\,\text{Å}$ we obtain $\mathcal{L} = 8 \cdot 10^{37}\,\mathrm{m^{-2}s^{-1}}$. We note that in the CLIC design the input beam with a transverse (normalized) emittance of 20 nm is focused down to 0.9 nm at the target. We expect the DLA to have one order of magnitude smaller beam dimensions. In order to achieve a larger luminosity in a DLA collider it should be investigated how to increase the

wakefield-limited bunch charge, e.g., by increasing the driving wavelength or by working with elliptical beams.

5.3 Generation of X-rays using electron beams

One of the key tools to explore the properties of matter is X-ray radiation. Since its discovery more than a century ago, there has been a lot of progress in producing high energy, high brightness and short pulsed X-rays. Applications of such sources, for example, in X-ray crystallography, range from solid state physics and materials science all the way to chemistry, biology and medicine [3]. Further advances in the production of high energy, coherent X-rays may even pave the way towards nuclear spectroscopy [157] and nuclear quantum optics [158].

One disadvantage of today's advanced X-ray sources is their limited availability to a wide community of potential users, due to the size and cost of accelerator facilities. The envisioned compact and affordable laser-based linacs, both DLAs and plasma-based accelerators, may revolutionize X-ray sources by providing table-top solutions for devices which currently have km-dimensions.

In this section we briefly introduce two classes of advanced X-ray sources based on electron beams: incoherent synchrotron radiation and coherent radiation from free electron lasers. We include recent theoretical and experimental efforts towards merging advanced accelerator technology with these radiation sources [5].

5.3.1 Synchrotron radiation, undulators and wigglers

In Chapter 1 we have introduced the total radiated power emitted by an electron on a circular orbit with radius ρ given by Larmor's formula (Equation 1.2). This synchrotron radiation limits the maximum attainable energy in a circular accelerator, but can also serve as a source of high brightness, high energy X-ray radiation. The synchrotron radiation spectrum consists of harmonics of the revolution frequency $\omega_0 = 2\pi f_{\mathrm{rev}} = 2\pi c/(2\pi\rho) = c/\rho$ and has a cut-off at the critical frequency [159]

$$\omega_{\mathrm{c}} = \frac{c}{\rho}\gamma^3. \tag{5.10}$$

For example, the circular electron accelerator DORIS II at DESY in Hamburg with a bending radius of $\rho = 12\,\mathrm{m}$ and an electron energy of $5\,\mathrm{GeV}$ ($\gamma \sim 10^4$) can provide X-rays up to an energy of $\hbar\omega_{\mathrm{c}} = 23\,\mathrm{keV}$ [160].

Instead of circular accelerators X-ray sources often employ either undulators or wigglers, i.e., periodic arrays of dipole magnets, which force the electrons on an oscillatory trajectory. This way the radiation power emitted during each period adds up leading to an increase in intensity as compared with a circular device. Furthermore, the emitted radiation is more collimated than in circular accelerators. The radiation features are determined by the dimensionless undulator parameter $K = 0.934 \cdot B(\mathrm{T}) \cdot \lambda_{\mathrm{u}}(\mathrm{cm})$, with the

peak magnetic field B and the undulator period λ_u [161]. The spectrum of the undulator radiation shows characteristic peaks at the wavelengths

$$\lambda_\mathrm{n} = \frac{\lambda_\mathrm{u}}{2n\gamma^2}\left(1 + \frac{K^2}{2} + \gamma^2\theta^2\right), \tag{5.11}$$

where θ is the angle of observation relatively to the undulator axis and n is the harmonic number. For $K \ll 1$, radiation occurs only at the fundamental wavelength λ_1. With increasing K the fundamental wavelength becomes longer and higher harmonics appear in the spectrum. Typical undulators operate around $K \sim 1$. For $K \gg 1$, the spectrum becomes very broad and consists of many closely spaced harmonics with an envelope approaching the spectrum of continuous synchrotron radiation [162]. In this limit the device is called wiggler instead of undulator.

On the way towards compact sources of synchrotron and undulator radiation, merging plasma-based accelerators with undulators has been studied. For a detailed review on the theory and experiments of such X-ray sources we refer the reader to [163]. For example, the plasma wave itself can be used as a wiggler, which produces so-called betatron radiation. In a first plasma wiggler experiment at SLAC photon energies up to 30 keV have been measured [164]. A recent milestone has been reached with the combination of laser-plasma accelerated electrons with a 30 cm-long undulator producing radiation with a fundamental wavelength of 18 nm [165].

Besides conventional, i.e., static undulators and plasma wigglers electrons can also oscillate inside intense laser fields. The related radiative process is referred to as inverse Compton or Thompson scattering and combination with LPAs has been studied [5, 163]. A more detailed description of those experiments is beyond the scope of this thesis.

5.3.2 Free electron lasers

If N electrons, which are randomly distributed along the beam, traverse the undulator, the radiation contributed from each electron adds up linearly ($\propto N$). This leads to the synchrotron or undulator radiation discussed in the previous section. However, if the electron beam is bunched with a bunch length smaller than the undulator period, the contributions from the electrons add up coherently ($\propto N^2$) leading to orders of magnitude larger intensities. Under certain circumstances a collective interaction between the undulator radiation field and the electron beam can induce this microbunching, which is known as the free electron laser (FEL) process [166]. FELs represent high intensity, spatially coherent light sources with wavelengths ranging from the microwaves to the X-ray regime. They have optical properties similar to conventional lasers leading to countless applications across many disciplines.

Of critical importance for successful FEL operation is the electron beam quality. It can be shown that the transverse normalized emittance $\tilde{\epsilon}_\mathrm{n}$ has to be smaller than $\gamma\lambda_1/(4\pi)$, with the fundamental wavelength λ_1 (Equation 5.11), also known as the spatial coherence limit. Hence, it becomes clear that ultralow emittance is essential for the generation of

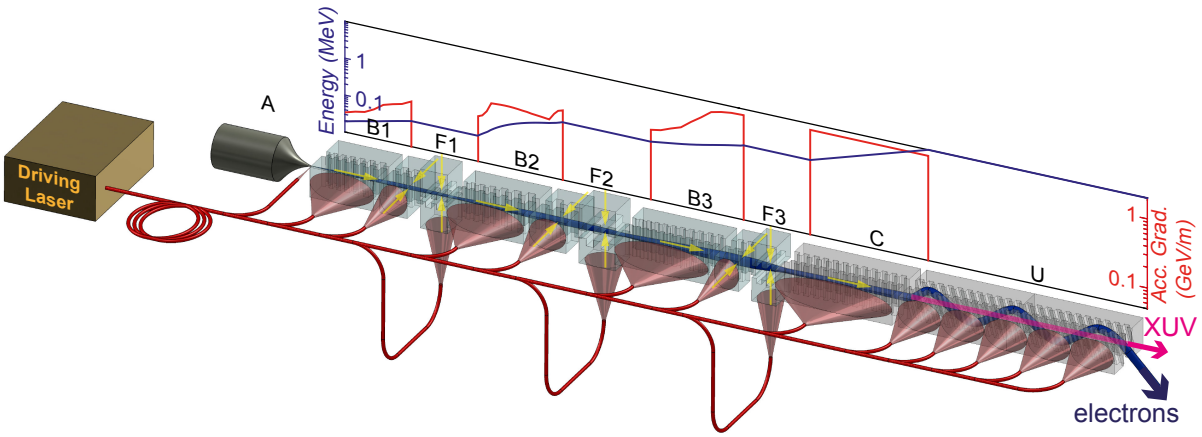

Figure 5.2: Sketch of an envisioned all-optical DLA-based FEL. It consists of the DLA, depicted in Figure 5.1, with an additional dielectric-based undulator section (U) to generate coherent X-ray radiation. Not to scale.

coherent FEL radiation in the X-ray regime. DLAs naturally provide electron beams with a small transverse dimension ($\leq 1\,\mu$m), which in conjunction with well collimated beams leads to a normalized emittance $\sim$1 nm, about 3 orders of magnitude smaller than in conventional FELs [166]. The spatial coherence limit also implies that decreasing the transverse emittance enables FEL operation at lower electron energies and with a shorter undulator period, which scales down the size of the FEL. Therefore, DLAs together with ultralow emittance electron sources [33, 36–40, 167, 168] may be used in compact FELs. On the one hand, DLAs could be used as injectors for compact magnetic undulators [169]. On the other hand, even an all-optical dielectric structure-based FEL seems feasible [78, 79, 170].

In Figure 5.2 we show the envisioned design of such a DLA-based free electron laser. It consists of an accelerator section described above and an undulator that is based on dielectric double grating structures with tilted grating grooves [79]. Coherent X-ray radiation is emitted on-axis in the forward direction. Such a complete system is expected to be only a few meters long and may therefore fit in any laboratory, making available these ultrahigh brilliance sources of X-ray radiation to many scientists around the world.

Chapter 6

Conclusion and outlook

In this proof-of-principle experiment we have successfully demonstrated the inverse Smith-Purcell effect in the optical regime by accelerating non-relativistic 28 keV electrons in the vicinity of a dielectric grating structure. We have measured a maximum energy gain of 280 eV. Together with the short acceleration distance of $\sim$11 μm this corresponds to a maximum acceleration gradient of 25 MeV/m, already comparable to state-of-the-art linacs, such as SLAC. The experimental results show excellent agreement with our simulations.

The intriguing feature of the photonic grating structures used in this work is the direct inter-compatibility with their relativistic counterparts, which allows straightforward concatenation (i.e., scalability) similarly to conventional RF structures. Therefore our findings, together with the demonstration of dielectric laser acceleration of relativistic electrons in parallel to this work by our collaborators in Stanford [13], represent a milestone towards the realization of large-scale dielectric laser accelerators (DLAs) that are expected to be more compact and economical than conventional RF-based facilities.

The main application of DLAs lies in compact sources of coherent high brilliance X-ray radiation, based on the free electron laser (FEL). These lab-scale FELs may lead to a revolution in experiments probing the structure of matter by making available techniques to many laboratories around the world that are currently limited to a few large-scale research facilities.

Further applications based on the grating-based acceleration of non-relativistic electrons may arise in bunching elements for ultrafast electron diffraction experiments or in novel electron optical elements for electron microscopy. The combination of both novel X-ray sources as well as ultrafast electron diffraction experiments may lead to a new kind of pump-probe experiments to explore the structure of materials [171]. Moreover DLA structures may be used for laser-based acceleration of protons and ions with applications, amongst others, in compact sources for particle therapy.

Next steps comprise the combination of the DLA structures with a laser-triggered high-brightness electron source that is synchronized with the driving laser. The design and first experimental results of such a source are reported in [40]. In a different experiment 3 A peak current of a pulsed electron source has been demonstrated [36]. With this peak current, the count rate in our experiment would be increased by almost 12 orders of

magnitude. This would allow to study the acceleration process, the space-charge effect or microbunching in a more detailed manner. Moreover, the realization of double grating structures for non-relativistic electrons represents an important next step, in which surface charging of the dielectric material may pose a challenge. Following these initial steps the simulation and experimental demonstration of mm-long structures that accelerate non-relativistic electrons up to relativistic energies has to be undertaken. Here, the difficulty lies in the compensation of dephasing and beam expansion.

Appendix A

Grating fabrication process

The gratings used in our experiment have been fabricated in a two-step process by the Fraunhofer Institute for Applied Optics and Precision Engineering, Jena, Germany. The fabrication process is described below and depicted in Figure A.1 with kind permission of T. Harzendorf.

These gratings on top of a mesa are fabricated in two consecutive lithographic processes. In the first step of the fabrication of the grating nanostructure electron beam lithography and reactive ion etching (RIE) are used. A fused silica substrate covered with a chromium layer is coated with an electron sensitive resist and is then exposed in an electron beam writer (VISTEC SB350 OS) with the given grating pattern. This pattern, which is present in the resist after a wet chemical development, is transferred into the chromium layer by RIE. The structured chromium layer is used as a hard mask for the deep etching process inductively coupled plasma RIE (ICP-RIE), in which the pattern is transferred into the fused silica substrate.

After the remaining chromium mask has been removed in a wet chemical process, the second lithographic process is applied to the substrate to generate the mesa microstructure. The substrate including the grating is coated with a UV sensitive photoresist. The area outside the grating is exposed by laser lithography. After development, the grating area is protected by the resist. After the following ICP-RIE process, the sample is cleaned leaving behind a monolithic fused silica substrate with a grating located on top of a mesa structure.

In total 28 of these structures were fabricated on a 1 mm thick fused silica wafer. In a final step these gratings were separated by wafer dicing into 3 mm x 20 mm large chips.

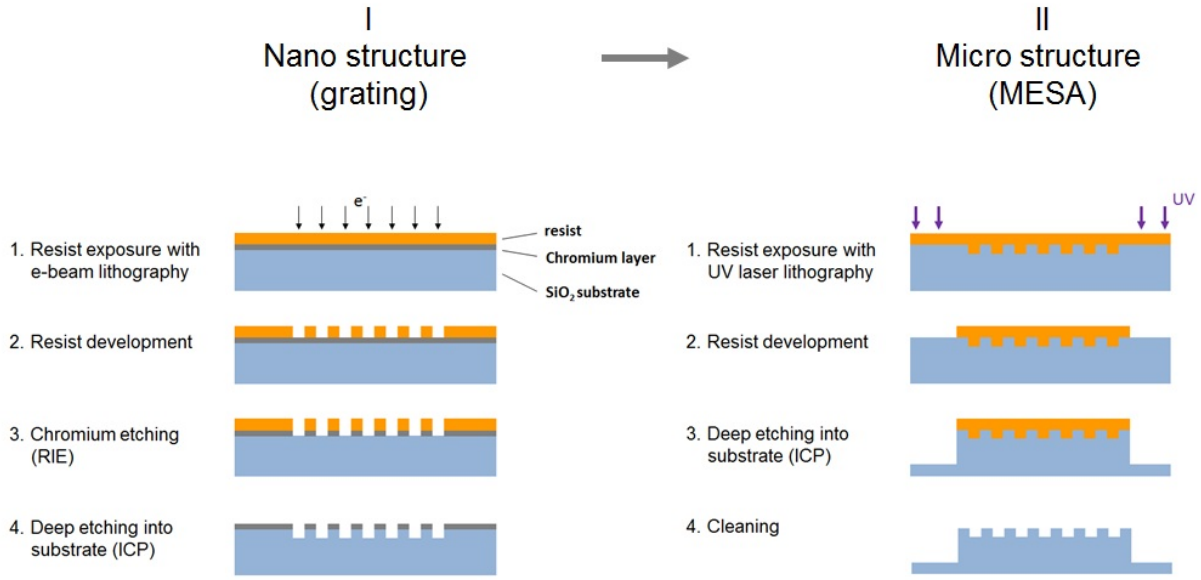

Figure A.1: Illustration of the two-step grating fabrication process. In the first step the grating is etched into the substrate. In the second step the grating is masked and the mesa structure is etched. Details are given in the text. Courtesy of T. Harzendorf, Fraunhofer Institute for Applied Optics and Precision Engineering, Jena, Germany.

Appendix B

Phosphor coating next to the grating mesa structure

In this section we describe the phosphor coating procedure, which we applied to coat the grating substrate that we use as a monitor for the coarse alignment of the electron beam and the laser. In the beginning it was not clear that we could exchange the phosphor-coated grating after initial coarse alignment with an uncoated grating. Therefore the sample was prepared with utmost care to keep the grating surface clean. In addition, the thickness of the phosphor layer is required to be small compared to the mesa height of $\sim$20 μm. We chose the P43 phosphor UKL65/UF-C1 from Phosphor Technology Ltd, which has a median particle size of 2.5 μm. In order to obtain a uniform layer we decided to use the silicate-settling method [172]. This method requires an aqueous environment and it proved rather challenging to create a shield around the mesa to keep the grating free from contaminations.

The mask, which covers the grating during the slide settling method, is produced from a circuit board. A pocket with a width and depth of about 125 μm is milled into the middle of a 0.4 mm wide bar. The grating is then positioned under a microscope in such a way that the mesa resides inside that pocket. Two metal plates are used to clamp the grating substrate onto the mask, as shown in Figure B.1.

The following procedure was used to coat the sample:

- Chemicals needed: potassium silicate solution (sg 1.057), dihydrate barium chloride solution (0.4 g/l $BaCl_2.2H_2O$) and 4% hydrochloric acid.

- Equipment needed: glass dish (inner diameter 7.6 cm), plastic bottle, funnel with small opening around $\sim$1 mm and glass pipette (25 ml).

1. Clean the glass dish with soap and rinse with water. Fill it with hydrochloric acid and let it sit for at least 5 minutes. Then rinse it with destilled water. Also rinse all other equipment with destilled water before use.

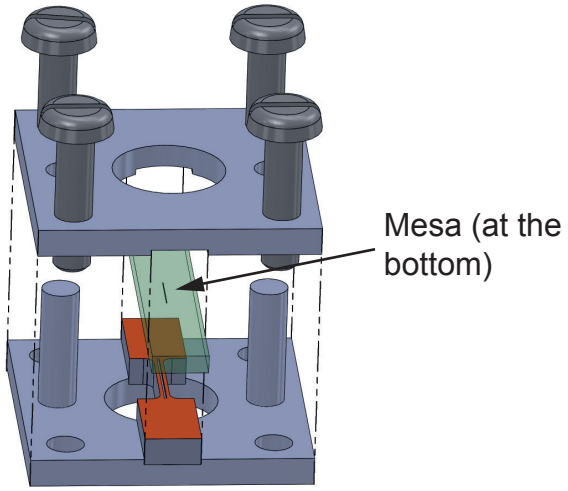

Figure B.1: Drawing of the sample. The mask, which is produced from a circuit board, has a 125 μm wide pocket which is aligned with the mesa. The square metal plates are used to clamp the grating onto the mask.

2. After cleaning the glass dish, fill it about 3 cm with the barium chloride solution. Place the sample into the solution. Put a rod under one side of the dish in order to tilt it by $\sim 5°$.

3. Mix 30 mg phosphor with 22 ml potassium silicate solution in the plastic bottle. With a density of the phosphor of 7.5 g/cm^3 the thickness of the phosphor layer will be $30\,\mathrm{mg}/(7.5\,\mathrm{g/cm^3} \cdot 45\,\mathrm{cm^2}) = 0.9\,\mu$m, which corresponds to 0.4 layers assuming a grain size of 2.5 μm.

4. Fill the mixture into the distributing funnel and keep the opening of the funnel just under the surface of the barium chloride solution. Distribute the mixture evenly and let it settle for 60-90 minutes.

5. Suck out the solution and let it sit for another 15 minutes. Take the sample out and put it upright on filter paper to dry.

The coated sample is shown in Figure 4.6. We note that the crucial parameter for the success of the settling method is the ratio of dissolved barium ions to silicate molecules, i.e., the molar ratio $n_{\mathrm{Ba^{2+}}}/n_{\mathrm{SiO_2}}$ [172]. Hence, care has to be taken when other dishes or different concentrations of the solutions are used. For our recipe the 136 ml barium chloride solution imply $n_{\mathrm{Ba^{2+}}} = 0.4\,\mathrm{g/l} \cdot 0.136\,\mathrm{l}/(244\,\mathrm{g/mol}) = 2.2 \cdot 10^{-4}\,\mathrm{mol}$. The potassium silicate solution (sg 1.32) contains 0.35 wt.% of K_2SiO_3 and therefore has a concentration of $0.35 \cdot 1.32\,\mathrm{g/cm^3} = 462\,\mathrm{g/l}$. This corresponds to a concentration of 3 mol/l, assuming a molar mass of 154 g/mol. To obtain 100 ml sg 1.057 potassium silicate solution we dilute 18 ml sg 1.32 solution with 82 ml distilled water, as $(18 \cdot 1.32 + 82)/100 = 1.057$. Hence, the

concentration of sg 1.057 solution equals $3\,\mathrm{mol/l} \cdot 18/100 = 0.54\,\mathrm{mol/l}$. Therefore 22 ml of the sg 1.057 potassium silicate solution contain $n_{SiO_2} = 119 \cdot 10^{-4}\,\mathrm{mol}$. Thus, the molar ratio $n_{Ba^{2+}}/n_{SiO_2}$ for our recipe is $1.9 \cdot 10^{-2}$.

The most challenging part of the coating procedure was to find a way to mask the mesa in a reliable way. For initial tests we coated a couple of microscope slides instead of the actual grating substrate. Once we solved this problem and found the right concentration of the solutions, the recipe worked with a success rate of over 50%.

List of Variables

$\mathcal{A}$	Electromagnetic field vector: $\mathcal{A}(\mathbf{r}, t) = (\mathbf{E}(\mathbf{r}, t), \mathbf{B}(\mathbf{r}, t))$
$\mathbf{B}$	Magnetic field vector
$\hat{B}$	(Unnormalized) brightness of a particle beam
$\hat{B}_\mathrm{n}$	Normalized brightness of a particle beam
$B_y^{(n)}$	Magnetic field amplitude of the n-th spatial harmonic (TM mode); space and time dependence are omitted: $B_y^{(n)} = B_y^{(n)}(\mathbf{r}, t)$
C_c	Amplitude of the cosh-component of the magnetic field of the accelerating mode inside a double grating structure, leading to a sinh-shaped accelerating field
C_s	Amplitude of the sinh-component of the magnetic field of the accelerating mode inside a double grating structure, leading to a cosh-shaped accelerating field
c	Speed of light: $c = 2.998 \cdot 10^8\,\mathrm{m/s}$
d	Width of the vacuum channel of a double grating structure
d_gr	Grating depth
$\mathbf{E}$	Electric field vector
E_kin	Kinetic energy of a particle
E_p	Laser peak electric field
e	Elementary charge: $e = 1.602 \cdot 10^{-19}\,\mathrm{As}$
$\mathbf{F}$	Force vector
F_p	Laser peak fluence
f	Frequency

f_{rep}	Repetition rate
G	Acceleration gradient
h	Planck constant: $h = 6.626 \cdot 10^{-34}\,\mathrm{kg \cdot m^2/s}$
I_{acc}	Number or current of accelerated electrons
I_{b}	Particle beam current
I_{eff}	Number or current of electrons that can interact with the laser pulse: $I_{\mathrm{eff}} \approx I_{\mathrm{b}} \tau_{\mathrm{p}} f_{\mathrm{rep}}$
j	Electron beam current density
K	Undulator parameter
k_0	Wave vector: $k_0 = 2\pi/\lambda$
k_{p}	Grating vector: $k_{\mathrm{p}} = 2\pi/\lambda_{\mathrm{p}}$
m_0	Rest mass of a particle
m_{e}	Electron mass: $m_{\mathrm{e}} = 9.109 \cdot 10^{-31}\,\mathrm{kg}$
n_0	Plasma density
n_{b}	Number of microbunches per bunch train
Q_{b}	(Macro-)bunch charge
q	Charge of a particle
r_{m}	Beam envelope radius
U_{G}	Counter voltage applied to the spectrometer
U_{G}^0	Counter voltage applied to the spectrometer at the center of the electron spectrum
$\mathbf{v}$	Velocity of a particle
v_{ph}	Phase velocity of the accelerating mode
w_{e}	$1/e$ electron beam waist radius
w_{int}	Characteristic interaction distance of an electron passing by the grating with a laser pulse that is incident perpedicularly to the electron trajectory
w_{l}	$1/e$ waist radius of the laser field

w_{tr}	Trench width of a grating
x_{deph}	Dephasing length
α	Accelerated fraction: $\alpha = I_{\mathrm{acc}}/I_{\mathrm{eff}}$
β	Velocity of the particle in units of the speed of light: $\beta = v/c$
Δ	Longitudinal offset between the grating grooves of the upper and the lower grating of a double grating structure
$\Delta\phi$	Dephasing angle
δ	Decay constant of the evanescent field
ϵ_0	Vacuum permittivity: $\epsilon_0 = 8.854 \cdot 10^{-12}\,\mathrm{As/(Vm)}$
ϵ_{acc}	Acceleration efficiency: $\epsilon_{\mathrm{acc}} = G/E_{\mathrm{p}}$
$\epsilon_{\mathrm{acc}}^{\mathrm{dg}}$	Acceleration efficiency of the double grating: $\epsilon_{\mathrm{acc}}^{\mathrm{dg}} = G(z_0 = 0)/E_{\mathrm{p}}$
ϵ_{exc}	Acceleration efficiency: $\epsilon_{\mathrm{exc}} = cB_y/E_{\mathrm{p}}$
$\tilde{\epsilon}$	(Unnormalized) emittance of a particle beam
$\tilde{\epsilon}_{\mathrm{n}}$	Normalized emittance of a particle beam: $\tilde{\epsilon}_{\mathrm{n}} = \beta\gamma\tilde{\epsilon}$
Φ	Laser polarization angle
γ	Lorentz factor: $\gamma = (1 - \beta^2)^{-1/2}$
λ	Wavelength
λ_{p}	Grating period
λ_{pl}	Plasma wavelength
λ_{u}	Undulator period
ω	Angular frequency: $\omega = 2\pi f$
ω_{pl}	Plasma frequency
ρ	Radius of a particle orbit
τ_{b}	(Macro-)bunch or train duration
τ_{cycle}	Optical cycle: $\tau_{\mathrm{cycle}} = \lambda/c$
τ_{mb}	Microbunch duration
τ_{p}	Laser pulse duration (full width at half maximum (FWHM) of the intensity envelope)

Bibliography

[1] Aad, G. *et al.* Observation of a new particle in the search for the standard model Higgs boson with the ATLAS detector at the LHC. *Phys. Lett. B* **716**, 1–29 (2012).

[2] Chatrchyan, S. *et al.* Observation of a new boson at a mass of 125 GeV with the CMS experiment at the LHC. *Phys. Lett. B* **716**, 30–61 (2012).

[3] Rousse, A., Rischel, C. & Gauthier, J.-C. Femtosecond x-ray crystallography. *Rev. Mod. Phys.* **73**, 17–31 (2001).

[4] DeLaney, T. & Hanne M. Kooy, P. *Proton and charged particle radiotherapy* (Wolters Kluwer Health/Lippincott Williams & Wilkins, 2008).

[5] Carlsten, B. *et al.* New source technologies and their impact on future light sources. *Nucl. Instrum. Methods A* **622**, 657–668 (2010).

[6] Shimoda, K. Proposal for an electron accelerator using an optical maser. *Appl. Opt.* **1**, 33–35 (1962).

[7] Takeda, Y. & Matsui, I. Laser linac with grating. *Nucl. Instrum. Methods* **62**, 306–310 (1968).

[8] Palmer, R. B. Interaction of relativistic particles and free electromagnetic waves in the presence of a static helical magnet. *J. Appl. Phys.* **43**, 3014–3023 (1972).

[9] Tajima, T. & Dawson, J. M. Laser electron accelerator. *Phys. Rev. Lett.* **43**, 267–270 (1979).

[10] Fontana, J. R. & Pantell, R. H. A high-energy, laser accelerator for electrons using the inverse Cherenkov effect. *J. Appl. Phys.* **54**, 4285–4288 (1983).

[11] Rosenzweig, J., Murokh, A. & Pellegrini, C. A proposed dielectric-loaded resonant laser accelerator. *Phys. Rev. Lett.* **74**, 2467 (1995).

[12] Huang, Y. C., Zheng, D., Tulloch, W. M. & Byer, R. L. Proposed structure for a crossed-laser beam, GeV per meter gradient, vacuum electron linear accelerator. *Appl. Phys. Lett.* **68**, 753–755 (1996).

[13] Peralta, E. A. *et al.* Demonstration of electron acceleration in a laser-driven dielectric microstructure. *Nature* **advance online publication**, 27 Sept 2013 (DOI 10.1038/nature12664).

[14] Lilley, J. S. The Daresbury nuclear structure facility. *Physica Scripta* **25**, 435–442 (1982).

[15] Van De Graaff, R. Tandem electrostatic accelerators. *Nucl. Instrum. Methods* **8**, 195–202 (1960).

[16] Jackson, J. *Classical Electrodynamics* (Wiley, 1999).

[17] Seeman, J. The Stanford Linear Collider (1991). SLAC-PUB-5607.

[18] Aßmann, R., Lamont, M. & Myers, S. A brief history of the LEP collider. *Nucl. Phys. B (Proc. Suppl.)* **109**, 17–31 (2002).

[19] Lawson, J. D. Lasers and accelerators. *IEEE Trans. Nucl. Sci.* **26**, 4217–4219 (1979).

[20] Woodward, P. A method of calculating the field over a plane aperture required to produce a given polar diagram. *J. Inst. Electr. Eng.* **93**, 1554–1558 (1946).

[21] Palmer, R. An introduction to acceleration mechanisms. *Frontiers of Particle Beams* **296**, 607–635 (1988).

[22] Esarey, E., Sprangle, P. & Krall, J. Laser acceleration of electrons in vacuum. *Phys. Rev. E* **52**, 5443–5453 (1995).

[23] Boot, H. A. H. & R.-S.-Harvie, R. B. Charged particles in a non-uniform radio-frequency field. *Nature* **180**, 1187–1187 (1957).

[24] Rau, B., Tajima, T. & Hojo, H. Coherent electron acceleration by subcycle laser pulses. *Phys. Rev. Lett.* **78**, 3310–3313 (1997).

[25] Kim, K.-J., McDonald, K. T., Stupakov, G. V. & Zolotorev, M. S. Comment on "Coherent acceleration by subcycle laser pulses". *Phys. Rev. Lett.* **84**, 3210–3210 (2000).

[26] Rau, B., Tajima, T. & Hojo, H. Rau, Tajima, and Hojo reply. *Phys. Rev. Lett.* **84**, 3211–3211 (2000).

[27] Troha, A. L. *et al.* Vacuum electron acceleration by coherent dipole radiation. *Phys. Rev. E* **60**, 926–934 (1999).

[28] Wang, J. X., Scheid, W., Hoelss, M. & Ho, Y. K. Comment on "Vacuum electron acceleration by coherent dipole radiation". *Phys. Rev. E* **65**, 028501 (2002).

[29] Troha, A. L. & Hartemann, F. V. Reply to "Comment on 'Vacuum electron acceleration by coherent dipole radiation' ". *Phys. Rev. E* **65**, 028502 (2002).

[30] Reiser, M. *Theory and Design of Charged Particle Beams* (Wiley-VCH Verlag GmbH, 2007).

[31] Cornacchia, M. & Emma, P. Transverse to longitudinal emittance exchange. *Phys. Rev. ST Accel. Beams* **5**, 084001 (2002).

[32] Emma, P., Huang, Z., Kim, K.-J. & Piot, P. Transverse-to-longitudinal emittance exchange to improve performance of high-gain free-electron lasers. *Phys. Rev. ST Accel. Beams* **9**, 100702 (2006).

[33] Graves, W. S., Kärtner, F. X., Moncton, D. E. & Piot, P. Intense superradiant X rays from a compact source using a nanocathode array and emittance exchange. *Phys. Rev. Lett.* **108**, 263904 (2012).

[34] Dowell, D. H. & Schmerge, J. F. Quantum efficiency and thermal emittance of metal photocathodes. *Phys. Rev. ST Accel. Beams* **12**, 074201 (2009).

[35] Hommelhoff, P., Sortais, Y., Aghajani-Talesh, A. & Kasevich, M. A. Field emission tip as a nanometer source of free electron femtosecond pulses. *Phys. Rev. Lett.* **96**, 077401 (2006).

[36] Ganter, R. *et al.* Laser-photofield emission from needle cathodes for low-emittance electron beams. *Phys. Rev. Lett.* **100**, 064801 (2008).

[37] Tsujino, S. *et al.* Ultrafast electron emission from metallic nanotip arrays induced by near infrared femtosecond laser pulses. *Appl. Phys. Lett.* **92**, 193501 (2008).

[38] Tsujino, S. *et al.* Static and optical field enhancement in metallic nanotips studied by two-photon photoemission microscopy and spectroscopy excited by picosecond laser pulses. *Appl. Phys. Lett.* **94**, 093508 (2009).

[39] Mustonen, A., Beaud, P., Kirk, E., Feurer, T. & Tsujino, S. Five picocoulomb electron bunch generation by ultrafast laser-induced field emission from metallic nano-tip arrays. *Appl. Phys. Lett.* **99**, 103504 (2011).

[40] Hoffrogge, J. *et al.* A tip-based source of femtosecond electron pulses at 30keV (2013). arXiv:1303.2383.

[41] Callaham, M. Quantum-mechanical constraints on electron-beam brightness. *IEEE J. Quantum Electron.* **24**, 1958–1962 (1988).

[42] Wangler, T. P. *RF Linear accelerators* (Wiley-VCH, 2008).

[43] Ising, G. Prinzip einer Methode zur Herstellung von Kanalstrahlen hoher Voltzahl. *Ark. Mat. Astr. Fys.* **18**, 1–4 (1924).

[44] Wideröe, R. Über ein neues Prinzip zur Herstellung hoher Spannungen. *Archiv Elektrotechnik* **21**, 387–406 (1928).

[45] Alvarez, L. W. The design of a proton linear accelerator. *Phys. Rev.* **70**, 799 (1946).

[46] Alvarez, L. W. *et al.* Berkeley proton linear accelerator. *Rev. Sci. Instrum.* **26**, 111–133 (1955).

[47] Cork, B. Proton linear-accelerator injector for the Bevatron. *Rev. Sci. Instrum.* **26**, 210–219 (1955).

[48] Chodorow, M. *et al.* Stanford high-energy linear electron accelerator (Mark III). *Rev. Sci. Instrum.* **26**, 134–204 (1955).

[49] Gerigk, F. Cavity types (2011). arXiv:1111.4897.

[50] Bollinger, L. M. Superconducting linear accelerators for heavy ions. *Ann. Rev. Nucl. Part. Sci.* **36**, 475–503 (1986).

[51] Padamsee, H. The science and technology of superconducting cavities for accelerators. *Supercond. Sci. Technol.* **14**, R28 (2001).

[52] Solyak, N. A. Gradient limitations in room temperature and superconducting acceleration structures. *AIP Conf. Proc.* **1086**, 365–372 (2009).

[53] Higo, T. *et al.* Advances in X-band TW accelerator structures operating in the 100 MV/m regime. In *IPAC 2010 Proceedings*, THPEA013, 3702 (Kyoto, Japan, 2010). SLAC-PUB-15150.

[54] Tantawi, S. G., Dolgashev, V., Higashi, Y. & Spataro, B. Research and development for ultra-high gradient accelerator structures. *AIP Conf. Proc.* **1299**, 29–37 (2010).

[55] Spataro, B. *et al.* Technological issues and high gradient test results on X-band molybdenum accelerating structures. *Nucl. Instrum. Methods A* **657**, 114–121 (2011).

[56] Grudiev, A., Calatroni, S. & Wuensch, W. New local field quantity describing the high gradient limit of accelerating structures. *Phys. Rev. ST Accel. Beams* **12**, 102001 (2009).

[57] Aune, B. *et al.* Superconducting TESLA cavities. *Phys. Rev. ST Accel. Beams* **3**, 092001 (2000).

[58] Yakovlev, V., Avrakhov, P., Kanareykin, A., Kazakov, S. & Solyak, N. Progress towards development of a superconducting traveling wave accelerating structure. In *Particle Accelerator Conference, 2007. PAC. IEEE*, 2182–2184 (2007).

[59] Lebrun, P. *et al.* A multi-TeV linear collider based on CLIC technology. Tech. Rep., CERN (2012). CERN-2012-007.

[60] Phinney, N., Toge, N. & Walker, N. ILC Reference Design Report Volume 3 - Accelerator (2007). arXiv:0712.2361.

[61] Maiman, T. H. Stimulated optical radiation in ruby. *Nature* **187**, 493–494 (1960).

[62] Palmer, R. A laser-driven grating linac. *Part. Accel.* **11**, 81–90 (1980).

[63] Mizuno, K., Ono, S. & Shimoe, O. Interaction between coherent light waves and free electrons with a reflection grating. *Nature* **253**, 184–185 (1975).

[64] Mizuno, K., Pae, J., Nozokido, T. & Furuya, K. Experimental evidence of the inverse Smith-Purcell effect. *Nature* **328**, 45–47 (1987).

[65] Bae, J. *et al.* Experimental verification of the theory on the inverse Smith-Purcell effect at a submillimeter wavelength. *Appl. Phys. Lett.* **61**, 870–872 (1992).

[66] Yoder, R. B. & Rosenzweig, J. B. Side-coupled slab-symmetric structure for high-gradient acceleration using terahertz power. *Phys. Rev. ST Accel. Beams* **8**, 111301 (2005).

[67] Cowan, B. M. Three-dimensional dielectric photonic crystal structures for laser-driven acceleration. *Phys. Rev. ST Accel. Beams* **11**, 011301 (2008).

[68] Plettner, T., Lu, P. P. & Byer, R. L. Proposed few-optical cycle laser-driven particle accelerator structure. *Phys. Rev. ST Accel. Beams* **9**, 111301 (2006).

[69] Du, D., Liu, X., Korn, G., Squier, J. & Mourou, G. Laser-induced breakdown by impact ionization in SiO_2 with pulse widths from 7 ns to 150 fs. *Appl. Phys. Lett.* **64**, 3071–3073 (1994).

[70] Stuart, B. C. *et al.* Optical ablation by high-power short-pulse lasers. *J. Opt. Soc. Am. B* **13**, 459–468 (1996).

[71] Lenzner, M. *et al.* Femtosecond optical breakdown in dielectrics. *Phys. Rev. Lett.* **80**, 4076–4079 (1998).

[72] Lin, X. E. Photonic band gap fiber accelerator. *Phys. Rev. ST Accel. Beams* **4**, 051301 (2001).

[73] Cowan, B. M. Two-dimensional photonic crystal accelerator structures. *Phys. Rev. ST Accel. Beams* **6**, 101301 (2003).

[74] Zakowicz, W. Particle acceleration by wave scattering off dielectric spheres at whispering-gallery-mode resonance. *Phys. Rev. ST Accel. Beams* **10**, 101301 (2007).

[75] Neuner, B., III, Korobkin, D., Ferro, G. & Shvets, G. Prism-coupled surface wave accelerator based on silicon carbide. *Phys. Rev. ST Accel. Beams* **15**, 031302 (2012).

[76] Naranjo, B., Valloni, A., Putterman, S. & Rosenzweig, J. B. Stable charged-particle acceleration and focusing in a laser accelerator using spatial harmonics. *Phys. Rev. Lett.* **109**, 164803 (2012).

[77] Wong, L. J., Fallahi, A. & Kärtner, F. X. Compact electron acceleration and bunch compression in THz waveguides. *Opt. Express* **21**, 9792–9806 (2013).

[78] Plettner, T. & Byer, R. L. Proposed dielectric-based microstructure laser-driven undulator. *Phys. Rev. ST Accel. Beams* **11**, 030704 (2008).

[79] Plettner, T. & Byer, R. L. Microstructure-based laser-driven free-electron laser. *Nucl. Instrum. Methods A* **593**, 63–66 (2008).

[80] Plettner, T., Byer, R. L., McGuinness, C. & Hommelhoff, P. Photonic-based laser driven electron beam deflection and focusing structures. *Phys. Rev. ST Accel. Beams* **12**, 101302 (2009).

[81] Esarey, E., Sprangle, P., Krall, J. & Ting, A. Overview of plasma-based accelerator concepts. *IEEE Trans. Plasma Sci.* **24**, 252–288 (1996).

[82] Esarey, E., Schroeder, C. B. & Leemans, W. P. Physics of laser-driven plasma-based electron accelerators. *Rev. Mod. Phys.* **81**, 1229–1285 (2009).

[83] Kirby, N. *et al.* Energy measurements of trapped electrons from a plasma wakefield accelerator. *AIP Conf. Proc.* **877**, 541–546 (2006).

[84] Dawson, J. M. Nonlinear electron oscillations in a cold plasma. *Phys. Rev.* **113**, 383–387 (1959).

[85] Strickland, D. & Mourou, G. Compression of amplified chirped optical pulses. *Opt. Commun.* **56**, 219–221 (1985).

[86] Fritzler, S. *et al.* Emittance measurements of a laser-wakefield-accelerated electron beam. *Phys. Rev. Lett.* **92**, 165006 (2004).

[87] Mangles, S. P. D. *et al.* Monoenergetic beams of relativistic electrons from intense laser-plasma interactions. *Nature* **431**, 535–538 (2004).

[88] Geddes, C. G. R. *et al.* High-quality electron beams from a laser wakefield accelerator using plasma-channel guiding. *Nature* **431**, 538–541 (2004).

[89] Faure, J. *et al.* A laser-plasma accelerator producing monoenergetic electron beams. *Nature* **431**, 541–544 (2004).

[90] Leemans, W. P. *et al.* GeV electron beams from a centimetre-scale accelerator. *Nat. Phys.* **2**, 696–699 (2006).

[91] Wang, X. *et al.* Quasi-monoenergetic laser-plasma acceleration of electrons to 2 GeV. *Nat. Commun.* **4**, 1988 (2013).

[92] Lundh, O. *et al.* Few femtosecond, few kiloampere electron bunch produced by a laser-plasma accelerator. *Nat. Phys.* **7**, 219–222 (2011).

[93] Osterhoff, J. *et al.* Generation of stable, low-divergence electron beams by laser-wakefield acceleration in a steady-state-flow gas cell. *Phys. Rev. Lett.* **101**, 085002 (2008).

[94] Hafz, N. A. M. *et al.* Stable generation of GeV-class electron beams from self-guided laser-plasma channels. *Nat. Photon.* **2**, 571–577 (2008).

[95] Liu, J. S. *et al.* All-optical cascaded laser wakefield accelerator using ionization-induced injection. *Phys. Rev. Lett.* **107**, 035001 (2011).

[96] Pollock, B. B. *et al.* Demonstration of a narrow energy spread, ∼0.5 GeV electron beam from a two-stage laser wakefield accelerator. *Phys. Rev. Lett.* **107**, 045001 (2011).

[97] Chen, P., Dawson, J. M., Huff, R. W. & Katsouleas, T. Acceleration of electrons by the interaction of a bunched electron beam with a plasma. *Phys. Rev. Lett.* **54**, 693–696 (1985).

[98] Rosenzweig, J. B., Breizman, B., Katsouleas, T. & Su, J. J. Acceleration and focusing of electrons in two-dimensional nonlinear plasma wake fields. *Phys. Rev. A* **44**, R6189–R6192 (1991).

[99] Ruth, R. D., Chao, A. W., Morton, P. L. & Wilson, P. B. A plasma wakefield accelerator. *Part. Accel.* **17**, 171–189 (1985).

[100] Blumenfeld, I. *et al.* Energy doubling of 42 GeV electrons in a metre-scale plasma wakefield accelerator. *Nature* **445**, 741–744 (2007).

[101] Hidding, B. *et al.* Ultracold electron bunch generation via plasma photocathode emission and acceleration in a beam-driven plasma blowout. *Phys. Rev. Lett.* **108**, 035001 (2012).

[102] Scully, M. A simple laser linac. *Appl. Phys. B* **51**, 238–241 (1990).

[103] Scully, M. O. & Zubairy, M. S. Simple laser accelerator: Optics and particle dynamics. *Phys. Rev. A* **44**, 2656–2663 (1991).

[104] Bochove, E. J., Moore, G. T. & Scully, M. O. Acceleration of particles by an asymmetric Hermite-Gaussian laser beam. *Phys. Rev. A* **46**, 6640–6653 (1992).

[105] Haaland, C. M. Laser electron acceleration in vacuum. *Opt. Commun.* **114**, 280–284 (1995).

[106] Liu, Y., Cline, D. & He, P. Vacuum laser acceleration using a radially polarized CO_2 laser beam. *Nucl. Instrum. Methods A* **424**, 296–303 (1999).

[107] Varin, C. *et al.* Direct electron acceleration with radially polarized laser beams. *Appl. Sci.* **3**, 70–93 (2013).

[108] Payeur, S. *et al.* Generation of a beam of fast electrons by tightly focusing a radially polarized ultrashort laser pulse. *Appl. Phys. Lett.* **101**, 041105 (2012).

[109] Kieffer, J. C. Private communication.

[110] Pantell, R. H. & Piestrup, M. A. Free-electron momentum modulation by means of limited interaction length with light. *Appl. Phys. Lett.* **32**, 781–783 (1978).

[111] Plettner, T. *et al.* Visible-laser acceleration of relativistic electrons in a semi-infinite vacuum. *Phys. Rev. Lett.* **95**, 134801 (2005).

[112] Plettner, T. *et al.* Proof-of-principle experiment for laser-driven acceleration of relativistic electrons in a semi-infinite vacuum. *Phys. Rev. ST Accel. Beams* **8**, 121301 (2005).

[113] Piestrup, M. A., Rothbart, G. B., Fleming, R. N. & Pantell, R. H. Momentum modulation of a free electron beam with a laser. *J. Appl. Phys.* **46**, 132–137 (1975).

[114] Edighoffer, J. A., Kimura, W. D., Pantell, R. H., Piestrup, M. A. & Wang, D. Y. Observation of inverse Čerenkov interaction between free electrons and laser light. *Phys. Rev. A* **23**, 1848 (1981).

[115] Kimura, W. D. *et al.* Laser acceleration of relativistic electrons using the inverse Cherenkov effect. *Phys. Rev. Lett.* **74**, 546–549 (1995).

[116] Sprangle, P., Hafizi, B. & Hubbard, R. F. Ionization and pulse lethargy effects in inverse Cherenkov accelerators. *Phys. Rev. E* **55**, 5964–5975 (1997).

[117] Courant, E. D., Pellegrini, C. & Zakowicz, W. High-energy inverse free-electron-laser accelerator. *Phys. Rev. A* **32**, 2813–2823 (1985).

[118] Kimura, W. D. *et al.* Demonstration of high-trapping efficiency and narrow energy spread in a laser-driven accelerator. *Phys. Rev. Lett.* **92**, 054801 (2004).

[119] Musumeci, P. *et al.* High energy gain of trapped electrons in a tapered, diffraction-dominated inverse-free-electron laser. *Phys. Rev. Lett.* **94**, 154801 (2005).

[120] Sears, C. M. S. *et al.* Production and characterization of attosecond electron bunch trains. *Phys. Rev. ST Accel. Beams* **11**, 061301 (2008).

[121] Saito, N. & Ogata, A. Plasmon linac: A laser wake-field accelerator based on a solid-state plasma. *Phys. Plasmas* **10**, 3358–3362 (2003).

[122] Mourou, G., Brocklesby, B., Tajima, T. & Limpert, J. The future is fibre accelerators. *Nat. Photon.* **7**, 258–261 (2013).

[123] Poppe, A. *et al.* Few-cycle optical waveform synthesis. *Appl. Phys. B* **72**, 373–376 (2001).

[124] Shelton, R. K. *et al.* Phase-coherent optical pulse synthesis from separate femtosecond lasers. *Science* **293**, 1286–1289 (2001).

[125] Pukhov, A., Kostyukov, I., Tückmantel, T. & Luu-Thanh, P. Electron acceleration by coherent laser pulse echelons in periodic plasma structures (2013). arXiv:1306.6516.

[126] Breuer, J. & Hommelhoff, P. (2013). In preparation.

[127] Earnshaw, S. On the nature of the molecular forces which regulate the constitution of the luminiferous ether. *Trans. Camb. Phil. Soc.* **7**, 97 (1842).

[128] Good, M. L. Phase-reversal focusing in linear accelerators. *Phys. Rev.* **92**, 538–538 (1953).

[129] Swenson, D. A. Alternating phase focused linacs. *Part. Accel.* **7**, 61–67 (1976).

[130] Plettner, T., Byer, R. L. & Montazeri, B. Electromagnetic forces in the vacuum region of laser-driven layered grating structures. *J. Mod. Opt.* **58**, 1518–1528 (2011).

[131] Yee, K. Numerical solution of inital boundary value problems involving Maxwell's equations in isotropic media. *IEEE Trans. Antennas Propag.* **14**, 302–307 (1966).

[132] Coccioli, R., Itoh, T., Pelosi, G. & Silvester, P. Finite-element methods in microwaves : A selected bibliography. *IEEE Trans. Antennas Propag.* **38**, 34–48 (1996).

[133] Ferrari, R. The finite-element method, part 2: P. P. Silvester, an innovator in electromagnetic numerical modeling. *IEEE Trans. Antennas Propag.* **49**, 216–234 (2007).

[134] Weiland, T. A discretization model for the solution of Maxwell's equations for six-component fields. *Archiv Elektronik und Übertragungstechnik* **31**, 116–120 (1977).

[135] Liu, Q. H. & Zhao, G. Advances in PSTD techniques. In Taflove, A. & Hagness, S. (eds.) *Computational Electromagnetics: The Finite-Difference Time-Domain Method* (Artech House, Inc., 2005).

[136] Pai, D. M. & Awada, K. A. Analysis of dielectric gratings of arbitrary profiles and thicknesses. *J. Opt. Soc. Am. A* **8**, 755–762 (1991).

[137] Tremain, D. E. & Mei, K. K. Application of the unimoment method to scattering from periodic dielectric structures. *J. Opt. Soc. Am.* **68**, 775 (1978).

[138] Soong, K., Byer, R. L., McGuinness, C., Peralta, E. & Colby, E. Experimental determination of damage threshold characteristics of IR compatible optical materials. In *Proceedings of 2011 Particle Accelerator Conference*, 277–279 (IEEE, New York, 2011).

[139] Breuer, J. & Hommelhoff, P. Laser-based acceleration of nonrelativistic electrons at a dielectric structure. *Phys. Rev. Lett.* **111**, 134803 (2013).

[140] Naumov, S. *et al.* Approaching the microjoule frontier with femtosecond laser oscillators. *N. J. Phys.* **7**, 216 (2005).

[141] Shannon, J. P., Philp, S. F. & Trump, J. G. Insulation of high voltage across solid insulators in vacuum. *J. Vac. Sci. Technol.* **2**, 234–239 (1965).

[142] Hawley, R. Solid insulators in vacuum: A review (invited paper). *Vacuum* **18**, 383–390 (1968).

[143] Brack, K. Über eine Anordnung zur Filterung von Elektroneninterferenzen. *Z. Naturforsch. Teil A* **17**, 1066–1070 (1962).

[144] Kofoid, M. J. Effect of metal-dielectric junction phenomena on high-voltage breakdown over insulators in vacuum. *Power Apparatus and Systems, Part III.* **79**, 999–1004 (1960).

[145] Steib, G. F. & Moll, E. High-voltage conditioning at large gaps in industrial vacuum. *J. Phys. D* **6**, 243 (1973).

[146] Diamond, W. T. New perspectives in vacuum high voltage insulation. II. Gas desorption. *J. Vac. Sci. Technol. A* **16**, 720–735 (1998).

[147] Wiedemann, H. *Particle Accelerator Physics* (Springer, 2007).

[148] Paresce, F. Quantum efficiency of a channel electron multiplier in the far ultraviolet. *Appl. Opt.* **14**, 2823–2824 (1975).

[149] Lawson, J. D. Perveance and the bennett pinch relation in partially-neutralized electron beams. *J. Electr. Contr.* **5**, 146–151 (1958).

[150] Travier, C. Review of microwave guns. *Part. Accel.* **36**, 33–74 (1991).

[151] Rosenzweig, J., Barov, N. & Colby, E. Pulse compression in radio frequency photoinjectors-applications to advanced accelerators. *IEEE Trans. Plasma Sci.* **24**, 409–420 (1996).

[152] Anderson, S. G. *et al.* Velocity bunching of high-brightness electron beams. *Phys. Rev. ST Accel. Beams* **8**, 014401 (2005).

[153] Rosenzweig, J. *et al.* Generation of ultra-short, high brightness electron beams for single-spike SASE FEL operation. *Nucl. Instrum. Methods A* **593**, 39–44 (2008).

[154] Paschotta, R. *Encyclopedia of laser physics and technology*, vol. 1 (Wiley-VCH Berlin, 2008).

[155] Braun, H. *et al.* CLIC 2008 parameters (2008). CLIC-Note-764.

[156] Nakamura, K. & Group, P. D. Review of particle physics. *J. Phys. G* **37**, 075021–(2010).

[157] Pietralla, N. *et al.* Parity measurements of nuclear levels using a free-electron-laser generated γ-ray beam. *Phys. Rev. Lett.* **88**, 012502 (2001).

[158] Di Piazza, A., Müller, C., Hatsagortsyan, K. Z. & Keitel, C. H. Extremely high-intensity laser interactions with fundamental quantum systems. *Rev. Mod. Phys.* **84**, 1177–1228 (2012).

[159] Wiedemann, H. *Synchrotron Radiation* (Springer, 2003).

[160] Wille, K. Synchrotron radiation sources. *Rep. Prog. Phys.* **54**, 1005 (1991).

[161] Winick, H., Brown, G., Halbach, K. & Harris, J. Wiggler and undulator magnets. *Phys. Today* **34**, 50–63 (1981).

[162] Brown, G., Halbach, K., Harris, J. & Winick, H. Wiggler and undulator magnets - A review. *NIM* **208**, 65–77 (1983).

[163] Corde, S. *et al.* Femtosecond X rays from laser-plasma accelerators. *Rev. Mod. Phys.* **85**, 1–48 (2013).

[164] Wang, S. *et al.* X-ray emission from betatron motion in a plasma wiggler. *Phys. Rev. Lett.* **88**, 135004 (2002).

[165] Fuchs, M. *et al.* Laser-driven soft-X-ray undulator source. *Nat. Phys.* **5**, 826–829 (2009).

[166] McNeil, B. W. J. & Thompson, N. R. X-ray free-electron lasers. *Nat. Photon.* **4**, 814–821 (2010).

[167] Li, R. K. *et al.* Surface-plasmon resonance-enhanced multiphoton emission of high-brightness electron beams from a nanostructured copper cathode. *Phys. Rev. Lett.* **110**, 074801 (2013).

[168] Polyakov, A. *et al.* Plasmon-enhanced photocathode for high brightness and high repetition rate x-ray sources. *Phys. Rev. Lett.* **110**, 076802 (2013).

[169] Harrison, J., Joshi, A., Lake, J., Candler, R. & Musumeci, P. Surface-micromachined magnetic undulator with period length between 10 μm and 1 mm for advanced light sources. *Phys. Rev. ST Accel. Beams* **15**, 070703 (2012).

[170] Chang, C., Tang, C. & Wu, J. High-gain Thompson-scattering X-ray free-electron laser by time-synchronic laterally tilted optical wave. *Phys. Rev. Lett.* **110**, 064802 (2013).

[171] Carbone, F., Musumeci, P., Luiten, O. & Hebert, C. A perspective on novel sources of ultrashort electron and x-ray pulses. *Chem. Phys.* **392**, 1–9 (2012).

[172] Smith, M. L. Adhesion of silicate-settled phosphor screens. *J. Appl. Chem.* **5**, 271–288 (1955).

Acknowledgements

I would like to thank the following people whose help and support made this work possible. My biggest thanks goes to Prof. Peter Hommelhoff, who supervised this project. Besides the knowledgable advice on solutions for everyday issues in the lab, Peter's encouraging words helped me to stay persistent when confronted with a seemingly unsolvable problem. His positive attitude kept me going and focusing on the goal that often seemed so far away. Moreover, he was always understanding when family matters interfered with work, which happened quite a bit with two small children at home. In every respect I could not have wished for a better advisor.

I would also like to acknowledge the help of Roswitha Graf and Johannes Hoffrogge in setting up the experiment. Rosi spent weeks of her time helping me to set up the laser system. Without her help and experience the laser would probably be still not operating stable enough to perform any measurements. Jo contributed in particular to the modifications of the electron microscope unit. I also greatly appreciate especially his expertise in electronics that helped me solve a lot of problems.

Thanks to our precision engineers Wolfgang Simon and Karl ("Charly") Linner, who helped with the mechanical layout of the experiment. Through discussions with Wolfgang and Charly I have gained insight into the practical design of mechanical systems. Moreover, they have taught me a lot of know-how and tricks in the workshop, which will be of great importance for my life even beyond this project. I also appreciate the advice of our electronics engineers Helmut Brückner and Anton Scheich. Philipp Altpeter kindly helped with gold and titanium coating of the gratings.

I would like to give a special thanks to Harishchandra Ramadas and Robert Davies, who helped to set up and run extensive simulations. Furthermore, I greatly appreciate the discussions with and the advice from former and current members of the Ultrafast Quantum Optics group. I especially mention Markus Schenk, Michael Krüger, Jakob Hammer, Michael Förster, Sebastian Thomas, Max Eisele and Hanno Kaupp. I am also grateful for the discussion with our collaborators at the Stanford University and SLAC, in particular, Chris Sears, Joel England, Edgar Peralta, Ken Leedle and Prof. Byer. Thanks to Valentin Batteiger and Takuya Higuchi for proofreading of this thesis.

Last but not least I would like to thank my family, especially my wife Julia and my sons Trey and Lukas, for their emotional and financial support. After a stressful and sometimes frustrating day in the lab it was very important for me to clear my head by spending time with my family. Thanks also to my parents without whose support I could

not have made it this far.